Microgrid Enabling Towards the Implementation of Active Distribution Systems: Planning, Operation, and Energy Trading

by

Ahmed Ibrahim Magdy Kamel Morsy Sallam

A thesis
presented to the University of Waterloo
in fulfillment of the
thesis requirement for the degree of
Doctor of Philosophy
in
Electrical and Computer Engineering

Waterloo, Ontario, Canada, 2020

Examining Committee Membership

The following served on the Examining Committee for this thesis. The decision of the Examining Committee is by majority vote.

Supervisor	Magdy Salama Professor
External Examiner	Osama A. Mohammed Professor
Internal Member	Mehrdad Kazerani Professor
Internal Member	Tarek Abdelgalil Adjunct Professor
Internal-external Member	Eihab Abdel-Rahman Professor

AUTHOR'S DECLARATION

I hereby declare that I am the sole author of this thesis. This is a true copy of the thesis, including any required final revisions, as accepted by my examiners.

I understand that my thesis may be made electronically available to the public.

Abstract

Recent years have perceived a substantial surge in interest in green technologies due to the growing awareness about the environmental concerns and the technologies' development, which have resulted in considerable utilization of DC-based distributed generators (DGs) and loads such as photovoltaic (PV) panels and electric vehicles. This increased penetration has reformed the generation and utilization of electric, resulting in promoting the microgrids (μGs) as a promising candidate for future systems. Despite the well-establishment and the extensive studies of μGs, there is still some debate over having μGs that are purely AC, purely DC, or AC-DC hybrid. Purely AC and purely DC configurations cannot meet the challenges and the new technologies that are expected to emerge in the near future as they require many interfacing converters to accommodate the high penetration of DC DGs and loads. These interfacing converters increase the system costs, the conversion losses, and the system complexity. The aforementioned reasons have resulted in the consensus tending towards a new vision of combining the AC and DC to acquire the benefits of both systems, which calls for further investigation of the AC-DC system compositions.

The growing electricity demand, aging of the power system infrastructure, and countries effort to utilize renewable-based DGs have stimulated the concept of isolated μGs. Isolated μGs could allow utilities and developers to defer the installation of new generation capacities, in addition to transmission and distribution capacities upgrades by connecting distributed energy resources. Despite the significant benefits provided by isolated μGs, preserving load-generation balance is comprehensively challenging, given that μGs are dominated by renewable-based DGs, which are characterized by their probabilistic nature and intermittent power. This challenge introduced the interconnection of μGs as a promising solution that enhance the system operation and increase the system reliability. The interconnection of a group of μGs essentially leads to a (small scale) energy market of interconnected microgrids (IμGs) when these μGs exchange energy with each other. Therefore, it is vital to refine and enhance the way in which players from different μGs construct the interconnected μGs and manage electricity trading.

Driven by the aforementioned challenges, the main objective of this thesis is to promote the concept of μG and optimally accommodate the expected increased penetration of DC DGs and DC loads in future systems, and ensure the continuity of power supplied to these future systems through their interconnection and managing the energy trading process. Achieving this target entailed the completion of the following parts: 1) Proposing the

bilayer μGs configuration, in addition to its power flow model, at which each node is a universal node that can include two buses with different types of power (AC and DC) or a single bus (AC or DC). The inclusion of the two types of power reduces the number of interfacing converters and allows for the accommodation of the increased penetration of DC DGs and loads besides the existing conventional AC DGs and loads. 2) Proposing a stochastic planning framework for the network configuration of AC-DC bilayer μGs that is capable of minimizing the total system costs through the determination of the optimal BμG configuration. 3) Investigating the AC-DC bilayer μGs operation under fault conditions and introducing a multilevel converter with fault confining capability that can isolate the faulty layer, and hence ensures optimal and reliable operation of the healthy layer under fault conditions. 4) The proposal of a stochastic planning framework for the IμGs that minimizes the total system costs and minimizes the loads curtailment under DG failure, while considering the stochastic variations of the renewable-based DGs and loads. 5) Developing an energy trading mechanism that facilitates the power trading between the interconnected μGs, provides full utilization of the renewable output power, minimizes operation cost, and minimizes load curtailment.

Acknowledgements

I would like to express my appreciation and gratitude to my supervisor, Professor Magdy Salama for his guidance, continuous support, patience and inspiration. It has been a great honor and privilege to complete my studies under his supervision. His excellent guidance was crucial for the completeness of this thesis.

I would like to thank all my Ph.D committee members: Professor Mehrdad Kazerani, Professor Tarek AbdelGalil, and Professor Eihab Abdelrahman, for their time, suggestions, and constructive criticism. Thanks are also extended to my external examiner, Professor Osama A. Mohammed, for coming to referee this thesis.

I would also like to thank Dr. Haytham Abdelrahman for his valuable comments, discussions, and support during my Ph.D.

I cannot describe my feelings to my parents and brothers. Without their sacrifices, love, and affection I would not have been able to accomplish this research. They are my source of endless motivation, which never fails to pick me up in the most difficult moments.

I would like to thank my wife Nourane for her love and constant support, for all the late nights and early mornings, and for keeping me sane over the past few months. Thank you for being my best friend and my source of happiness. I owe you everything.

Dedication

To my parents,
my wife,
and my brothers...

Table of Contents

List of Figures

List of Tables

Nomenclature

Acronyms

μG	Microgrid
μGCC	Microgrid central controller
AC	Alternating current
ACB	AC breaker
BμG	AC-DC bilayer microgrid
CDF	Cumulative distribution function
CT	Conventional trading
DATM	Dual action trading mechanism
DC	Direct current
DCB	DC breaker
DER	Distributed energy resources
DG	Distributed generator
DS	Distribution system
ES	Energy storage

EV	Electric vehicle
EVS	Electric vehicle station
GA	Genetic algorithm
GAMS	General algebraic modeling system
HμG	AC-DC hybrid microgrid
HVAC	High voltage alternating current
HVDC	High voltage direct current
IμG	Interconnected Microgrid
IC	Interlinking converter
LF	Load flow
LVDC	Low voltage direct current
MCS	Monte-Carlo Simulation
MMC	Modular Multilevel Converter
OPF	Optimal power flow
PCC	Point of common coupling
PDPWM	Phase Disposition Pulse Width Modulation
PV	Photovoltaic
SCSM	Switched capacitor submodule
SM	Submodule
VPV	Virtual power variable
VSC	Voltage source converter

Parameters

FR	Inflation rate
$\eta_{c\text{-}n\text{-}i}$	Efficiency of an inverter at bus n (as a %)
$\eta_{c\text{-}n\text{-}r}$	Efficiency of a rectifier at bus n (as a %)
$\eta_{inv/rec}$	Efficiency of an interfacing inverter/rectifier, as a %
λ_{AM}	Annual maintenance cost as a % of the investment cost
$\rho_{D_{jk}}$	Price of block k bid by demand j
$\rho_{G_{ib}}$	Price of block b offered by generator i
B^{ac}_{nm}	Susceptance of the AC line connecting buses n and m, p.u.
$C^{ac/dc}_{l}$	Cost of AC/DC lines, in $/mile.
$C^{cb,ac}_{c\text{-}xy}$	Cost of the breaker at the AC side of the IC connecting two candidate buses x and y
$C^{cb,dc}_{c\text{-}xy}$	Cost of the breaker at the DC side of the IC connecting two candidate buses x and y
$C^{ac/dc}_{cb,c\text{-}nx}$	Cost of the breaker at the AC/DC side of the interlinking converter connecting AC bus n and DC bus x
$C^{ac/dc}_{cb,u}$	Cost of AC/DC breaker for component u, which can be AC line (nm), DC line (xy), AC DG (G_i), DC DG (G_j), AC load (L_n), or DC load (L_x)
C_{conv}	Cost of the interlinking converter, in $/kVA
C_{exp}	Cost of exporting power (in $/MWh)
$C^{ac}_{G_i}$	Generation costs of the AC energy resources, in $/MWh
$C^{dc}_{G_j}$	Generation costs of the DC energy resources, in $/MWh

C_{imp}	Cost of imported power
C_{imp}	Cost of importing power (in \$/MWh)
$C_{xy}^{cb,ac}$	Cost of an AC breaker installed in the line connecting candidate buses x and y
$C_{xy}^{cb,dc}$	Cost of an DC breaker installed in the line connecting candidate buses x and y
G_{nm}^{ac}	AC line connecting buses n and m conductance, p.u.
G_{xy}^{dc}	DC line connecting buses x and y Conductance, p.u.
IR	Interest rate
$IR^{'}$	Modified interest rate
L_{xy}^{ac}	Distance (in miles) of an AC line connecting two candidate buses x and y
L_{xy}^{dc}	Distance (in miles) of an DC line connecting two candidate buses x and y
L_{nm}	Distance of AC line nm, in miles
L_{xy}	Distance of DC line xy, in miles
N_{c}^{max}	Maximum allowable number of interlinking converters
$N_{L,n}^{max/min}$	maximum/minimum permissible number of lines that can be connected to an AC bus n
$N_{L,x}^{max/min}$	maximum/minimum permissible number of lines that can be connected to an DC bus x
$N_{L,x}^{max}$	Maximum allowable interconnection lines that can be connected to candidate bus x
$N_{L,x}^{min}$	Minimum allowable interconnection lines that can be connected to candidate bus x

ND_j	Number of blocks bid by demand j
NG_i	Number of blocks offered by generator i
$P_{xy}^{dc,max}$	Maximum power capacity of DC line xy
PD^{Max}	Max size of demand bid block
PG^{Max}	Max size of supply offer block
S_{base}	Apparent power base value, in MVA
S_{base}	Network base power, in MVA
$S_{nm}^{ac,max}$	Maximum apparent power capacity of AC line nm
$S_{nx}^{c\text{-}max}$	Interlinking converter rated-power
T_r	Lifetime of component r
V_{base}^{ac}	AC base voltage, in kV
V_{base}^{dc}	DC base voltage, in kV
$C_{G.Db}$	Generation cost (in \$/MWh) of the dispatchable energy resource b
$C_{G.Ra}$	Generation cost (in \$/MWh) of the renewable energy resource a
$C_{L.Mc}$	Cost of curtailing power (in \$/MWh) for participant c enrolling in the load management program
$\blacklozenge^{max}$	Maximum limit of the variable ✦.
$\blacklozenge^{min}$	Minimum limit of the variable ✦.
ND	Number of demand participants
NG	Number of generator participants

Sets

$N^{b}_{\mu G_q}$	Set of buses in μG_q
N^{cand}_{buses}	Set of candidate buses
N^{ac}_{b}	Set of AC buses
N^{dc}_{b}	Set of DC buses
N^{ac}_{G}	Set of AC energy resources
N^{dc}_{G}	Set of DC energy resources
$N^{c}_{\mu G_q}$	Set of AC-DC converters in μG_q
$N^{G,ac}_{\mu G_q}$	Set of AC energy resources in μG_q
$N^{G,dc}_{\mu G_q}$	Set of DC energy resources in μG_q
$N_{\mu G}$	Set of μGs
T_P	The number of years in the planning study
$N_{G.D}$	Set of dispatchable energy resources
$N_{G.R}$	Set of renewable energy resources
$N_{L.M}$	Set of participants in load management program
N_{Loads}	Set of loads

Variables

$(P_{exp.D})_{stage1}$	Power exported by the dispatchable energy resources in Stage 1
$(P_{exp.D})_{stage2}$	Available power of the dispatchable energy resources that can be exported in Stage 2
$(P_{exp.R})_{stage1}$	Power exported by the renewable energy resources in Stage 1
$(P_{exp.R})_{stage2}$	Available power of the renewable energy resources that can be exported in Stage 2

$(P_{imp})_{stage1}$	Power imported by the renewable energy resources in Stage 1.
$(P_{imp})_{stage2}$	Amount of power that should be imported in Stage 2
$(P_{G.D})_b$	Power generated by dispatchable energy resource b
$(P_{L.M})_c$	Power curtailed from load management program participant c
β_{conv}	Power-loss coefficient for the interlinking converters
β_c	Power-loss coefficient for converter c
$\mathbb{E}(C_{OPF,s,t})$	Expected value of the operation cost at year t
$\mathbb{E}(S_{n,s}^{vpv})$	The expected value of $S_{n,s}^{vpv}$
$\overline{A_n}$	Logical inverse of A_n
θ_{nm}	Difference in voltage angle (i.e., $\theta_{nm} = \theta_n - \theta_m$).
θ_n	Voltage angle at bus n, in rad/degrees.
A_n	Binary variable representing bus n type
A_x	Binary variable representing candidate bus x type
A_y	Binary variable representing candidate bus y type
$C_{\mu G_q}^{OPF}$	Operation cost of μG_q
C_r^{rep}	Replacement cost of component r
$C_{OPF,s,t}$	Optimal operation cost (in \$/h) for an MCS scenario s at year t
$C_{AOM,t}$	Annual operation and maintenance costs for year t.
C_{INV}	Total investment costs (i.e., lines, breakers, and converters)
C_{NPV}	Net present value of the system costs (i.e., investment, maintenance, and operation costs)

C_{REP}	Total replacement costs of the system components
H_{nx}^{C}	Binary element of an interlinking converter connected between AC bus n and DC bus x
i_j	Output current of phase j
I_{arm}	Value of the MMC arm current
I_{dc}	DC-grid current
i_{low_j}	Lower arm current of phase j
i_{up_j}	Upper arm current of phase j
K_{nm}	Binary variable representing the connection between bus n and bus m
K_{nm}^{ac}	Binary element of AC line connecting buses n and m.
K_{xy}	Binary variable representing the connection between the candidate buses x and y
K_{xy}^{dc}	Binary element of DC line connecting buses x and y
M_c	Modulation index of the converter c
M_{nx}	Modulation index of the interlinking converter connected between AC bus n and DC bus x
M_{nx}	Modulation index of the interlinking converter connecting buses n and x
P_c^{ac}	Active power at the AC side of the AC-DC converter c
P_c^{loss}	Power losses of converter c
$P_{exp.R}$	Renewable power can be exported by the μG
$P_{G_i}^{ac}$	Active power of AC resource i
$P_{G_j}^{dc}$	Output power of DC resource j

$P_{G_n}^{ac}$	Active power of an AC energy resource connected at bus n
$P_{G_x}^{dc}$	Active power of an DC energy resource connected at bus x
P_{imp}	Power imported by the μG
P_{imp}	Power that should be imported by the μG to maintain its adequacy
$P_{L_n}^{ac}$	Active power demand for an AC load connected at bus n
$P_{L_x}^{dc}$	Active power demand for a DC load connected at bus x
$P_{Lcur,n}^{ac}$	Curtailed active power from AC loads at bus n in the faulty μG
$P_{Lcur,n}^{dc}$	Curtailed active power from DC loads at bus n in the faulty μG
P_{nm}^{ac}	Active power transmitted through the AC line nm
$P_{nx}^{c\text{-}ac}$	Active power at the AC side of the interlinking converter
$P_{nx}^{c\text{-}loss}$	Power loss of the interlinking converter
P_{n}^{cal}	Calculated active power at bus n
P_{n}^{inj}	Active power injected at bus n
P_{rq}	Active power transmitted from μG_r to μG_q
$P_{xn}^{c\text{-}dc}$	Active power at the DC side of the interlinking converter
P_{xy}^{dc}	Active power transmitted through the AC line xy
$PD_{j.k}$	Power block k bid by demand j
$PG_{i.b}$	Power block b offered by generator i
Q_{c}^{ac}	Reactive power at the AC side of the AC-DC converter c
$Q_{G_i}^{ac}$	Reactive power of AC resource i
$Q_{G_n}^{ac}$	Reactive power of an AC energy resource connected at bus n

$Q^{ac}_{L_n}$	Reactive power demand for an AC load connected at bus n
$Q^{ac}_{Lcur,n}$	Curtailed reactive power from AC loads at bus n in the faulty μG
Q^{ac}_{nm}	Reactive power transmitted through the AC line nm
$Q^{c\text{-}ac}_{nx}$	Reactive power at the AC side of the interlinking converter
Q^{cal}_{n}	Calculated reactive power at bus n
Q^{inj}_{n}	Reactive power injected at bus n
$S^{vpv}_{n,s}$	VPV apparent power at bus n for an MCS scenario s
S^{vpv}_{n}	Value of the apparent power of the VPV at bus n
$S^{c\text{-}max}_{c-xy}$	Rated apparent power of the IC required for connecting two different types (AC and DC) of candidate buses x and y
$S_{c\text{-}xy,s}$	Apparent power of the IC connecting two candidate buses x and y for different MCS scenarios
S^{ac}_{c}	Apparent power at the AC side of the AC-DC converter c
$S^{c}_{nx,s}$	Stochastic variable representing the apparent power of the interlinking converter connecting AC bus n and DC bus x for different MCS scenarios
$S^{c\text{-}max}_{nx}$	Rated apparent power of the interlinking converter connecting AC bus n and DC bus x
S^{c}_{nx}	Apparent-power of the interlinking converter connected between AC bus n and DC bus x
V^{ac}_{m}	Voltage magnitude at DC bus m
V^{ac}_{n}	Voltage magnitude at DC bus n
V^{dc}_{x}	Voltage magnitude at DC bus x
V^{dc}_{y}	Voltage magnitude at DC bus y

$V_{C_{k_{low_j}}}$	Instantaneous voltage of submodule k of the lower arm of phase j
$V_{C_{k_{up_j}}}$	Instantaneous voltage of submodule k of the upper arm of phase j
V_c^{ac}	Voltage magnitude at the AC side of converter c
V_c^{dc}	Voltage magnitude at the DC side of converter c
$V_{low_{j_k}}$	Switching functions of lower arm submodule of phase j
$V_{up_{j_k}}$	Switching functions of upper arm submodule of phase j
V_j	Converter output voltage of phase j
V_{dc}	DC-grid voltage
V_{g_j}	AC-side voltage of phase j (j = a, b, c)
$V_{low_j}^{SM}$	Total voltage of lower SMs of phase j
V_{low_j}	Total voltage of lower arm of phase j
$V_{up_j}^{SM}$	Total voltage of upper SMs of phase j
V_{up_j}	Total voltage of upper arm of phase j
J	Social welfare

Chapter 1

Introduction

The generation and distribution of electric power has changed considerably in the last decade due to the growing awareness of the environmental concerns , the development of power electronics technology, as well as government efforts and policy maker initiatives to encourage the use of clean energy. Examples of these policies in Canada, include the feed-in-tariff (FIT) program in Ontario, Canada [1], the community feed-in-tariff (COMFIT) in Nova Scotia, Canada [2], and the Federal Tax Provision for Clean Energy Equipment Federal Tax Provision for Clean Energy Equipment [3]. These developments and government policies have resulted in a global interest in increasing the penetration of renewable energy resources and distributed generations (DGs). In Canada, for example, the installed wind power and solar power capacity have increased significantly, as shown in Fig. 1.1 and Fig. 1.2 [4, 5]. According to Fig. 1.1, the installed wind power capacity has increased from 3,967 megawatts (MW) in 2010 to 13,413 in 2019. While Fig. 1.2 shows that the installed solar power capacity has increased from 221 MWs in 2010 to 3,310 MWs in 2019.

Interestingly, the utilization of many renewable-based DGs in DC systems is more advantageous compared to AC systems. For instance, the integration of a photovoltaics (PV) to a DC system requires two conversion stages to feed a non-linear DC load [6]. However, five conversion stages are needed to feed the same load provided the integration of the PV array to an AC system. As a result, the power conversion efficiency approaches 98 % in DC systems compared to only 86 % in AC systems [6]. Additionally, the modern electrical appliances, such as LED-based lighting, cell phones, PCs, and electronic devices

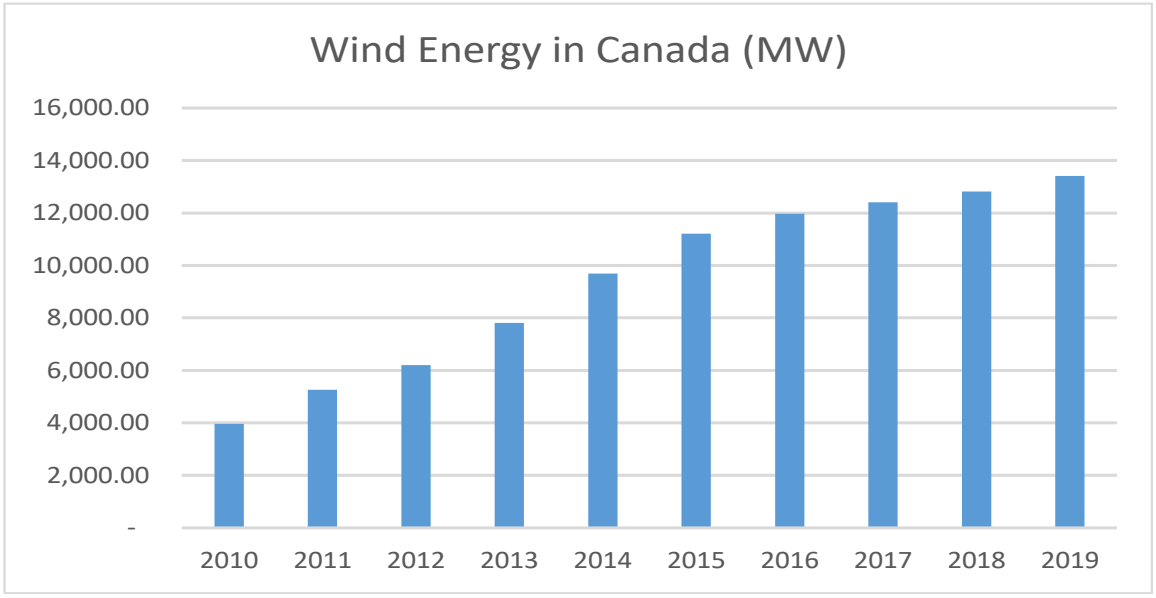

Figure 1.1: Installed Wind Power Capacity in Canada.

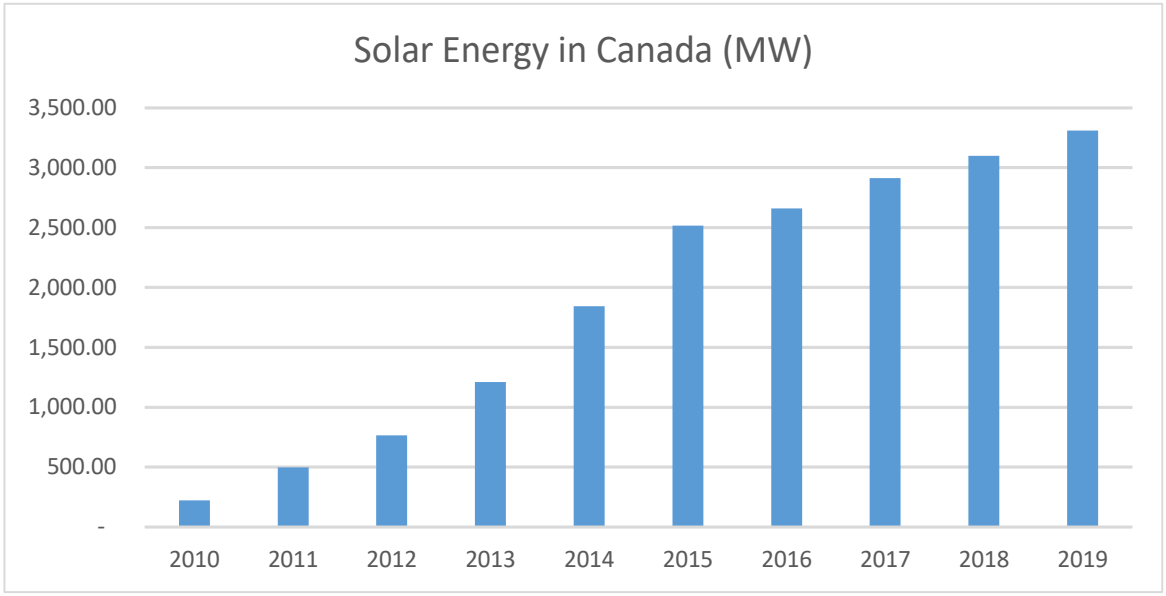

Figure 1.2: Installed Solar Power Capacity in Canada.

are all DC-based loads. Moreover, the electric vehicles (EVs) have attracted academic and industrial attentions, and it is expected to represent one of the main DC loads in the near future, which promotes the implementation of DC systems [7].

Additional considerations include the following beneficial characteristics of DC distribution systems (DSs) compared to AC DSs [8, 9]:

1. Lack of many issues including synchronization problems and reactive power flow
2. Higher power capacity for the same cable sizing
3. Higher system efficiency
4. Absence of the skin effect

The increased penetration of renewable-based DGs has reformed the power system generation to a decentralized generation paradigm, which promoted the implementation of isolated μGs [10, 11]. The construction of these isolated μGs have been initiated as AC networks, and then evolved to include DC and AC-DC hybrid systems in order to accommodate the high penetration of DC-based DGs and loads [12, 13]. However, maintaining the self adequacy of isolated μGs is considered the main challenge due to the probabilistic nature of loads and renewable-based DGs. Hence, the interconnection of isolated μGs is crucial to enhance the system operation and increase the system reliability. This interconnection essentially leads to small-scale energy market of interconnected microgrids (IμGs). Therefore, it is vital to refine and enhance the way in which players from different μGs construct the interconnected μGs and manage electricity trading.

Driven by the benefits of DC systems and the increased penetration of renewable-based DGs, extensive research has been directed to 1) the integration of DC and AC μGs in order to configure a new AC-DC hybrid paradigm and accommodate the increased penetration of DC loads and DGs, 2) the interconnection of isolated μGs, and 3) the direct energy trading between these IμGs.

1.1 Motivation

The growing trend towards the utilization of DC-based DGs, such as PV panels and battery storage systems [14], as well as the expanded DC-based load demand related to components such as EVs and modern home appliances has been promoted by the rising development of the use of DC architectures in DSs. For instance, sales of electric cars globally has increased dramatically from 2010-2019 to boost the stock to 7.2 million electric cars, as shown in Fig. 1.3 [15]. The advent of renewable-based DGs has led to radical changes in the nature of loading resulting in the promotion of the concept of DC systems and isolated μGs for active distribution systems [16, 17].

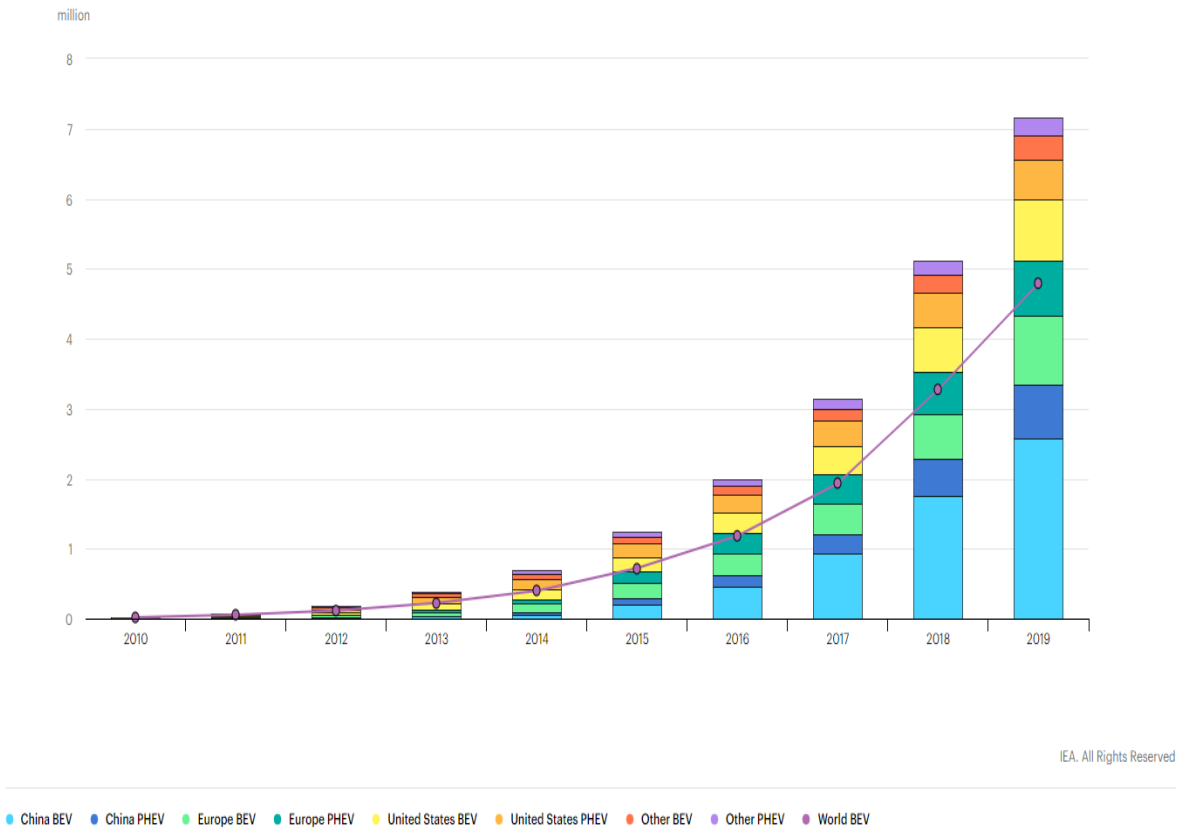

Figure 1.3: Global electric car stock, 2010-2019 [15].

Despite the advantages of the DC systems and the increased penetration of DC-based DGs and load demands, the implementation of a pure DC system is not practical because of two reasons: 1) most planning techniques and electrical standards are appropriate for the AC system, and 2) the existence of high portion of AC-based DGs and loads. As such, the implementation of both systems together is an intermediate solution to acquire the AC and DC benefits, which calls for further research in the area of planning and operation of AC-DC hybrid system.

The concept of isolated μGs has recently attracted significant attention since it provides a viable solution for remote community electrification. Isolated μGs can eliminate investments on additional generation and transmission facilities to supply remote loads. Recent publications have addressed several operational and planning issues in isolated μGs. Operational studies include modelling and energy management. Additionally, load flow and stability have been extensively performed for the different isolated μGs structures [18, 19]. However, the planning studies are performed mostly for AC μGs.

Given the aforementioned discussion, the benefits of μGs make them a perfect host for high penetration of renewable energy resources. However, preserving the adequacy of μGs represents a main challenge as μGs are dominated by renewable-based DGs. These renewable-based DGs are characterized by their probabilistic nature, and hence the interconnection of isolated μGs is crucial in enhancing the system operation and increasing the system reliability. This interconnection essentially leads to a small scale energy market of IμGs, which calls for further research to construct the interconnected μGs and manage their electricity trading.

1.2 Research Objectives

The main goal of this thesis is facilitating the utilization of μGs by addressing and providing solutions to the challenges associated with their implementation. In order to achieve this goal, new μG configuration as well as new methodologies for the planning and operation of AC-DC bilayer μGs are developed in this thesis. In this context, the main objectives of the research conducted in this thesis are shown in Fig. 1.4, and can be summarized as follows:

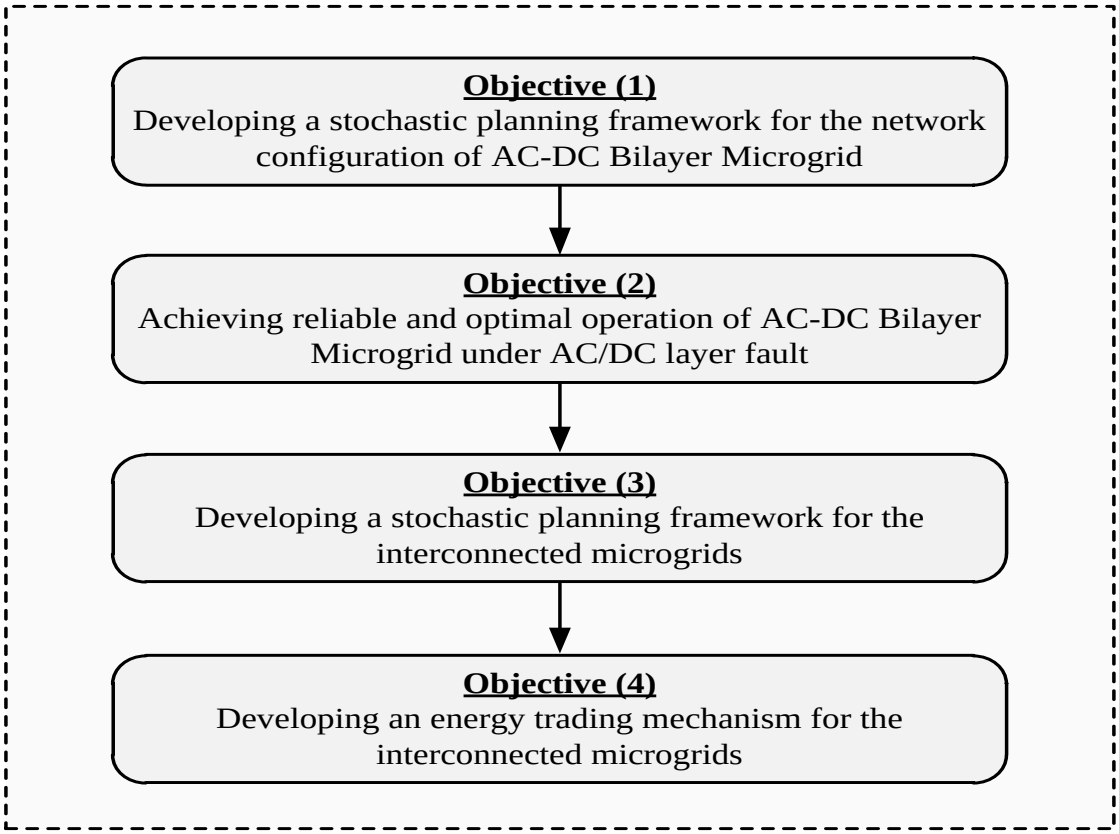

Figure 1.4: Research Objectives.

1. Promoting and enhancing the AC-DC bilayer microgrid configuration that can optimally accommodate the increased penetration of the DC-based DGs and loads and reduce the number of interfacing converters. Additionally, developing a stochastic planning framework for BμG that is capable of minimizing the total system costs through the determination of the optimal BμG configuration.

2. Investigating the AC-DC bilayer microgrid operation under fault conditions, derive the fault current equations and proposing modular multilevel converter (MMC) as interlinking converter for AC/DC microgrids in order to utilize its fault confining capability in eliminating the fault current contribution between the AC and DC layer of the bilayer μG.

3. Developing a stochastic planning framework for interconnected microgrids. The planning framework minimizes the total system costs, minimizes the loads curtailment under DG failure, and maximizes/minimizes the μG capability to export/import power. These objectives are achieved through the determination of interconnection buses and optimal interconnection configuration.

4. Developing a dual action trading mechanism (DATM) that facilitates and arranges the power trading between the interconnected microgrids. The mechanism includes two trading stages, the first stage is the conventional trading at which the μGs submit their bids/offers based on surplus power or load demand, while the second stage provides the μGs with the chance to adjust their bids/offers in Stage 2. This adjustment would ensure full utilization of the renewable output power and minimization of load curtailment, and hence maximization of the social welfare.

1.3 Thesis Outlines

The remainder of this thesis is organized as follows:

Chapter 2 includes the background and literature review of the previous work implemented in the field of 1) planning and operation of AC-DC hybrid μGs, 2) protection of μGs, 3) interconnection of μGs, and 4) energy trading among IμGs.

Chapter 3 introduces the AC-DC bilayer microgrid configuration that facilitates the integration of loads and DGs of different power types (AC and DC) by connecting all the AC/DC loads and DGs directly to the corresponding AC/DC layer. Additionally, this chapter presents the planning framework that is used to achieve the optimal operation of this bilayer configuration. The framework determines the optimal BμG configuration that minimizes the system total costs by providing the following decisions: the AC-layer connection; the DC-layer connection; and the number, locations and sizes of the ICs.

Chapter 4 presents a mathematical formulation for the fault current calculation in the interlinked BμGs. It also presents a solution for the fault current elevation in BμGs through the utilization of a novel IC topology, which is capable of isolating the two layers under faults conditions using innovative configuration and power electronic switches.

Chapter 5 provides a planning framework for interconnected microgrids. The planning framework determines the optimal interconnected microgrids configuration that minimizes the installation and operation cost to provide the following planning decisions: the interconnection buses of each μG; the interconnection lines that will form the IμG network, the types of these lines (AC/DC); and the locations and sizes of the interlinking converters used to interconnect two μGs of different types of power (AC/DC).

Chapter 6 introduces a dual action trading mechanism that facilitates the power trading between the IμGs. This mechanism provides employs two trading stages. Stage 1 is the conventional trading at which the μGs submit their bids/offers to the interconnected system operator to determine the trading price and the amount of power exchange. Afterwards, the μGs are given the chance to participate in Stage 2 by submitting new offers/bids, however, they also have the option to not participate (i.e. Do nothing). Stage 2 results in a decrease in the μGs operation cost, reduces the renewable power curtailment, and maximizes social welfare.

Chapter 7 sets out the thesis conclusions and contributions as well as recommendations for future research studies.

Chapter 2

Background and Literature Survey

2.1 Introduction

As mentioned in Chapter 1, AC-DC hybrid configurations are the core of future systems due to their capability in providing optimal accommodation of AC/DC DGs and loads. Moreover, interconnecting the μGs and manage the energy trading between them would have significant benefits including reduction in the energy costs and proper managing for the uncertainty of renewable-based DGs. These beliefs heighten the need for reliable appropriate techniques for the planning, operation, and energy trading of future μGs, as was highlighted in the research objectives in Chapter 1.

This chapter presents the required background and literature survey related to the thesis objectives. The first section, Section 2-2, presents an overview of the different types of the AC-DC hybrid power systems that have been discussed in the literature. Section 2-3 discusses the operation and control of AC-DC hybrid μGs. Section 2-4 and 2-5 review the planning and protection techniques used for AC-DC hybrid μGs. Previous research works conducted for the interconnection of μGs and their energy trading are discussed in Section 2-6 and 2-7, respectively. Finally, the conclusions and discussions of this chapter are presented in Section 2-8.

2.2 AC-DC Hybrid Systems

In this section, the different topologies for the utilization of the DC power in the transmission and distribution systems are discussed. The three systems are: 1) high voltage direct current (HVDC) transmission systems, 2) AC-DC hybrid microgrids, and 3) low voltage direct current (LVDC) distribution systems. A review of the state of the existing AC-DC hybrid systems configurations is presented.

2.2.1 HVDC Transmission Systems

HVDC systems are considered the first AC-DC hybrid configuration, where the first project was implemented in 1954 in Sweden. Since then, researchers have been concerned with the HVDC transmission along with its various applications in the electrical power system due to the their significant features [20–23], such as:

1. HVDC systems are characterized by their ability to transmit power over long distances at low cost compared to high voltage alternating current (HVAC).
2. HVDC systems do not suffer from stability problems.

Due to the aforementioned features, the implementation of HVDC systems has increased dramatically and different configurations including 1) point-to-point transmission, 2) back-to-back, and 3) multi-terminal, as shown in Fig. 2.1, were implemented depending on the desired application.

The full scale review of this type of system is outside the scope of this thesis, however, few observations on the recent trend in the planning of this system is discussed in the literature. The planning of the point-to-point and multi-terminal DC transmission was presented in [24]. An expansion planning algorithm for the AC-DC hybrid transmission is presented in [25]. The algorithm purposed is to select the optimal combination of AC-DC transmission links. However, the main drawback of the presented expansion planning algorithm is the limitation of the considered scenarios, and hence the optimal solution is not guaranteed.

Ref. [26] proposed an optimal power flow model for a multi-terminal voltage source converter (VSC) HVDC based system. The minimization of the generation cost and the active power losses are the objective functions of that model. The solution is obtained by considering different planning scenarios. Each scenario represents a possible installation of a multi-terminal DC system into the existing AC grid in order to find the final planning scenario. The model was not concerned with the uncertainties due to wind energy sources.

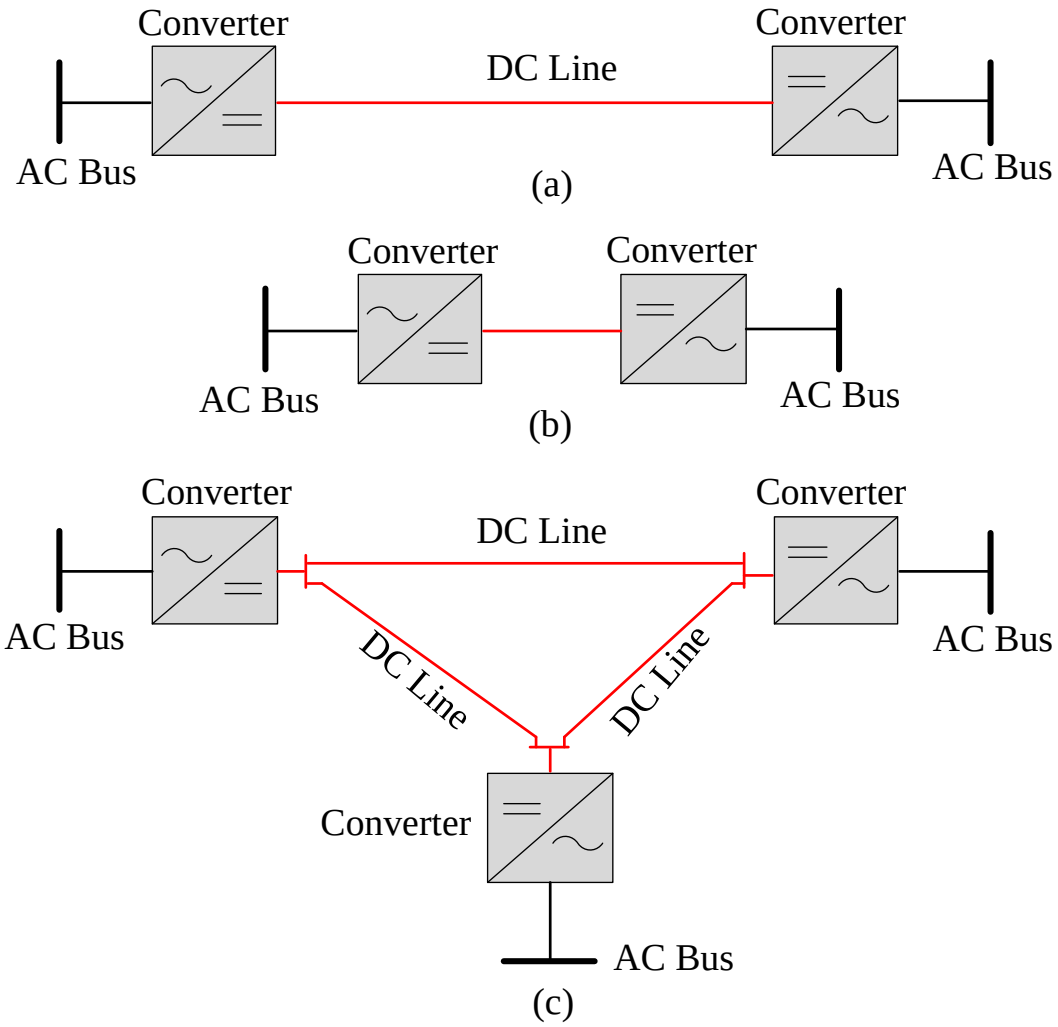

Figure 2.1: HVDC Connections: (a) point-to-point transmission (b) back-to-back (c) multi-terminal HVDC.

2.2.2 AC-DC Hybrid Microgrids

The integration between AC and DC systems has been introduced as an intermediate solution to acquire both the AC and DC benefits, which is referred to as AC-DC hybrid microgrid (HμG) [27–29]. A HμG is a μG that combines both AC and DC systems, where all system components including AC/DC loads, AC/DC renewable-based distributed generations (DGs), dispatchable DGs, and energy storage systems are clustered into AC/DC subgrids. The AC and DC subgrids are connected by an interlinking converter (IC) [30,31], whose function is to compensate for any power mismatch between the two subgrids, as shown in Fig. 2.2.

It is worthwhile to note that clustering the system components into the AC/DC subgrids is appropriate for small areas. However, this clustering topology is not technically feasible for large power grids.

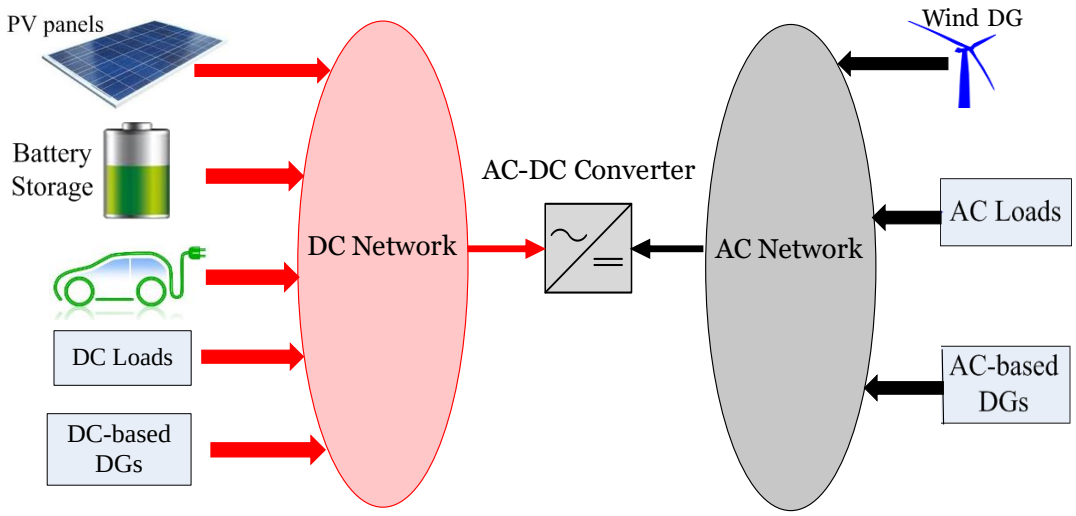

Figure 2.2: General architecture of AC-DC hybrid microgrids.

2.2.3 LVDC Distribution Systems

The development in power electronics technology and renewable based-DGs led to a significant increase in the utilization of DC loads and DC DGs. As such, great attention has been directed to DC distribution systems (DS), as will be discussed in the literature.

References [32, 33] discussed the techno-economic analysis of LVDC systems. The two main LVDC configurations, shown in Fig. 2.3, were investigated in [33]. As shown in Fig. 2.3-a and Fig. 2.3-b, the two configurations are different in terms of the DC links and DC/AC converters locations and sizes. The analysis in [32, 33] revealed that although LVDC system protection and operation is more complex compared to conventional AC grid, the LVDC is better than the conventional AC grid in terms of: 1) transmission capacity, 2) power quality, and 3) power losses.

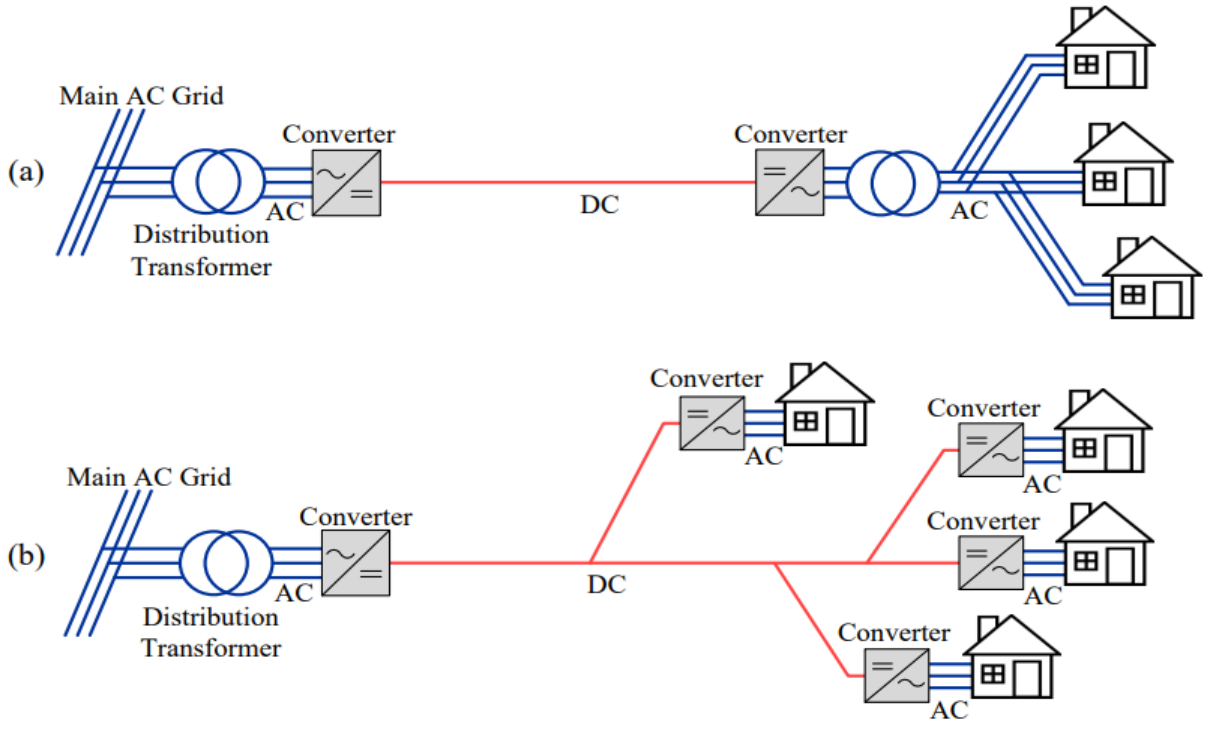

Figure 2.3: LVDC topologies presented in [33].

2.3 Operation and Control of AC-DC Hybrid Microgrids

2.3.1 Control Techniques for DGs

Various control techniques are implemented for DGs and energy storage systems ESS to ensure appropriate load sharing and avoid overloading. This subsection review the common control techniques.

I. PQ Control

In PQ control, the interfacing-DG inverter is acting as a current controlled voltage source. The inverter is controlled in order to inject certain amount of active and reactive power into the grid whose reference values of P and Q (i.e. P* and Q*) are sent from the supervisory central controller of the μG (μGCC). The PQ control scheme is shown in Fig. 2.4 [34].

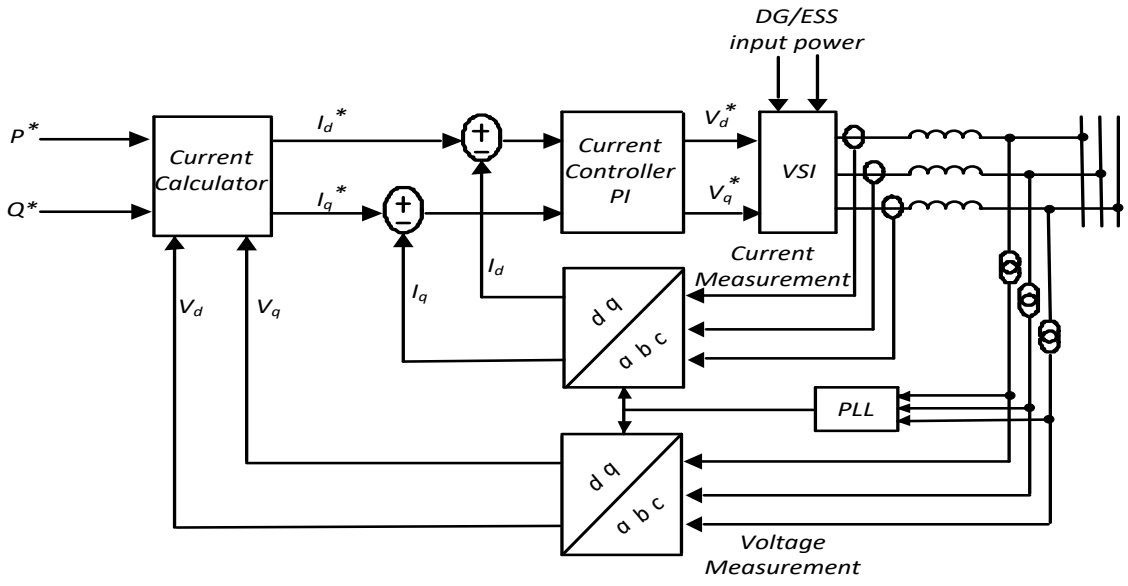

Figure 2.4: PQ Control of Inverter-Interfaced DG/BESS.

II. Droop Control

The droop control is implemented to avoid the DGs overloading by ensuring the power sharing among the existing DGs without communication due to the utilization of the AC system frequency and voltage in setting the output active and reactive power respectively as expressed in (2.1) and (2.2). The block diagram of the AC droop control is shown in Fig. 2.5.

$$\omega = \omega_o + K_p P \tag{2.1}$$

$$V = V_o + K_v Q \tag{2.2}$$

Unlike the AC droop, the DC droop relates the injected power to the voltage as expressed in (2.3) and (2.4) [35].

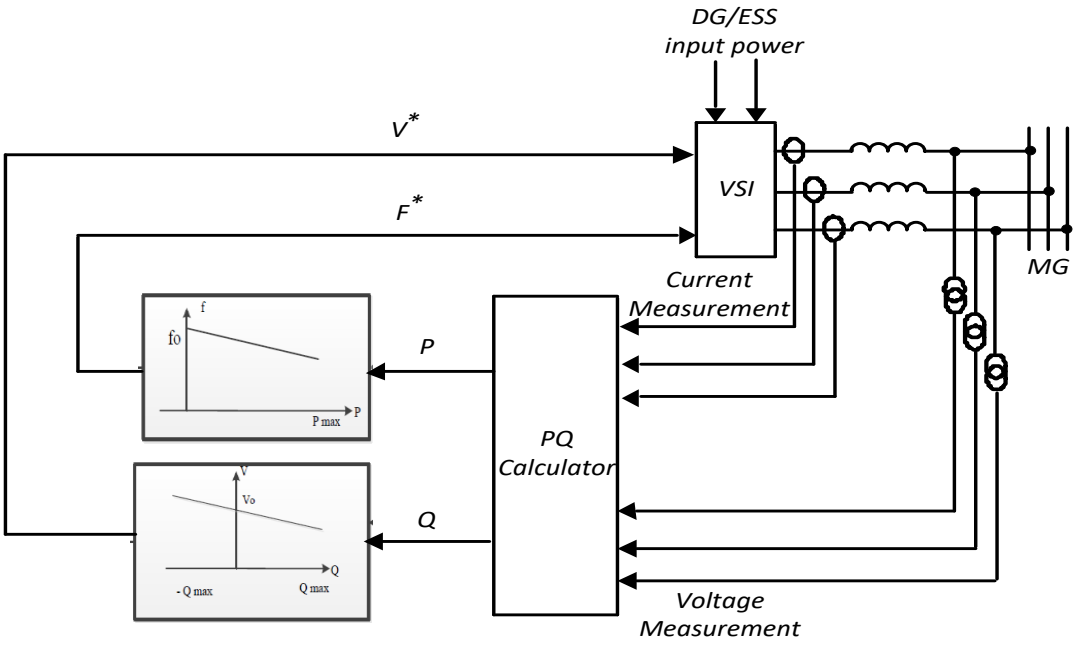

Figure 2.5: Inverted Interfaced DG/ESS Droop Control.

$$V_{dc} = V^* + K_{dc}P_{dc} \tag{2.3}$$

$$K_{dc} = \frac{P_{dc,max}}{V_{dc,max} - V_{dc,min}} \tag{2.4}$$

III. PV Control

In PV control, the active power and voltage at the point of common coupling PCC are feedback to generate the control reference signals. Consequently, the voltage at the PCC is controlled by the DG, however, the active power balance controls the frequency. The PV block diagram is given in Fig. 2.6 [36].

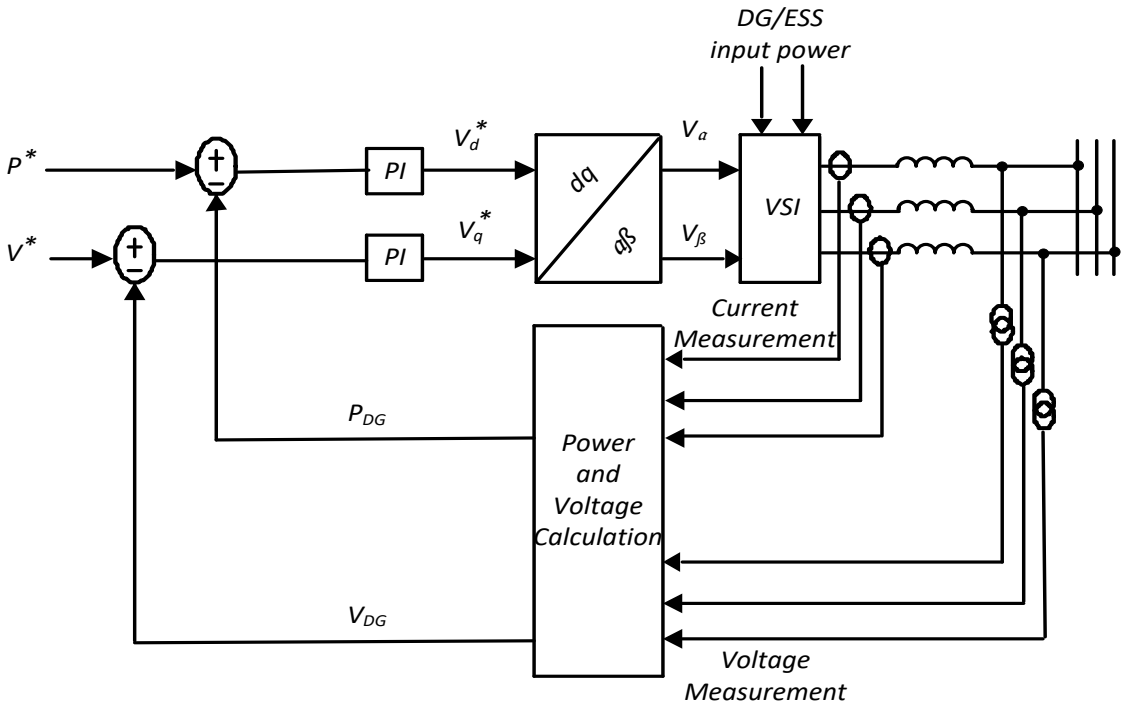

Figure 2.6: Inverted Interfaced DG/ESS PV Control.

2.3.2 Operational Modes for Hybrid AC-DC Microgrids

The generation capacities of the Hybrid AC-DC μGs DGs and the availability of the connection to the main grid determine the μG operation mode as follows:

1.3.2.1 Grid Connected Hybrid Systems

This mode of operation includes the connection of the μG to the main grid. Consequently, the AC subgrid is considered stiff which acts as a slack bus for the DC subgrid that is capable of supplying any power mismatch between the generation and load as shown in Fig. 2.7. The DC and AC subgrid are studied separately due to the availability of slack bus (AC subgrid and main grid).

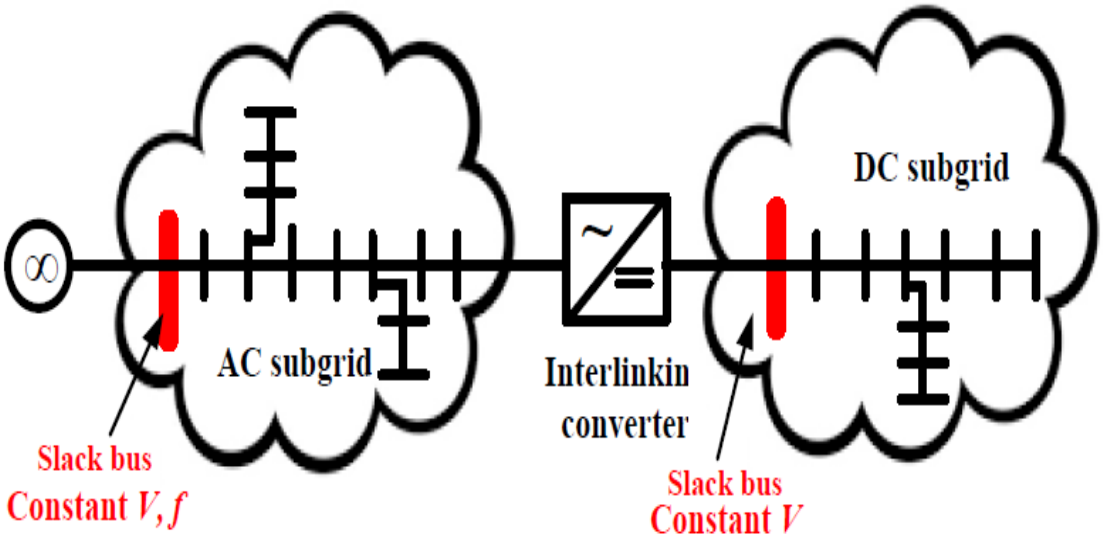

Figure 2.7: Grid Connected Hybrid Microgrid.

1.3.2.2 Islanded Hybrid Systems

This mode of operation does not incorporate connection to the main grid. On the other hand, the AC and DC subgrid are still connected. This mode of operation has various operation scenarios based on the DGs generation capacities as follows:

I. Islanded Hybrid system with stiff AC subgrid [37]

In this scenario, the generation capacity of the AC subgrid is high enough to act as a slack bus for the DC subgrid. As a result, the AC subgrid regulates the DC subgrid voltage by injecting proper active power. Droop control is implemented to maintain the load-generation balance in the AC subgrid while the DGs in the DC subgrid will be operated as constant power.

II. Islanded Hybrid system with stiff DC subgrid [38]

Conversely, the generation capacity of the DC subgrid is high enough to act as a slack bus for the AC subgrid. As a result, the DC subgrid regulates the AC subgrid voltage and frequency by injecting proper reactive power and active power. Droop control is implemented to maintain the load-generation balance in the DC subgrid while the DGs in the AC subgrid can be operated in the PV or PQ control mode.

III. Islanded Hybrid Systems

In this scenario, the generation capacity of the DC and AC subgrid are not enough to act as a slack bus for the AC subgrid. As a result, the AC subgrid frequency is linked to the DC subgrid voltage through the IC to allow the DGs in both grids to share the load. If the load in the DC subgrid increases, the DC subgrid voltage will decrease and thus the AC subgrid frequency drops which increases the injected power of the AC subgrid DGs. Similarly, if the load in the AC subgrid rises, the AC subgrid frequency will decrease resulting in a reduction in the DC subgrid voltage and thus the injected power of the DC subgrid DGs would increase. The schematic diagram of the islanded hybrid system with limited AC and DC capabilities is shown in Fig. 2.8 [38]. The role of the IC is to equalize the per unit voltage of the DC subgrid with the per unit frequency of the AC subgrid [38].

1.3.2.3 Isolated Hybrid Systems

In this scenario, the Hybrid μG is no longer connected to the grid and the two subgrids are isolated. Therefore, each μG will operate independently.

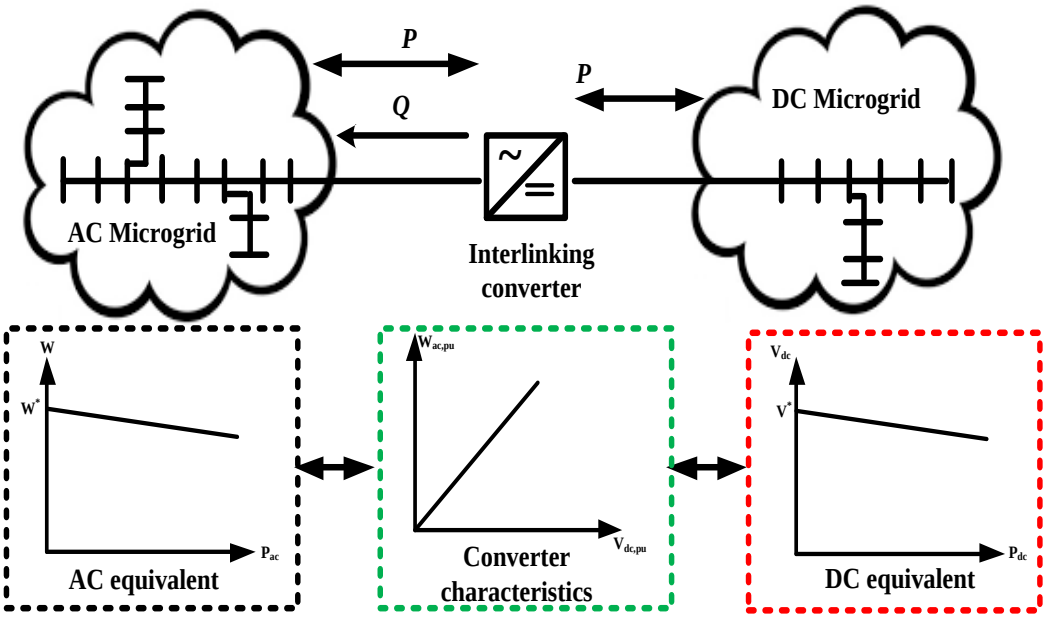

Figure 2.8: Isolated Hybrid AC-DC Microgrid

.

2.4 Planning of AC-DC Hybrid Microgrids

AC-DC hybrid microgrids have gained considerable attention in the academia due to their integration to the AC and DC systems, as well as the high penetration of DC DGs and DC loads. However, the techno-economic benefits of HμGs need further investigations to allow for the widespread of this technology [39–41]. Consequently, it is beneficial to introduce an efficient planning model in order to reduce the system cost and ensure the economic viability of the HμG. In contrast to the research in the AC μG, the research in the HμG planning is still limited and this will be elaborated on the following literature.

The authors of [42] introduced a planning model that specifies the optimal location and size of each distributed energy resources DERs, and in [43], they extended their work by specifying the type of each individual feeder. However, in both [42] and [43], the authors ignored the reactive power demand and the stochastic natures of the renewable resources,

and hence provided unrealistic solutions.

The planning of isolated HμGs has been addressed in [44] and [10]. The authors of [44] proposed a planning algorithm that was formulated as a mixed integer non-linear program. Locating and sizing the μG equipment that facilitate the access of fuel to remote communities, in addition to the determination of the μG configuration (AC, DC, or Hybrid AC-DC) were the model objectives. In this work, the authors assumed a fixed radial network and they tried to determine the optimal type (AC/DC) of the network buses and lines. In [10], a planning model was proposed to minimize the total planning cost by providing 1) the optimal μG configuration and 2) the optimal sizing of DERs and ICs. However, this model dealt with the μG as a clustered zone of DGs and loads, and thus did not consider: 1) the μG configuration and its effect on the power flow and losses, 2) the capacities of the network lines, and 3) the voltage limits of each bus. Moreover, it determines the type of the μG, which can be AC, DC, or AC-DC hybrid, but it does not determine the μG configuration (i.e., the type of buses, the type of lines, and their connection).

In another work [45], a stochastic planning model was proposed for minimizing the operation and installation cost of HμGs. In order to achieve this objective, the model searches for the optimal network configuration determined by the types (AC/DC) of the network buses and lines, in addition to the network connection.

The AC-DC hybrid configuration has shown significant benefits for the planning of new areas that have high penetration of DC DGs and loads. However, the AC-DC hybrid configuration is not the optimal configuration for the power system reinforcement and upgrade since it is not capable of fully utilizing the existing assets in the system. The AC-DC hybrid configuration planning for existing areas is based on replacing some of the existing AC parts in the system with DC, and hence the existing AC assets are not properly utilized.

Given the aforementioned discussion, further research in the AC-DC configurations is required to fill the gaps of the existing AC-DC hybrid configuration. As a result, this thesis proposed the AC-DC bilayer microgrid BμG configuration that allows the two types of power (AC and DC) to be available at each node in the system, which would achieve significant benefits in terms of optimal accommodation of different types (AC/DC) of loads and DGs, in addition to proper utilization of the existing assets, as will be illustrated in

Chapter 3.

2.5 Protection of AC-DC Hybrid Microgrids

The interest in μGs has emerged significantly motivated by their capability in harnessing the advantages provided by DERs. However, the existence of DERs, various μGs operational modes, and different network configurations of μGs presents several challenges to the grid. One of these challenges is the change in the fault current level. Accordingly, conventional over-current protection schemes, which assume unidirectional power flow, are not capable of protecting μGs against various fault scenarios [46].

The following issues make protection of microgrids rather uniquely challenging.

1. The level of the fault current in μGs in grid-connected mode is substantially different from that in islanded mode.
2. The existence of bulk generation units in the power system grid along with the possibility of blackouts as a result of grid protection failures justify the huge investment in macrogrids to develop resilient protection systems. In contrast, the failure of a μG does not impact a wide area, which limits the investment in microgrid protection.

For these reasons, introducing a protection scheme that is capable of responding properly to faults in both grid-connected and islanded/isolated modes is considered one of the main challenges [47].

Many works have been concerned with the fault current calculation in grid connected AC microgrids [48–52]. For instance, in [48], the conventional fault analysis method was modified in order to consider the fault current contribution of inverted based distributed generators. In [49, 50], the application of inverter-interfaced distributed generation units in the fault analysis was introduced. A steady state power flow analysis model for the DG sources as well as fault current calculation of microgrids was introduced in [51, 52]. However, this thesis is concerned with isolated μGs, and hence focusing on protection schemes for isolated μGs.

2.5.1 Isolated Microgrids

The droop control is one of the common control techniques implemented in isolated HμGs to provide load sharing between the various DGs. Despite the significant advantages of the droop control, it results in load sharing not only under normal conditions, but also for fault scenarios. Thus, all DGs will contribute into the fault. For that reason, the calculation of the fault current is crucial in the design of the protective components.

The high contribution of the healthy subgrid DGs current into the faulty subgrid may result in a damage of the semiconductor devices in the IC. Therefore, the isolation of both subgrids is essential to eliminate the contribution of the healthy subgrid. However, the conventional VSCs does not provide isolation during faults since it provides a path for the fault current through their antiparallel diodes, which causes the converter to act as uncontrolled rectifier even when the gating signals of the valves are turned off [53]. To overcome this problem, the DC side is integrated with solid state dc circuit breaker. Unfortunately, DC circuit breakers cost are relatively high and these breakers introduce high conduction losses [54]. Thus, it is not the vital solution. Another approach depends on the AC side circuit breakers to achieve the required DC protection by opening the breakers and isolating the DC side from AC side [55]. Thus, the contribution of the AC side current into the fault is prevented. However, this introduces a risk to the semiconductor devices due to the fast recovery characteristics of the antiparallel diodes. Thus, they may get damaged before the circuit breaker trips.

2.6 Interconnection of Microgrids

Interconnected microgrids IμGs are formed when two or more microgrids are connected together, as shown in Fig. 2.9. The interconnection of μGs was proposed as a promising solution not only for remote areas that do not have access to the main grid, but also to areas with two or more μGs [56]. This interconnection of μGs would enhance the system operation and reduce the effect of the renewable-based DGs indeterminacy through the exchange of power within the IμGs. The interconnection of μGs provides numerous advantages including improved power quality, self-healing, and reliability, and reduction of DGs power curtailment [57].

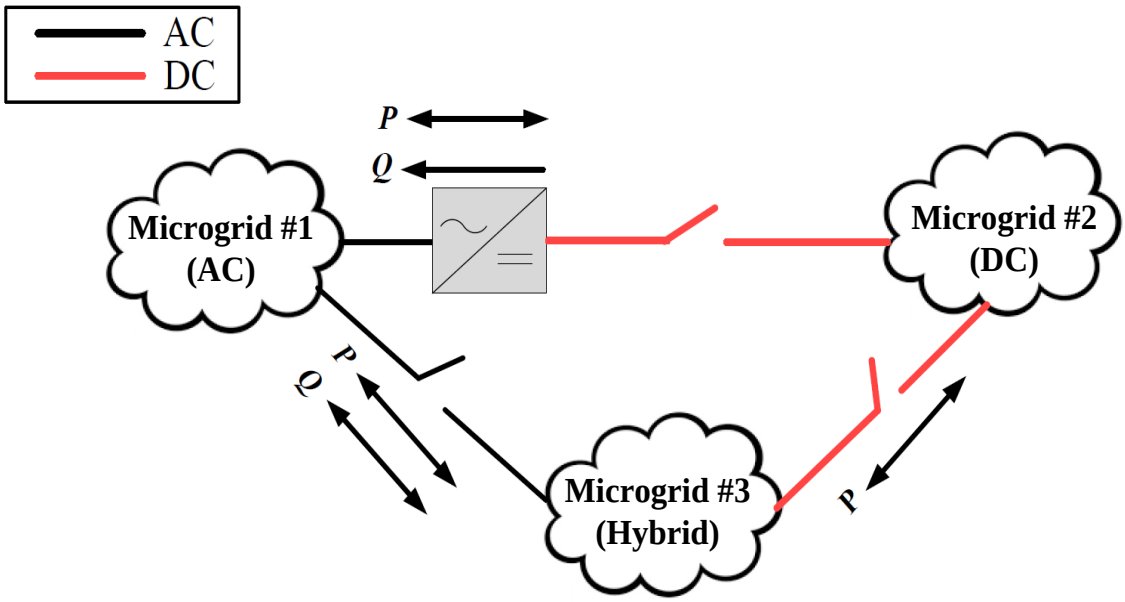

Figure 2.9: Interconnected Microgrids

.

The utilization of more DGs, liberalization of energy market, and improvement in communication technology facilitated and promoted the concept of the IμGs. Accordingly, extensive research has been directed to IμGs as will be elaborated in the following literature review. In [58] an operation strategy that interconnects the neighboring μGs was proposed in order to improve the distribution system self-healing under faulty conditions. The authors in [59] addressed the power trading between groups of IμGs. Reference [60] studied the operation of a network of μGs and presented a control strategy for their power flow. The control of the DGs converters' in IμGs to ensure proper load sharing was addressed in [61]. The necessary conditions to interconnect two or more μGs were presented in [62], while the stability analysis of IμGs prior to their interconnection was discussed in [63]. The work reported in [64, 65] were concerned with investigating the selection of the μGs, among an existing interconnected network, prior to their interconnection. The cooperative power dispatching of multiple IμGs, with a common operator coordinating the μGs, was studied in [66]. References [67, 68] studied the direct interactions among interconnected

isolated μGs. A planning model at which the IμGs cooperate to ensure proper operation of the system of IμGs was proposed in [69]. This cooperation is achieved through the determination of the optimal renewable-based DGs capacities, charging and discharging of energy storage units, and energy trading.

Although few research works studied the planning of IμGs, none of these works were concerned with determining the optimal network configuration of the IμGs in terms of the interconnection lines, line types, and sizing of the ICs connecting different types (AC, DC, or AC-DC Hybrid) of μGs. To the best of the author knowledge, the optimal planning of the network interconnection for multi-μGs was investigated only in [57, 70].

Reference [70] presented a novel stochastic multi-objective framework for optimal dynamic planning of IμGs through: 1) sizing and locating the DGs and ESSs, 2) determining the types and numbers of the DGs and ESSs and 3) specifying the electrical boundaries of the μGs through allocating the section switches. This framework considered an existing conventional distribution network, which was turned into active distribution network to form sets of IμGs through the allocation of the section switches. In other words, in this paper, the DS is already existing and they just insert switches to define new set of microgrids. As such, the authors did not plan the interconnection network and did not determine the optimal locations and sizes of the lines/converters of the interconnection network. Furthermore, the authors did not consider the different types of microgrids (AC, DC, and AC-DC hybrid).

The authors in [57] introduced an optimal planning model of μGs interconnection. However, this paper did not consider the following:

1. It considered only AC μG and it neglects all other types of μGs (DC and/or AC-DC hybrid). Choosing only AC μG limits the role of the type of of the lines connecting the different μGs on the optimum operation of the whole system.

2. It did not consider the active and reactive power losses in the lines and hence did not depict the proper operation of the IμGs.

3. It did not consider the network connection of each microgrid, thereby ignoring the active and reactive power losses in each μG, which questions the feasibility of the obtained solution.

According to the aforementioned discussion, the research in the area of interconnected microgrid planning still lacks the consideration of different types of microgrids and the operation constraints in isolated microgrids.

2.7 Energy Trading

As mentioned earlier in the previous section, the interconnection of μGs is beneficial as it enhances the system operation, reduces the effect of the renewable-based DGs indeterminacy, and reduces the μG's operation cost without the dependency/connection on/to the main grid by facilitating the direct exchange of energy between these interconnected microgrids (IμGs) [71, 72].

The direct trading of the IμGs provides significant benefits to the sellers and buyers (i.e. μGs) compared to their trading with the utility [73] that can be summarized as follows:

1. Regulating and balance energy generation/consumption in microgrids
2. Reducing transmission losses compared to trading with the utility
3. Reducing electricity cost by enhancing the electricity price competitiveness
4. Promoting the utilization of renewable-based DGs
5. Providing an investment opportunity to communities by creating new jobs and promote electricity trading within the μGs rather than with the utility

Despite the significant benefits provided by μGs direct trading, the design of energy trading mechanism is associated with several challenges. μGs are independent entities with different objectives, and thus μGs will interact and trade with each other only if such interactions results in further benefits. In this context, References [74–76] applied an auction mechanism for direct trading between IμGs in order to match the buyers and sellers. While, a collaboration between the μGs to collectively trade energy with the power grid and divide the revenue based on each μG contribution, was proposed in [77–79]. However, this cooperative model does not result in high profit and is associated with high risk as it

requires fair cooperation between different μGs participants. Finally, a cooperative power dispatching in IμGs was presented in [80]. However, the authors in this work assumed that μGs are controlled by a common operator and they cooperate to minimize the total operation cost without considering the benefits of interaction for each μG.

In contrast to the research conducted in the aforementioned works [74–80] that assumed the existence of main grid, other studies have investigated the direct trading between isolated IμGs [81,82]. The direct energy trading between two isolated μGs was investigated in [81], while the energy trading among a group of IμGs was studied in [82]. Both [81] and [82] formulated the problem as a convex optimization whose objective was the minimization of the global cost, and hence did not consider the self-interests of each μG.

Recently, there have been significant theoretical advances in the design of matching markets with contracts. The matching markets involves trading arrangements between group of agents through negotiations between each two agents [83]. It is worthwhile to note that the existence of stable outcomes is essential in order for the trading arrangement to be beneficial to all participants. In [84] and [85], markets with cyclical contractual relationships are considered, where a pair of agents may simultaneously buy inputs and sell outputs to one another.

The aforementioned literature have discussed the various trading mechanism for grid-connected and islanded μGs. However, none of these works have provided a promising solution in isolated μGs that can minimize load curtailment and the renewable-based DGs curtailment given their stochastic variations, which requires further investigation for trading mechanisms in isolated μGs.

2.8 Conclusions and Discussions

According to the aforementioned literature survey, μGs have emerged as dominant platforms for effectively accommodating the high penetration of renewable-based DGs and EVs. Furthermore, the utilization of DC technology is gaining significant attention due to the increased penetration of DC DGs and DC loads resulting in further interest in AC-DC hybrid configurations in order to incorporate the benefits of both AC and DC power. However, from the planning perspective, most hybrid planning methods presented in the

literature have focused on HVDC systems. These methods are dependent on prioritization of the solutions of a limited number of candidate scenarios. This approach does not allow the inclusion of all possible AC-DC configurations, thereby limiting the chances of finding superior solutions. Therefore, a novel stochastic planning framework is proposed, for bilayer μG, in Chapter 3 to determine the optimal AC/DC network configuration that minimizes the system costs. Although many research work investigated the protection of AC-DC hybrid μGs configurations, none of these works provided a solution for the fault contribution from AC subgrid to DC subgrid through the interlinking converter. This gap is addressed in Chapter 4 through the utilization of a novel modular multilevel converter with fault confining capability that prevents the fault contribution from AC subgrid to DC subgrid and vice versa using its power electronic devices. From the aforementioned literature survey, it has been shown that the interconnection of μGs would add considerable advantages to the system operation. However, the research in the optimal interconnection of μGs is still lacking and none of the implemented research has considered the internal network of each μGs and the various types of μGs (AC, DC, AC-DC hybrid, or bilayer). As a result, Chapter 5 introduces a reliable planning model that searches for the optimal interconnection of the μGs. The interconnection of the μGs would allow them to exchange energy with each other, which forms a small-scale electricity market for the IμGs. Consequently, Chapter 6 proposes an energy trading mechanism that facilitates the power exchange between the ImuGs, and defines the role of each participant.

Chapter 3

A Planning Framework for AC-DC Bilayer Microgrids

3.1 Introduction

This chapter introduces a novel stochastic planning framework for AC-DC bilayer microgrids, which facilitates the integration of different types (AC and DC) of loads and DGs. The BμG configuration proposed in this thesis consists of 1) an AC layer, in which AC loads and DGs are connected to AC buses, 2) a DC layer, in which DC loads and DGs are connected to DC buses, and 3) interlinking converters (ICs) that facilitate the connection between the AC and DC layers. Depending on the types, locations, and specifications of the μG loads and DGs, the planning framework allows each node to be a universal node that can include two buses (AC and DC) or a single bus (AC or DC). The network wiring can also be universal (AC, DC, or both) to facilitate the connection between the system nodes. Accordingly, the BμG is composed of universal nodes (AC/DC), universal wiring system (AC/DC), and IC(s), and therefore it is a new and improved design of future smart systems.

Achieving the proper and optimal operation of this bilayer configuration requires an efficient planning framework in order to determine the optimal configuration that achieves the aforementioned benefits. Therefore, a planning framework for the BμG is proposed in

this chapter. The proposed framework takes into account the stochastic variations in load demands and renewable-based DGs through the use of an Monte-Carlo simulation (MCS) technique, to achieve reliable and realistic planning solution. The network connection, as well as the allocation of the ICs play an important role in optimizing the total cost of the BμG. Consequently, the proposed planning framework solves the planning problem by providing the following decisions: 1) the optimal connection of the AC layer, 2) the optimal connection of the DC layer, and 3) the optimal number, sizes, and locations of the ICs.

Various case studies have been implemented and solved using different μG configurations to demonstrate the effectiveness of the proposed framework and the benefits of the BμG.

This Chapter is organized as follows: Section 3.2 and Section 3.3 describes the network configuration and the load flow (LF) model of the BμG, respectively. Section 3.4 formulates the planning framework and the associated optimization problem. The illustration of the planning framework, along with a pseudo code describing the planning strategy is presented in Section 3.5. Section 3.6 describes the case studies that were employed for evaluating the benefits of the BμG configuration. Finally, the Chapter is concluded in Section 3.7.

3.2 Description of the AC-DC Bilayer Microgrid

In the BμG, each node is a universal node that can include two buses with different types of power (AC and DC) or a single bus (AC or DC). The BμG has also a universal wiring system (AC and DC) that allows for 1) the connection of the AC DGs and loads to the AC-layer buses that are connected through AC lines, and 2) the connection of the DC DGs and loads to the DC-layer buses that are connected through DC lines, thereby eliminating the need for interfacing converters. As a result, the configuration of the AC layer can be different from the DC layer in terms of the lines and buses. The possible connection between the AC and DC layers is achieved through the installation of ICs.

It should be noted that the existing μG configurations adopt single layer architecture at which all the DGs and loads are connected to one layer, which can be AC, DC, or a combination of AC and DC (i.e. HμG). The increased penetration of DC DGs and DC loads has promoted the consideration of the AC-DC hybrid configuration as a likely compromised

solution to gain the benefits of both AC and DC power. However, the AC-DC hybrid single layer paradigm still needs interfacing converters to integrate different types (AC/DC) of loads and DGs, besides the ICs that are used to transfer the power between the AC and DC buses. The elimination of these interfacing converters is one of the main benefits provided by the bilayer configuration compared to the hybrid configuration, because of the following reasons: 1) the AC-DC converters are currently more expensive compared to cost of the lines, 2) the lifetimes of the AC-DC converters are shorter than lines and buses, 3) the operation and control of the AC-DC converters are relatively complex, and 4) the converters are power-consuming devices even if no loads are connected to them. As such, the elimination of the interfacing converters would reduce the system costs and losses. The advantages of the proposed bilayer configuration can be summarized as follows:

1. Simplifying the system operation due to the reduction of the number of converters.
2. Increasing the system efficiency and decreasing the operation cost due to the reduction in the power conversion requirements.
3. Enabling the adaptation of new technologies regardless of their types (AC/DC) due to the existence of both layers (AC/DC).
4. Accommodating the high DC DGs and loads penetration.
5. Facilitating the connection to other μGs regardless of their types (AC, DC, or Hybrid).
6. Utilizing the existing AC assets in the case of system reinforcement/upgrade. In the bilayer configuration, the existing AC layer (assets) are reinforced with another DC layer in the areas of need based on the system requirements.

3.3 Power Flow Equations of the AC-DC Bilayer Microgrid

This section introduces the power flow equations in the BμG for the following three possible cases.

3.3.1 Connection of AC Buses in the AC layer

In this case, each AC bus may include AC DGs or/and AC loads and the AC lines are used to connect the AC buses, as shown in Fig. 3.1. The active and reactive power flow constraints are given by

$$P^{ac}_{G_n} - P^{ac}_{L_n} = \sum_{\substack{m \in N^{ac}_b \\ m \neq n}} K^{ac}_{nm}\ P^{ac}_{nm} \quad , \quad \forall\ n \in N^{ac}_b \tag{3.1}$$

$$Q^{ac}_{G_n} - Q^{ac}_{L_n} = \sum_{\substack{m \in N^{ac}_b \\ m \neq n}} K^{ac}_{nm}\ Q^{ac}_{nm} \quad , \quad \forall\ n \in N^{ac}_b \tag{3.2}$$

where K^{ac}_{nm} is equal to 1 if an AC line connecting buses n and m, and equal to zero otherwise; $P^{ac}_{G_n}$ and $Q^{ac}_{G_n}$ are the active and reactive power of an AC energy resource connected at bus n, respectively; $P^{ac}_{L_n}$ and $Q^{ac}_{L_n}$ are the active and reactive power demand for an AC load connected at bus n, respectively; P^{ac}_{nm} and Q^{ac}_{nm} are the active and reactive power transmitted through the AC line nm, respectively; and N^{ac}_b is the set of AC buses. The equations for P^{ac}_{nm} and Q^{ac}_{nm} are expressed as follows:

$$P^{ac}_{nm} = (V^{ac}_n)^2\, G^{ac}_{nm} - V^{ac}_n V^{ac}_m \Big(G^{ac}_{nm} \cos\theta_{nm} + B^{ac}_{nm} \sin\theta_{nm} \Big) \tag{3.3}$$

$$Q^{ac}_{nm} = -(V^{ac}_n)^2\, B^{ac}_{nm} - V^{ac}_n V^{ac}_m \Big(G^{ac}_{nm} \sin\theta_{nm} - B^{ac}_{nm} \cos\theta_{nm} \Big) \tag{3.4}$$

3.3.2 Connection of DC Buses in the DC layer

In this case, a DC line is connecting two DC buses in the DC layer, as shown in Fig. 3.2. Thus, each bus may include DC DGs or/and DC loads. The DC power flow constraint is expressed as follows:

$$P^{dc}_{G_x} - P^{dc}_{L_x} = \sum_{\substack{y \in N^{dc}_b \\ y \neq x}} K^{dc}_{xy}\ P^{dc}_{xy} \quad , \quad \forall\ x \in N^{dc}_b \tag{3.5}$$

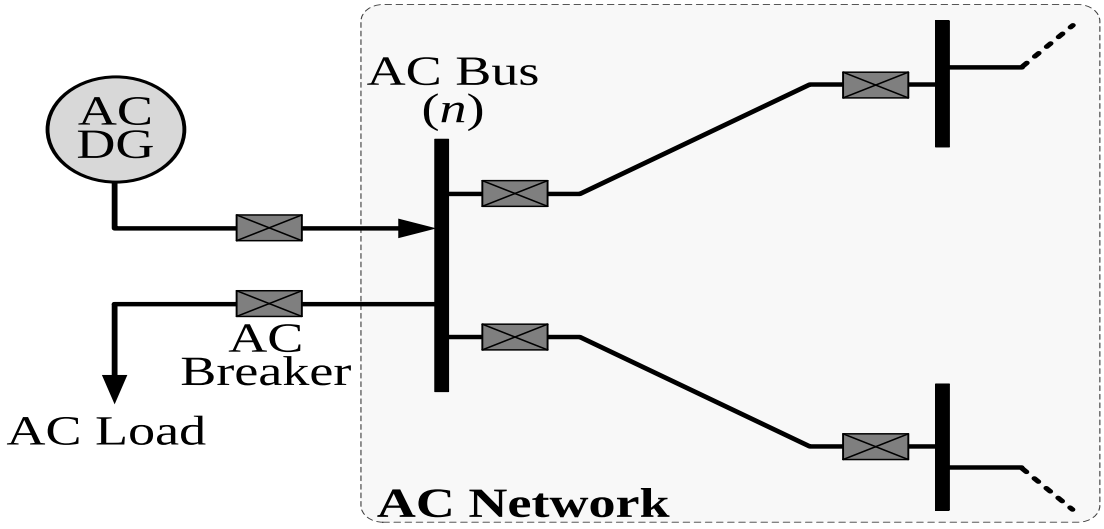

Figure 3.1: AC lines connecting the AC buses in the AC layer.

where

$$P_{xy}^{dc} = G_{xy}^{dc} \left((V_x^{dc})^2 - V_x^{dc} V_y^{dc} \right) \tag{3.6}$$

K_{xy}^{dc} is equal to 1 if a DC line connecting buses x and y, and equal to zero otherwise; $P_{G_x}^{dc}$ is the output power of a DC energy resource connected at bus x; $P_{L_x}^{dc}$ is the power demand for a DC load connected at bus x; P_{xy}^{dc} is the DC power transmitted through the DC line xy; V_x^{dc} is the voltage magnitude at DC bus x; G_{xy}^{dc} is the conductance of the DC line connecting buses x and y; and N_b^{dc} is the set of DC buses.

3.3.3 Interconnection of AC and DC Buses

In this case, an IC is connecting the AC and DC buses, as shown in Fig. 3.3. The power flow equations at the AC and DC buses that were given in (3.1), (3.2), and (3.5) are modified to include the effect of the IC, as follows:

$$P_{G_n}^{ac} - P_{L_n}^{ac} = \sum_{\substack{m \in N_b^{ac} \\ m \neq n}} K_{nm}^{ac} \, P_{nm}^{ac} + H_{nx,x=n}^{C} \, P_{nx,x=n}^{c\text{-}ac} \tag{3.7}$$

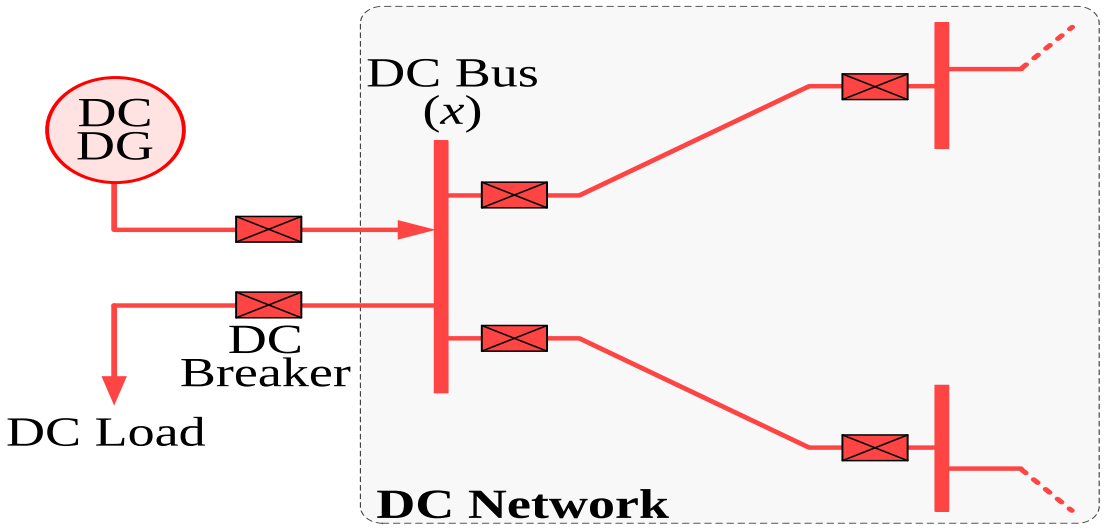

Figure 3.2: DC lines connecting the DC buses in the DC layer.

$$Q^{ac}_{G_n} - Q^{ac}_{L_n} = \sum_{\substack{m \in N^{ac}_b \\ m \neq n}} K^{ac}_{nm}\, Q^{ac}_{nm} + H^{C}_{nx,x=n}\, Q^{c\text{-}ac}_{nx,x=n} \tag{3.8}$$

$$P^{dc}_{G_x} - P^{dc}_{L_x} = \sum_{\substack{y \in N^{dc}_b \\ y \neq x}} K^{dc}_{xy}\, P^{dc}_{xy} + H^{C}_{xn,n=x}\, P^{c\text{-}dc}_{xn,n=x} \tag{3.9}$$

where

$$P^{c\text{-}ac}_{nx,x=n} = -P^{c\text{-}dc}_{xn,n=x} + P^{c\text{-}loss}_{nx,x=n} \tag{3.10}$$

$$P^{c\text{-}loss}_{nx,x=n} = \beta_{conv}\, |P^{c\text{-}ac}_{nx,x=n}| \tag{3.11}$$

$$V^{ac}_{n} = M_{nx,x=n}\, V^{dc}_{x} \tag{3.12}$$

H^{C}_{nx} is equal to 1 if an interlinking converter (IC) is connected between AC bus n and DC bus x; $P^{c\text{-}ac}_{nx}$ and $Q^{c\text{-}ac}_{nx}$ are the respective active and reactive power at the AC side of the IC; $P^{c\text{-}dc}_{xn}$ is the DC power at the DC side of the IC; $P^{c\text{-}loss}_{nx}$ is the power losses of the IC; β_{conv} is the power-loss coefficient for the ICs; and M_{nx} is the modulation index of the IC.

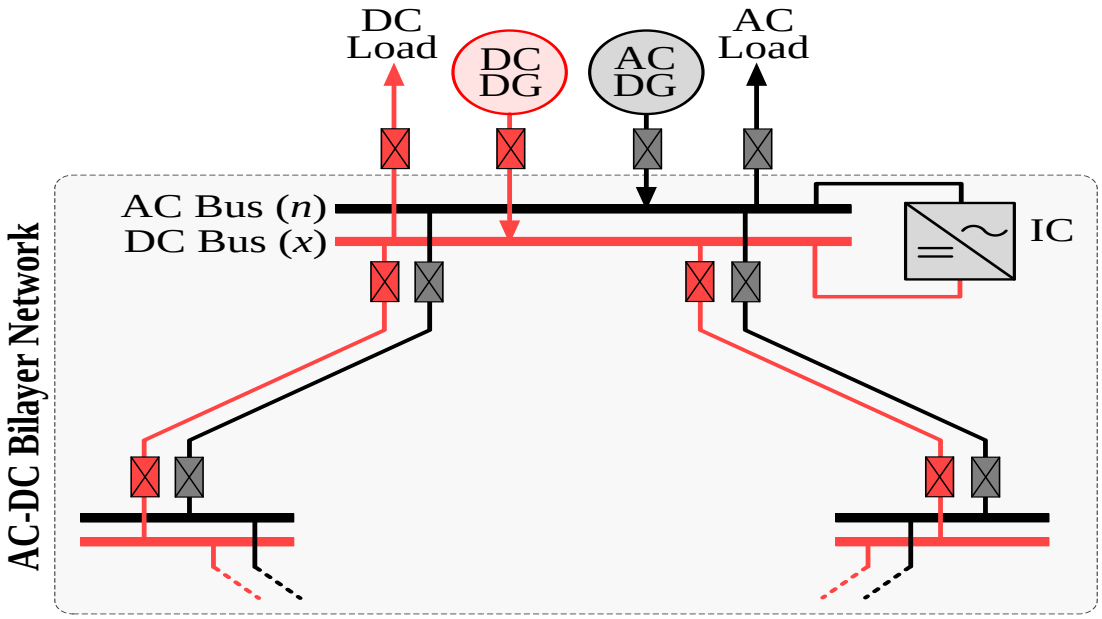

Figure 3.3: Interconnection of AC and DC layers in the BμG.

3.4 Planning Framework

The planning problem is divided into two nested optimization problems: primary and secondary. Genetic algorithm (GA) is implemented to solve the primary optimization problem, while the secondary optimization problem is implemented in the general algebraic modeling system (GAMS). The integration between the primary and the secondary problems has been carried out using the GDX utility (i.e., GDXMRW data exchange) that allows for the interface between MATLAB and GAMS [86]. The algorithms were executed on a desktop computer with the following specifications: Intel core i7 2600 @ 3.4 GHz, 64 bit, and 8 GB RAM.

The stochastic variations associated with load demands and renewable DGs are addressed in the proposed framework using an Monte-Carlo simulation (MCS) technique. As explained earlier, the possible lines combinations are: 1) an AC line connecting two AC buses in the AC layer, 2) a DC line connecting two DC buses in the DC layer, or 3) An IC connecting an AC bus in the AC layer with a DC bus in the DC layer. Therefore, the network configuration can be described by three matrices K^{ac}, K^{dc}, and H^{C}. The two

matrices K^{ac} and K^{dc} are $N \times N$ matrix that consists of $\big(0.5\,N\,(N-1)\big)$ binary variables, while H^C is a binary vector that consists of N binary variables, where N is the number of system zones.

3.4.1 Primary Optimization Problem

The primary optimization problem is performed using GA in order to find the optimal configuration that minimizes the net present value of the total system costs.

A. Objective Function

The objective function is to minimize the net present value of cost (C_{NPV}), as follows:

$$\min\ C_{NPV} = \left(C_{INV} + C_{REP} + \sum_{t=1}^{T_P} \frac{C_{AOM,t}}{(1+IR^{'})^t} \right) \tag{3.13}$$

where C_{NPV} is the net present value of the system costs (i.e., investment, maintenance, and operation costs); C_{INV} is the total investment costs; C_{REP} is the total replacement costs of the system components; T_P is the number of years in the planning study; $C_{AOM,t}$ is the annual operation and maintenance costs at year t; and $IR^{'}$ is the modified interest rate that can be calculated in terms of the interest rate (IR) and the inflation rate (FR) as follows:

$$IR^{'} = \frac{IR - FR}{1 + FR} \tag{3.14}$$

The equations for C_{INV}, C_{REP}, and $C_{AOM,t}$ are given by

$$\begin{aligned} C_{INV} = & \sum_{n \in N_b^{ac}} \sum_{\substack{m \in N_b^{ac} \\ m>n}} K_{nm}^{ac} \big(C_l^{ac}\, L_{nm} + 2\, C_{cb,nm}^{ac} \big) + \sum_{x \in N_b^{dc}} \sum_{\substack{y \in N_b^{dc} \\ y>x}} K_{xy}^{dc} \big(C_l^{dc}\, L_{xy} + 2\, C_{cb,xy}^{dc} \big) \\ & + \sum_{n \in N_b^{ac}} C_{cb,L_n}^{ac} + \sum_{x \in N_b^{dc}} C_{cb,L_x}^{dc} + \sum_{i \in N_G^{ac}} C_{cb,G_i}^{ac} + \sum_{j \in N_G^{dc}} C_{cb,G_j}^{dc} \\ & + \sum_{n \in N_b^{ac}} \sum_{\substack{x \in N_b^{dc} \\ x=n}} H_{nx}^{C} \big(C_{conv}\, S_{nx}^{\text{c-max}} + C_{cb,\text{c-}nx}^{ac} + C_{cb,\text{c-}nx}^{dc} \big) \end{aligned} \tag{3.15}$$

$$C_{REP} = \sum_{r \in N_{comp}} \frac{C_r^{rep}}{(1+IR')^{T_r}} \quad , \ \forall\ T_r < T_P \tag{3.16}$$

$$C_{AOM,t} = 8760\ \ \mathbb{E}(C_{OPF,s,t}) + \lambda_{AM}\ \ C_{INV} \tag{3.17}$$

where $C_l^{ac/dc}$ is the cost (in \$/mile) of the AC/DC lines; L_{nm} and L_{xy} are the distances (in miles) of AC line nm and DC line xy, respectively; $C_{cb,u}^{ac/dc}$ is the cost of AC/DC breaker for component u, which can be AC line (nm), DC line (xy), AC DG (G_i), DC DG (G_j), AC load (L_n), or DC load (L_x); C_{conv} is the IC cost (in \$/kVA); $S_{nx}^{c\text{-}max}$ is the rated apparent power of the IC connecting AC bus n and DC bus x; $C_{cb,c\text{-}nx}^{ac/dc}$ is the cost of the breaker at the AC/DC side of the IC connecting AC bus n and DC bus x; C_r^{rep} is the replacement cost of component r; T_r is the lifetime of component r; $C_{OPF,s,t}$ is the optimal operation cost (in \$/h) for an MCS scenario s at year t; $\mathbb{E}(C_{OPF,s,t})$ is the expected value of the operation cost at year t; and λ_{AM} is the annual maintenance cost as a % of the investment cost.

It should be noted that the apparent power of the IC connecting AC bus n and DC bus x for different MCS scenarios are represented by a stochastic variable $S_{nx,s}^c$. In the proposed planning framework, the IC rated-power ($S_{nx}^{c\text{-}max}$) is selected to achieve a 95% confidence level, while the system operation cost is represented by the expected value $\mathbb{E}(C_{OPF,s})$. For each MCS scenario for each GA chromosome, the values of the stochastic variables $\left(S_{nx,s}^c \text{ and } C_{OPF,s}\right)$ are obtained from the solution of the secondary optimization problem.

B. Optimization Constraints

Three constraints are considered in the primary optimization problem: a) the integer constraints (3.18)−(3.20) that are associated with the binary variables of the configuration matrices (K^{ac}, K^{dc}, and H^C), b) the bus-connectivity constraints (3.21)−(3.22), and c) the constraint (3.23) that limits the number of ICs in the system.

$$K_{nm}^{ac} \in \{0,1\} \quad , \ \forall\ n,m \in N_b^{ac} \tag{3.18}$$

$$K_{xy}^{dc} \in \{0,1\} \quad , \ \forall\ x,y \in N_b^{dc} \tag{3.19}$$

$$H_{nx,x=n}^{C} \in \{0,1\} \quad , \ \forall\ n \in N_b^{ac},\ x \in N_b^{dc} \tag{3.20}$$

$$N_{L,n}^{min} \leq \sum_{\substack{m \in N_b^{ac} \\ m \neq n}} K_{nm}^{ac} \leq N_{L,n}^{max} \quad , \quad \forall\, n \in N_b^{ac} \tag{3.21}$$

$$N_{L,x}^{min} \leq \sum_{\substack{y \in N_b^{dc} \\ y \neq x}} K_{xy}^{dc} \leq N_{L,x}^{max} \quad , \quad \forall\, x \in N_b^{dc} \tag{3.22}$$

$$\sum_{\substack{n \in N_b^{ac} \\ x \in N_b^{dc}}} H_{nx,x=n}^{C} \leq N_c^{max} \tag{3.23}$$

where $N_{L,n}^{max/min}$ and $N_{L,x}^{max/min}$ are the maximum/minimum allowable number of lines that can be connected to an AC bus n and a DC bus x, respectively; and N_c^{max} is the maximum allowable number of ICs.

3.4.2 Secondary Optimization Problem

The secondary optimization problem is implemented in GAMS to solve the optimal power flow (OPF) problem for each MCS scenario for each GA chromosome.

A. Objective Function

The objective is to minimize the operation cost, which is the generation cost of the AC and DC DGs, as described in (3.24).

$$\min C_{OPF} = \sum_{i=1}^{N_G^{ac}} C_{G_i}^{ac}\ P_{G_i}^{ac} + \sum_{j=1}^{N_G^{dc}} C_{G_j}^{dc}\ P_{G_j}^{dc} \tag{3.24}$$

where N_G^{ac} and N_G^{dc} are the sets of AC and DC energy resources, respectively; and $C_{G_i}^{ac}$ and $C_{G_j}^{dc}$ are the generation costs (in \$/MWh) of the AC and DC energy resources, respectively.

B. Optimization Constraints

Four types of constraints are considered in this model as follows: 1) the AC and DC power flow equations (3.1)−(3.12), 2) the upper and lower limits of the voltage magnitude and

angle at each bus, in addition to the power capacity of the network lines ((3.25)−(3.29)), 3) the active and reactive power limits for the energy resources ((3.30)−(3.32)), and 4) the modulation-index and capacity limits of the AC-DC converters ((3.33)−(3.34)).

$$V_n^{ac,min} \leq V_n^{ac} \leq V_n^{ac,max} \quad , \quad \forall\ n \in N_b^{ac} \tag{3.25}$$

$$V_x^{dc,min} \leq V_x^{dc} \leq V_x^{dc,max} \quad , \quad \forall\ x \in N_b^{dc} \tag{3.26}$$

$$\theta_n^{min} \leq \theta_n \leq \theta_n^{max} \quad , \quad \forall\ n \in N_b^{ac} \tag{3.27}$$

$$\sqrt{(P_{nm}^{ac})^2 + (Q_{nm}^{ac})^2} \ \leq \ S_{nm}^{ac,max} \quad , \quad \forall\ n, m \in N_b^{ac} \tag{3.28}$$

$$P_{xy}^{dc} \ \leq \ P_{xy}^{dc,max} \quad , \quad \forall\ x, y \in N_b^{dc} \tag{3.29}$$

$$P_{G_i}^{ac,min} \ \leq \ P_{G_i}^{ac} \ \leq \ P_{G_i}^{ac,max} \quad , \quad \forall\ i \in N_G^{ac} \tag{3.30}$$

$$P_{G_j}^{dc,min} \ \leq \ P_{G_j}^{dc} \ \leq \ P_{G_j}^{dc,max} \quad , \quad \forall\ j \in N_G^{dc} \tag{3.31}$$

$$Q_{G_i}^{ac,min} \ \leq \ Q_{G_i}^{ac} \ \leq \ Q_{G_i}^{ac,max} \quad , \quad \forall\ i \in N_G^{ac} \tag{3.32}$$

$$\sqrt{(P_{nx}^{c\text{-}ac})^2 + (Q_{nx}^{c\text{-}ac})^2} \ \leq \ S_{nx}^{c\text{-}max} \quad , \ \forall\ n \in N_b^{ac},\ x \in N_b^{dc},\ n = x \tag{3.33}$$

$$M_{nx}^{min} \leq M_{nx} \leq M_{nx}^{max} \ , \ \forall\ n \in N_b^{ac},\ x \in N_b^{dc},\ n = x \tag{3.34}$$

where $S_{nm}^{ac,max}$ is the maximum apparent power capacity of AC line nm; $P_{xy}^{dc,max}$ is the maximum power capacity of DC line xy; $P_{G_i}^{ac}$ and $Q_{G_i}^{ac}$ are the respective active and reactive power of AC resource i; $P_{G_j}^{dc}$ is the output power of DC resource j; S_{nx}^{c} and M_{nx} are the apparent-power and the modulation-index of the IC connected between AC bus n and DC bus x, respectively.

3.5 Strategy of the BμG Planning

The proposed planning framework aims to minimize the total system cost, which is achieved through the integration of two optimization models as described earlier. The stochastic variations of the loads and renewable-based DGs are inputted to the planning framework. The GAMS subroutine is running for every GA chromosome for every MCS scenario until a GA convergence is obtained. The outputs of the framework include three matrices (K^{ac}, K^{dc}, and H^{C}) that describe the AC-layer connection, the DC-layer connection, as well as

the number and locations of the ICs. It is worthwhile to note that the configurations of the AC and DC layers can be different in terms of the lines and buses.

3.5.1 Planning Framework Illustration

A GA population consisting of number of chromosomes is initialized where each chromosome represents a possible scenario of the BμG configuration, based on the three matrices (K^{ac}, K^{dc}, and H^{C}), as shown in Fig. 3.4. For each chromosome in the current GA generation, an MCS scenario is selected, and GAMS is called to solve the OPF problem to compute the operation cost and returns the model status to the GA. The solution of the OPF model can be: 1) feasible solution: the optimal operation cost ($C_{OPF,s}$) is calculated or 2) infeasible solution: a very large value is assigned to the system cost. Afterwards, if the MCS stopping criteria is not satisfied (i.e. the maximum number of iterations is not reached), then another MCS scenario is selected and the previous steps are repeated. However, if the MCS stopping criteria is satisfied and more than 95 % of the scenarios are feasible, the operation cost of this chromosome is represented by the expected value $\mathbb{E}(C_{OPF,s})$, while the corresponding chromosome is rejected if a confidence level less than 95 % is achieved. After solving all the current generation chromosomes, the GA stopping criterion is checked. If the GA stopping criterion is not satisfied, then the GA generation is updated by applying the GA operations (reproduction, crossover, and mutation) and the whole process is repeated. After the GA process is terminated, the optimal BμG configuration is obtained with the corresponding costs (for investment, maintenance and operation). The planning framework is illustrated using the pseudo code in Fig. 3.5.

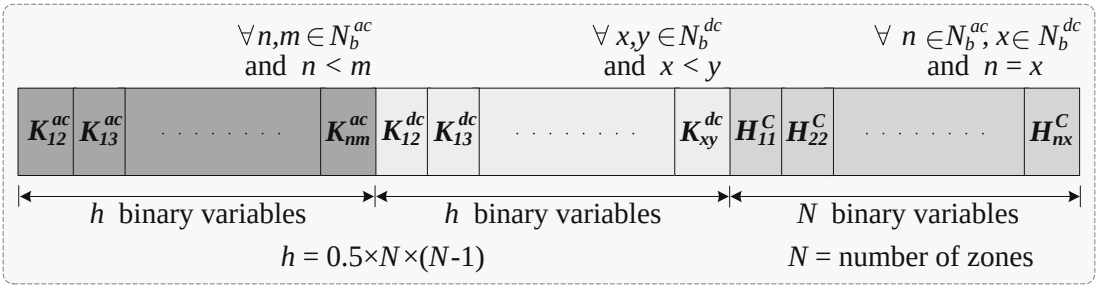

Figure 3.4: GA chromosome Structure.

Algorithm 1 – BμG Planning

```
1:  Input the data given for the system loads, energy resources, power
    flow limits, and network-configuration constraints
2:  Generate the MCS scenarios
3:  Initialize a GA population of chromosomes
4:  For GA stopping criteria not satisfied then
5:    For each chromosome in the current GA generation then
6:      For MCS stopping criteria not satisfied then
7:        Select an MCS scenario
8:        Call GAMS to solve the OPF problem and to determine
          the optimal operation cost
9:        If feasible solution for corresponding MCS scenario then
10:         calculate operation cost
11:       Else
12:         assign large value to the cost
13:       End if
14:     End for
15:     If confidence level achieved then
16:       operation cost of the current chromosome
                              = average cost (feasible solutions)
17:     Else
18:       the corresponding configuration is rejected
19:     End if
20:   End for
21:   Evaluate the GA objective function and constraints for the
      current GA generation
22:   If GA stopping criteria not satisfied then
23:     Apply GA operators to update the GA generation
24:   End if
25: End For
26: Output the B$\mu$G optimal configuration and the corresponding cost
27: End
```

Figure 3.5: Pseudo code for the proposed BμG planning framework.

3.5.2 Modeling of the Stochastic Variations

Tne stochastic variables including the AC/DC load demands, wind DGs output power, PV DGs output power, and the EVSs demand are discussed in this subsection.

I. AC and DC Load Demands

In order to incorporate the demand annual variation, year was divided into four seasons, and a typical day was used to represent each season. The load profile of a representative day for each season is shown in Fig. 3.6, based on the data provided in [87]. The hourly demand of each representative is given as a % of the annual peak demand. Then, the CDF was derived from those four daily profiles.

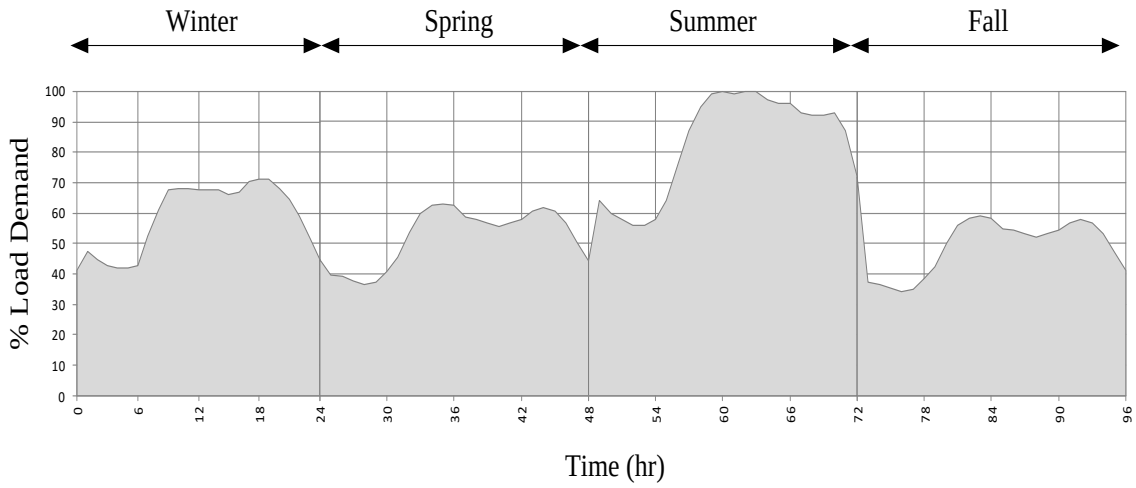

Figure 3.6: AC and DC loads Variations: typical day demand for four seasons.

II. Wind DG Output Power

The wind DGs output power were modeled based on he seasonal data provided in [87], as shown in Fig. 3.7. The hourly power generated during a typical day for each of the four seasons is given as a % of the annual maximum wind DG output power. Then, the CDF was derived from those four daily profiles.

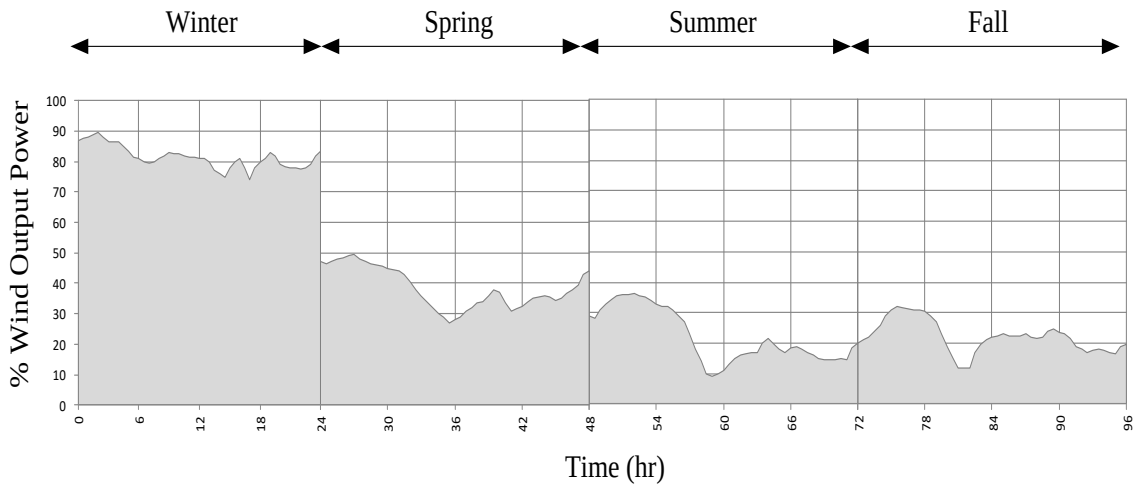

Figure 3.7: Wind DG output power variations: typical day power generation for four seasons.

III. PV DG Output Power

Fig. 3.8 shows the seasonal hourly variations in the PV output power, based on the historical data for three successive years provided in [88]. The hourly power generated during a typical day for each of the four seasons is given as a % of the annual maximum PV DG output power. Then, the CDF was derived from those four daily profiles.

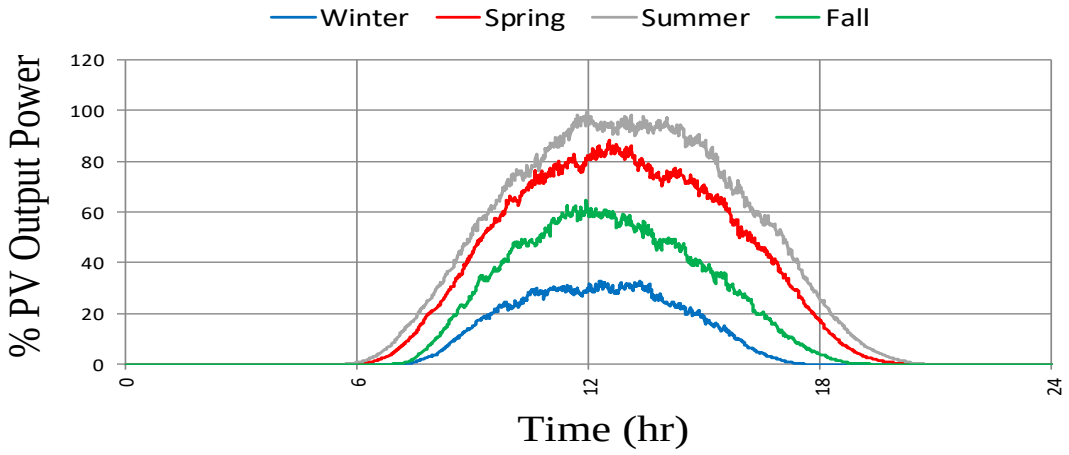

Figure 3.8: PV output power variations: typical day power generation for four seasons.

IV. EV Charging Station Demand

The hourly load variation for an EV charging station for a typical day is illustrated in Fig. 3.9, based on the 15-pole station model described in [89]. The hourly load demand of this typical day is given as a % of the peak demand of the station, which was used to derive the CDF.

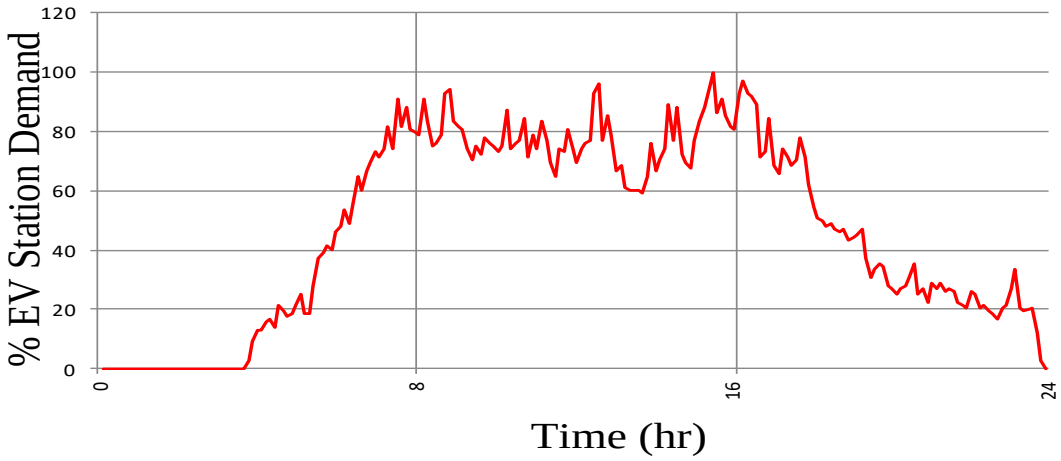

Figure 3.9: EV demand variation: typical day demand.

Best Fitting Distributions for the Stochastic Models

The stochastic variations of the PV DGs, wind DGs, and EVSs were representaed by Johnson SB distribution, as expressed in (3.35) [90].

$$F_1(x) = \Phi\left(\gamma + \delta \ln\left(\frac{z}{1-z}\right)\right) \tag{3.35}$$

where $F_1(x)$ is the cumulative distribution function (CDF) of the Johnson SB distribution; $z = \frac{x-\zeta}{\alpha}$; δ, γ are shape parameters; ζ is a location parameter; α is a scale parameter; and $\Phi(\blacklozenge)$ is the Laplace integral (i.e., the CDF of the standard normal distribution), which is given by

$$\Phi(x) = \frac{1}{\sqrt{2\pi}} \int_0^x e^{-0.5\,t^2}\,dt \tag{3.36}$$

The stochastic variations in the AC and DC load demands were represented based on the generalized Pareto distribution, expressed as (3.37) [90].

$$F_2(x) = 1 - \left(1 + k\frac{(x-\psi)}{\sigma}\right)^{-\frac{1}{k}} \quad , \quad k \neq 0 \tag{3.37}$$

where $F_2(x)$ is the CDF of the generalized Pareto distribution, k is a shape parameter, ψ is a location parameter, and σ is a scale parameter. The CDF parameters for the stochastic variables are shown in Table 3.1. For each stochastic variable, the parameters listed in Table 3.1 provide the stochastic variations of the variable as a percentage of its annual maximum value.

Table 3.1: CDF Parameters for the Stochastic Variables

Stochastic Variables	Seasons	CDF Parameters
PV-DG Power	Winter	γ= 0.6561, δ= 0.1853, α= 30.5430, ζ= -0.4102
	Spring	γ= 0.4549, δ= 0.2182, α= 81.8414, ζ= -1.3103
	Summer	γ= 0.4199, δ= 0.2332, α= 96.1342, ζ= -1.6687
	Fall	γ= 0.6052, δ= 0.2301, α= 59.0836, ζ= -1.0902
Wind-DG Power	Winter	γ= 1.4584, δ= 1.6624, α= 32.9295, ζ= 80.6751
	Spring	γ= 0.1402, δ= 0.6340, α= 25.9017, ζ= 30.9977
	Summer	γ= 0.3993, δ= 0.3682, α= 28.1423, ζ= 13.8442
	Fall	γ= 0.7441, δ= 1.6674, α= 43.7649, ζ= 7.0870
EVS	All	γ= -0.1555, δ= 0.4199, α= 94.1582, ζ= -4.1414
Load Demand	Winter	k= -2.0498, σ= 76.5706, ψ= 33.8229
	Spring	k= -2.0299, σ= 64.7435, ψ= 30.9216
	Summer	k= -2.1535, σ= 123.2435, ψ= 43.8349
	Fall	k= -2.0299, σ= 60.6328, ψ= 28.9583

3.6 Case Studies

A multi-zone microgrid is considered in these case studies, where each zone can have various types (AC/DC) of loads and DGs. A bus will be used to represent each zone, which can be AC, DC or both. Moreover, the lines connecting the buses have the possibility to be AC, DC or both. Therefore, four possible μG configurations exist:

1. AC μG: All the buses and lines are AC.
2. DC μG: All the buses and lines are DC.
3. HμG: The buses and lines can be AC or DC.
4. BμG: Two parallel layers are implemented; one is an AC layer to interface the various AC DGs and loads, while the other is a DC layer to interface the various DC DGs and loads.

The purpose is to investigate the different μG configurations (i.e. AC, DC, HμG, and BμG) to determine the optimal configuration minimizing the total system cost. The proposed planning framework is validated on the test system presented in [45]. As such, the financial parameters and system costs (i.e., lines, breakers, and converters) assumed in [45] were used in these case studies to provide a fair comparison. However, changing these values might considerably change the results. However, changing these values might affect the planning decisions and the resultant configurations. Two planning scenarios were investigated:

1. Case A: The 13 unshaded zones shown in Fig. 3.10 are considered, and the objective is to determine the optimal configuration.
2. Case B: Three extension zones represented by the shaded regions in Fig. 3.10 are assumed to be added to the existing configuration presented in Case A.
3. Small-Scale μGs: This section investigates the operation of small-scale μGs in bilayer and AC-DC hybrid μGs.

The proposed framework utilizes the MCS method and the stochastic models presented in [45], in which the seasonal stochastic variations associated with renewable-based DGs, load demands, and electric vehicles (EVs) demands were modeled based on the data given in [87–89].

Moreover, the energy costs of the PV panels, wind DGs, diesel DGs, and fuel cells are given as 209 $/MWh, 128 $/MWh, 92.2 $/MWh, and 180 $/MWh, respectively [45,91]. The active and reactive power limits of the system energy resources, in addition to the peak load demands are given in Table 3.2, while the GA parameters are given in Table 3.3. The cost of the AC-DC converters, lines, and circuit breakers are given as 170.0 $/kVA [92], 28.0 k$/mile/conductor [93], and 26.0 k$/unit [94] , respectively. The permissible limits for voltage magnitudes, voltage angles, and modulation indices are given as 0.95 to 1.05

Table 3.2: Data for the System Loads and Energy Resources

	Load Demands			**Energy Resources**				
Zone No.	P_L^{ac} (MW)	Q_L^{ac} (MVAR)	P_L^{dc} (MW)	Type	P_G^{max} (MW)	P_G^{min} (MW)	Q_G^{max} (MVAr)	Q_G^{min} (MVAr)
1	–	–	–	AC	10.0	1.0	4.8	0.8
2	1.00	0.45	–	–	–	–	–	–
3	–	–	1.25	–	–	–	–	–
4	0.50	0.25	–	DC	1.5	–	–	–
5	0.50	0.25	0.50	–	–	–	–	–
6	0.75	0.35	0.75	–	–	–	–	–
7	0.50	0.25	–	DC	1.5	–	–	–
8	0.50	0.25	1.25	–	–	–	–	–
9	–	–	0.85	AC	1.0	–	–	–
10	0.50	0.25	0.50	–	–	–	–	–
11	–	–	–	DC	1.5	–	–	–
12	–	–	1.25	–	–	–	–	–
13	0.75	0.35	–	AC	2.0	0.2	0.96	0.1
14	–	–	–	DC	1.5	0.2	–	–
15	0.75	0.35	1.25	–	–	–	–	–
16	0.50	0.25	–	AC	1.0	–	–	–

p.u., $-\pi/4$ to $\pi/4$ rad, and 0.77 to 1.0, respectively. The AC-DC interfacing converters efficiency is assumed to be 95 %, while the power-loss coefficient for the ICs is given as 5 %. The interest rate and the inflation rate are given as 7.5 % [45] and 1.0 % [95], respectively. The number of MCS scenarios is given as 10,000 [45]. $S_{base} = 10\,\text{MVA}$, $V_{base}^{ac} = 4.16\,\text{kV}$, and $V_{base}^{dc} = 6.8\,\text{kV}$ are used as base values in this study. For the AC and DC network lines, AWG #4/0 aluminum conductor steel-reinforced (ACSR) cables were used, whose DC resistance and AC impedance are (0.4415 Ω/mile) and ($0.4435 + \text{j}0.726$ Ω/mile), respectively.

Table 3.3: GA Parameters

Parameter	Value
Population size	150
Maximum number of generations	200
Stall generation limit	25
Selection criterion	Roulette wheel
Crossover criterion	Scattered
Mutation function	Gaussian

3.6.1 Case A

Case A considers 13 unshaded zones shown in Fig. 3.10, and the objective is to determine the optimal configuration. For this case, the distances between the system zones are given as follows:

1. the horizontal distance between each two adjacent zones (e.g., zones 2 and 3) is 1.4 mile
2. the vertical distance between each two successive zones (e.g., zones 1 and 5) is 1.4 mile
3. the diagonal distance between each two adjacent zones (e.g., zones 1 and 2) is 1.0 mile

In this case, four planning models were used to solve the 13-bus μG under study. The first planning model employs a traditional AC planning where all the buses and lines are assumed to be AC. In the AC planning, all the AC DGs and loads are connected directly to the AC buses, while the DC DGs and loads are connected to the AC buses via interfacing converters.

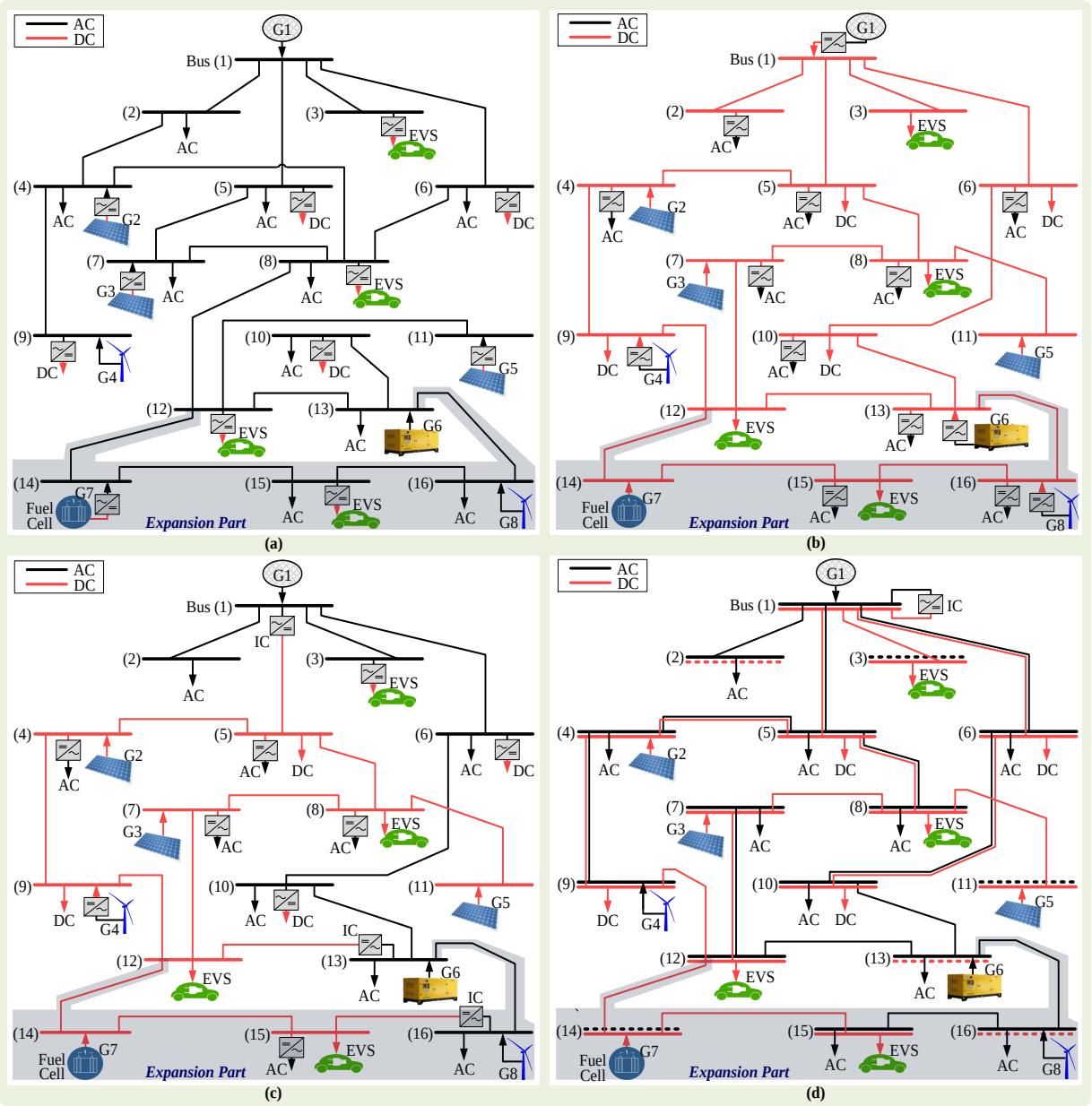

Figure 3.10: Possible solutions: (a) AC solution; (b) DC solution; (c) AC-DC hybrid solution; and (d) AC-DC bilayer solution.

Consequently, the planning model searches only for the optimal configuration of the AC network. The second planning model employs a DC planning, in which all the buses and lines are assumed to be DC, so the model searches only for the optimal configuration of the DC network. The third planning model uses the AC-DC hybrid planning technique presented in [45], in which each zone is represented by a single bus that can be AC or DC. In this technique, the network configuration is represented by a single-layer AC-DC hybrid system with ICs installed in the network lines, in addition to the use of interfacing converters for the loads and DGs at the system buses. The last planning model employs the proposed BμG planning framework, in which the nodes and the wiring system are universal and can include two types of power (AC and DC). In this framework, the DC DGs and loads are connected directly to the DC layer, while the AC DGs and loads are connected directly to the AC layer. Thus, eliminating the need for interfacing converters. The interconnection between the DC layer and the AC layer is achieved through the installation of ICs. This planning framework searches for the optimal configuration represented by the DC-layer connection, the AC-layer connection, as well as the converter sizes and locations. The bus connectivity constraints for all AC and DC buses were selected to be $N_L^{max}=4$ and $N_L^{min}=0$, while the maximum number of ICs was chosen to be $N_c^{max}=2$.

It should be noted that in the AC planning, the elements of the matrices K^{dc} and H^C are set to zeros, and equation (3.1) is replaced by (3.38). Furthermore, in the DC planning, the elements of the matrices K^{ac} and H^C are set to zeros, and equation (3.5) is replaced by (3.39).

$$\left(P_{G_n}^{ac} - P_{L_n}^{ac} + \eta_{inv\text{-}n}\, P_{G_n}^{dc} - \eta_{rec\text{-}n}^{-1}\, P_{L_n}^{dc}\right) = \sum_{\substack{m\in N_b^{ac}\\ m\neq n}} K_{nm}^{ac}\; P_{nm}^{ac} \quad , \quad \forall\; n \in N_b^{ac} \tag{3.38}$$

$$\left(P_{G_x}^{dc} - P_{L_x}^{dc} + \eta_{rec\text{-}x}\, P_{G_x}^{ac} - \eta_{inv\text{-}x}^{-1}\, P_{L_x}^{ac}\right) = \sum_{\substack{y\in N_b^{dc}\\ y\neq x}} K_{xy}^{dc}\; P_{xy}^{dc} \quad , \quad \forall\; x \in N_b^{dc} \tag{3.39}$$

where $\eta_{inv/rec}$ is the efficiency of an interfacing inverter/rectifier, as a %.

The optimal configurations obtained from the four planning models are presented in Fig. 3.10 (a−d). It should be noted that in the BμG configuration, buses 2 and 13 are only AC due to the absence of DC DGs and DC loads at these buses, and also they are not

connected to other DC buses. By the same concept, buses 3 and 11 are only DC buses. The obtained configuration therefore shows the flexibility and effectiveness of the proposed framework in finding the optimal configuration. The system cost is crucial in the choice of the optimal configuration. For that reason, a detailed analysis is carried out to compare and investigate the cost of each configuration. The present value is determined for a 15 years study period with an annual load growth rate of 0.7 %. The costs of the four μG configurations are listed in Table 3.4.

As shown in Table 3.4, the bilayer configuration achieved the lowest total net present cost of 49.832 M$ The results revealed that the bilayer configuration has extra costs compared to AC, DC, and AC-DC hybrid configurations in terms of lines and breakers. However, the bilayer configuration has the lowest operation cost and converters cost. The converters cost is the main saving factor in the bilayer configuration as it resulted in cost savings of 46.86 %, 70.32 %, and 54.36 % compared to the AC μG, DC μG, and HμG, respectively. Hence, the hybrid configuration would be the optimal configuration for the case under study provided the reduction of the converters cost. However, this scenario is not likely to occur for the following reasons a) converters are mature technology in the industry and their price is not likely to decrease dramatically in the next decade and b) converters are introducing significant cost savings of in the bilayer configuration of 46.86 %, 70.32 %, and 54.36 % compared to the AC μG, DC μG, and HμG and reduction by these significant values is unlikely to occur.

In conclusion, the extra costs introduced by the bilayer configuration in terms of lines and breakers were compensated by the savings in operation cost and converters, which resulted in overall cost savings of 5.6 %, 6.04 %, and 2.25 % in the bilayer configuration compared to the AC μG, DC μG, and HμG, respectively. In addition to the cost savings, the bilayer facilitates the adaptation of new technologies due to the existence of both layers (AC and DC), which reduces the future costs resulting from modifications and upgrades of the system. Thus, the bilayer configuration is shown to be the optimal configuration for the case under study.

Table 3.4: Comparison of different μG Configurations

Costs (M$)	AC	DC	Hybrid	Bilayer
Operation cost at year #15	5.0004	4.9177	4.9135	4.8042
Cost of lines	1.7136	0.9290	1.2264	2.0160
Cost of converters	2.0485	3.150	1.7595	0.9350
Cost of breakers	1.5340	1.6120	1.5340	1.6640
Total operation cost for 15 years	47.494	47.343	46.462	45.217
Total net present cost	52.790	53.035	50.981	49.832

3.6.2 Case B

In contrast to Case A that involves the planning of new constructed zones, Case B involves the integration of three new zones as an extension to the existing configuration obtained from Case A. The objective is to find the optimal configuration of the new zones for the four possible μG configurations, so that the system cost is minimized. The optimal configuration of the AC μG, DC μG, HμG, and BμG are presented by the shaded regions in Fig. 3.10 (a−d), respectively.

The case study has zones with only-AC or only-DC power, and yet the proposed planning framework successfully found the optimal bilayer configuration that provides lower cost than the AC, DC, and hybrid configurations. The buses associated with these zones (e.g., buses 2, 3, 11, 13, 14 and 16) were only AC or DC without the need to include both buses. In other words, the bilayer configuration can be considered as a generalized system that adopts AC, DC, and hybrid technologies. It is capable of accommodating any type of system.

Table 3.5 shows the extension costs that include the cost of adding new lines, converters, and breakers, in addition to the replacement cost of the old converters, given that the converters average lifetime is 15 years [96]. As per Table 3.5, the BμG achieved minimum cost of adding new converters of 0.17 M$, minimumm cost of replacing old converters of 0.935 M$, and minimum cost of adding new breakers of 0.338 M$, which resulted in minimum overall investment cost of 1.779 M$ for the extension planning at year #16. In other words, the BμG achieved cost savings, in the investment costs, at year #16, of 47.579 %,

Table 3.5: Cost Comparison of different μG Configurations after Expansion

Costs (M$)	AC	DC	Hybrid	Bilayer
Operation cost at year #16	6.2505	6.4969	6.1995	6.0606
Cost of adding new lines	0.4032	0.2688	0.2968	0.3360
Cost of adding new converters	0.5525	0.7770	0.4845	0.1700
Cost of replacing the old converters	2.0485	3.150	1.7595	0.9350
Cost of adding new breakers	0.3900	0.4160	0.3640	0.3380
Total investment cost at year #16	3.3937	4.6118	2.9043	1.7790

61.425 %, and 38.745 % compared to the AC μG, DC μG, and HμG, respectively. Moreover, the BμG has the lowest operation cost of 6.0606 M$ at year #16, which introduces cost savings of 3.038 %, 6.715 %, and 2.241 %, compared to the AC μG, DC μG, and HμG, respectively.

The obtained results therefore revealed that the proposed planning framework successfully determined the optimal BμG configuration that achieved the minimum operation and investment costs.

3.6.3 Small-Scale Case Studies

This subsection is concerned with the evaluation of small-scale μGs in order to validate their effectiveness on remote communities electric networks. These networks are usually characterized by limited number of lines, buses, and converters, which fits the case study evaluated in this section. Two cases are considered in this evaluation, and the obtained AC-DC hybrid and bilayer configurations are compared together for a 15 years study period with an annual load growth rate of 0.7 %. The same economic parameters utilized in the two aforementioned case studies, that were given in Subsection 3.6.1 and Subsection 3.6.2, are implemented for these cases.

Case I

The first case includes a reduced scale of the grid given in Fig. 3.10. This smaller scale grid has 6 zones, where each zone can have various types (AC/DC) of loads and DGs, as given in Fig. 3.11. The same active and reactive power limits of the system energy resources, the peak load demands of the 6 zones, and the economic parameters and components (AC-DC converters, lines, and circuit breakers) costs utilized in the two case studies A and B, that were given in Subsection 3.6.1 and Subsection 3.6.2, are utilized in the analysis of this 6 zones case study.

The present value is determined for a 15 years study period with an annual load growth rate of 0.7 %. The costs of the HμG and BμG configurations are listed in Table 3.6. As shown in Table 3.6, the bilayer configuration achieved a lower total net present cost of 2.0551 M$, compared to the hybrid configuration whose net present cost is 2.1228 M$. The results revealed that the bilayer configuration has extra costs compared to the AC-DC hybrid configurations in terms of lines and breakers, with a total value of 1.4926 M$ which is 32.15 % costly compared to the hybrid configuration. However, the bilayer configuration has the lowest operation cost and converters cost with cost savings of 1.36 % and 63.96 % , respectively, compared to the AC-DC hybrid configuration. As a result, the BμG configuration achieved cost savings of 1.83 % compared to the HμG configuration.

Table 3.6: Cost Comparison of AC-DC Hybrid and Bilayer μG Configurations for Case I

Costs (M$)	Hybrid	Bilayer
Operation cost at year #15	2.2703	2.2395
Cost of lines	0.4928	0.8160
Cost of converters	0.9435	0.3400
Cost of breakers	0.5200	0.6766
Total net present cost	21.206	20.824

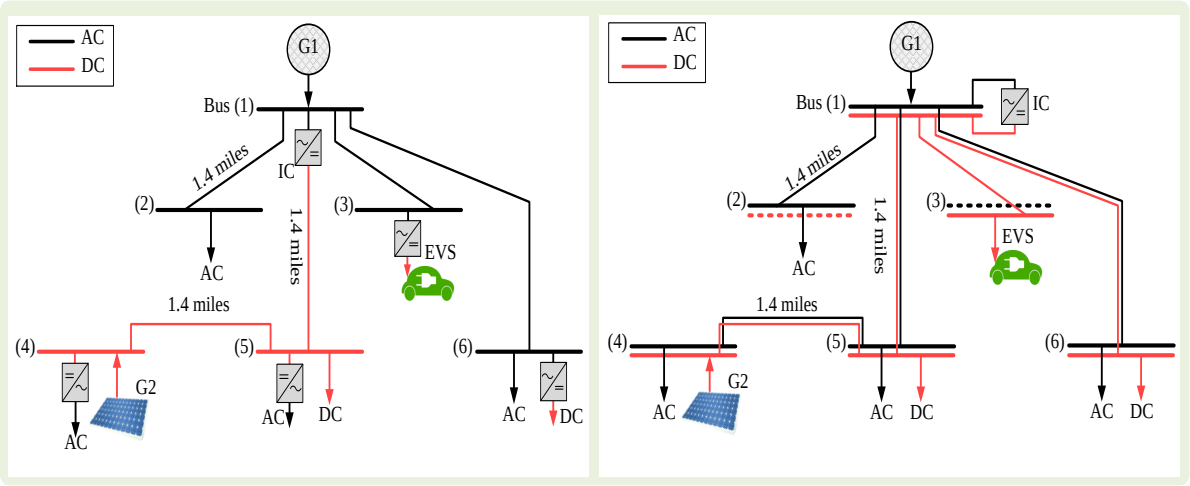

Figure 3.11: Case Study I: (6-bus microgrid).

Case II

The second case includes a four zone μG, as shown in Fig. 3.12. The distance between every two consecutive zones is 1.0 mile. The active and reactive power limits of the system energy resources, in addition to the peak load demands of the 4 zones are given in Table 3.7. While, the economic parameters and components (AC-DC converters, lines, and circuit breakers) costs utilized in the two case studies A and B, that were given in Subsection 3.6.1 and Subsection 3.6.2, are utilized in the analysis of this 6 zones case study.

Table 3.7: Data for the System Loads and Energy Resources

	Load Demands			**Energy Resources**				
Zone No.	P_L^{ac} (MW)	Q_L^{ac} (MVAR)	P_L^{dc} (MW)	Type	P_G^{max} (MW)	P_G^{min} (MW)	Q_G^{max} (MVAr)	Q_G^{min} (MVAr)
1	–	–	0.50	AC	2.0	0.3	1.0	0.15
2	0.50	0.25	0.25	–	–	–	–	–
3	0.50	0.25	–	–	–	–	–	–
4	–	–	0.25	DC	1.0	0.15	–	–

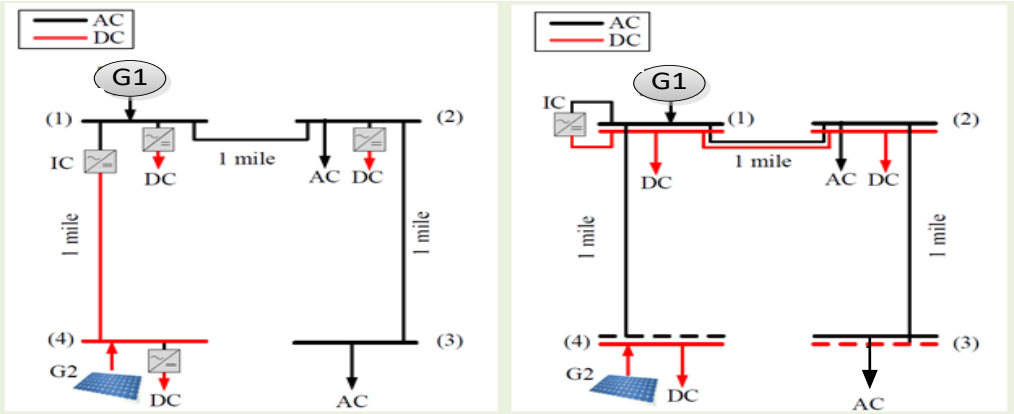

Figure 3.12: Case Study II: (4-bus microgrid).

Table 3.8: Cost Comparison of AC-DC Hybrid and Bilayer μG Configurations for Case II

Costs (M$)	Hybrid	Bilayer
Operation cost at year #15	0.957	0.943
Cost of lines	0.224	0.280
Cost of converters	0.374	0.187
Cost of breakers	0.390	0.442
Total net present cost	9.129	8.882

Similarly, the present value is determined for a 15 years study period with an annual load growth rate of 0.7 %. The costs of the HμG and BμG configurations are listed in Table 3.8. As shown in Table 3.8, the bilayer configuration achieved a lower total net present cost of 9.129 M$, compared to the hybrid configuration whose net present cost is 8.882 M$. The results revealed that the bilayer configuration has extra costs compared to the AC-DC hybrid configurations in terms of lines and breakers, with a total value of 0.722 M$ which increases the costs by 14.95 % compared to the hybrid configuration. However, the bilayer configuration has the lowest operation cost and converters cost with cost savings of 1.48 % and 100 % , respectively, compared to the AC-DC hybrid configuration. As a result, the BμG configuration achieved cost savings of 2.78 % compared to the HμG configuration.

3.7 Conclusion

A novel stochastic planning framework for BμGs has been proposed in this chapter. The BμG represents a new design for future smart systems, where each node in the BμG configuration is allowed to be a universal node that can include two buses (AC and DC) or a single bus (AC or DC), based on the types, locations, and specifications of the μG loads and DGs. In order to facilitate the connection between the system nodes, the wiring of the BμG configuration can also be universal (AC, DC, or both). The proposed framework considers the stochastic variations of the loads and renewable DGs, and it determines the optimal μG configuration described by the decision matrices K^{ac}, K^{dc}, and H^{C}. The objective of the proposed framework is to minimize the net present value of the system total costs (i.e. investment, maintenance, and operation costs). Several case studies were implemented to validate the effectiveness of the proposed planning framework. The first case study involved the determination of the optimal configuration for a new system to be constructed, while the second case study involved the extension of the μG obtained from the first case study. The third and fourth case studies involved the determination of the optimal configuration for two small-scale μGs to validate their effectivness on remote communities electric network. The results included cost comparisons of the BμG with other types of μGs (AC μG, DC μG, and HμG). The obtained results, for four case studies, demonstrated the benefits and the cost savings offered by the BμG and showed the capability of the planning framework in achieving the optimal configuration for the cases under study. The resulted revealed that converters represent the critical cost leading to cost savings in the bilayer configuration, while the lines are the dominant costs for the bilayer configuration and their reduction would introduce extra cost savings for the bilayer configuration which is achieved by the planning framework. Besides the cost savings, the bilayer facilitates the adaptation of new technologies due to the existence of both layers (AC and DC), which reduces the future costs resulting from modifications and upgrades of the system. The analysis discussed in this chapter shows that the BμG is a possible candidate that should be considered in the planning of future smart μGs.

Chapter 4

Interlinked Bilayer AC/DC Microgrids with Fault Confining Capabilities

4.1 Introduction

As mentioned in the previous chapter, the bilayer configuration has shown to be a promising candidate for future smart systems due to its numerous benefits, such as reduced system cost, adaptation of new technologies as a result of the existence of both layers (AC/DC), and full utilization for the AC assets. However, the operation of the bilayer configuration is critical due to the interconnection of the two layers (AC and DC) through the IC, and hence a fault in the AC layer would impact the DC layer resulting in service interruption for the whole network. This issue represents a main obstacle in the implementation of the bilayer configuration, which calls for further investigation and analysis for the protection techniques in order to provide innovative solution that would minimize the fault impact and service interruption in the network. For these reasons, this Chapter proposes the utilization of the modular multilevel converter (MMC) in bilayer microgrids, which would isolate the faulty layer from the healthy layer when a fault occurs, and hence reduces the impact of the fault by preventing the service interruption of the healthy layer.

This chapter is organized as follows: Section 4.2 presents a mathematical formulation for the fault current calculation in the interlinked BμGs. A solution (i.e. methodology) for the fault current alleviation in BμGs is presented in Section A.2. The simulations results are given in Section A.3. Finally, the chapter is concluded in Section 4.5.

4.2 Fault Current Calculation

This section presents the dynamic equations modeling the hybrid/bilayer microgrid during normal and fault conditions. It is crucial to consider the converter voltage to calculate the fault current contribution. The output voltage level of the converter depends on the number of SMs connected in the arms [97]. Considering the layout shown in Fig. A.1 and the module configuration presented in Fig. A.2, the dynamic behavior of the MMC is represented by the following set of equations [98]:

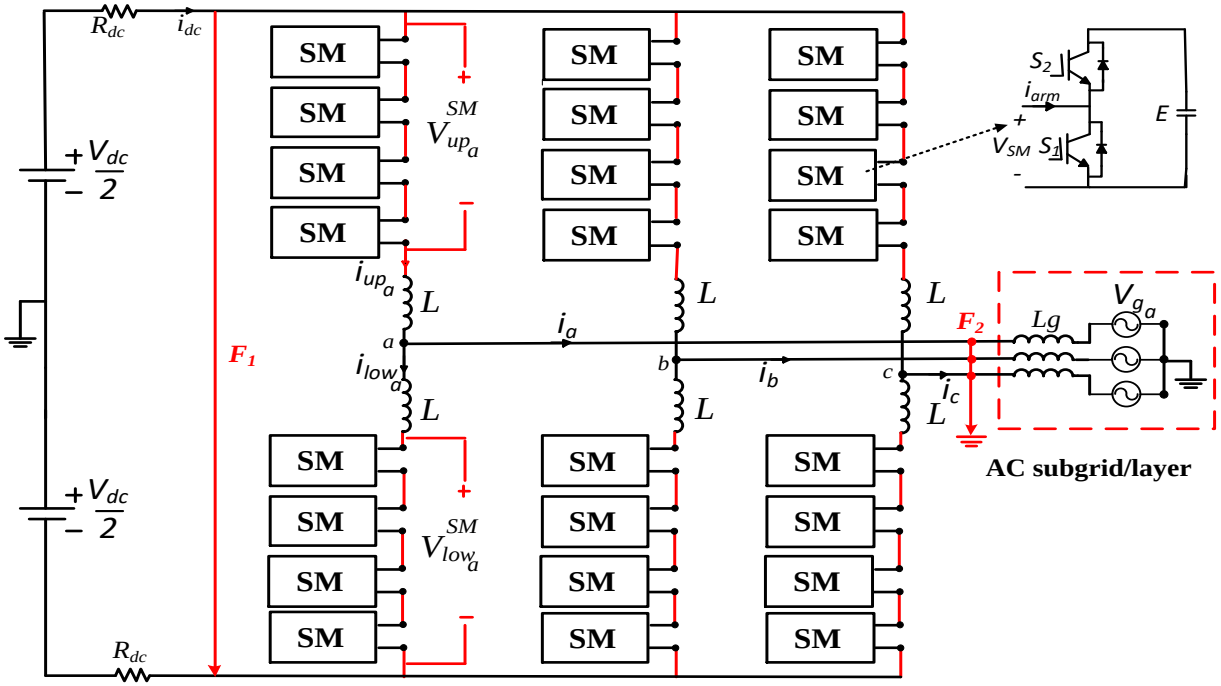

Figure 4.1: Modular Multilevel Converter Layout.

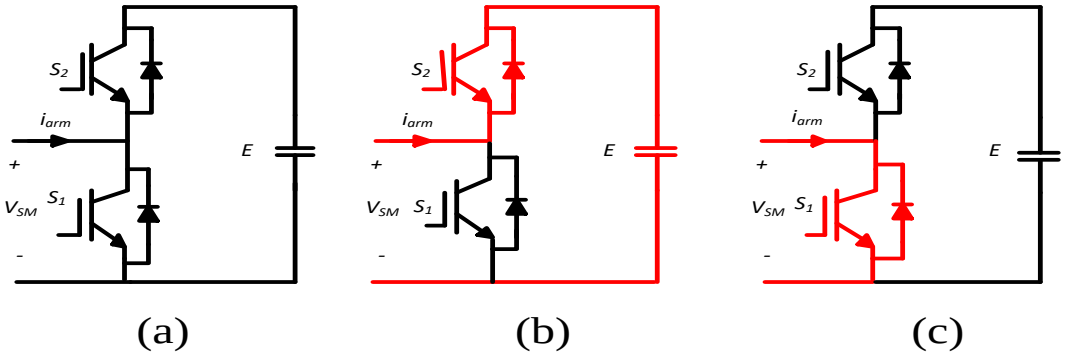

Figure 4.2: (a) Half-bridge Submodule Configuration, (b) On State, (c) Off State

$$V_{up_j} = V_{up_j}^{SM} + L\frac{di_{up_j}}{dt} \tag{4.1}$$

$$V_{low_j} = V_{low_j}^{SM} + L\frac{di_{low_j}}{dt} \tag{4.2}$$

$$V_{up_j}^{SM} = \sum_{k=1}^{n} S_{up_{j_k}} V_{c_{up_{j_k}}} \tag{4.3}$$

$$V_{low_j}^{SM} = \sum_{k=1}^{n} S_{low_{j_k}} V_{c_{low_{j_k}}} \tag{4.4}$$

$$V_j = \frac{V_{dc}}{2} - V_{up_j} = -\frac{V_{dc}}{2} + V_{low_j} \tag{4.5}$$

$$V_{up_j}^{SM} = -V_j - L\frac{di_{up_j}}{dt} + \frac{V_{dc}}{2} \tag{4.6}$$

$$V_{low_j}^{SM} = V_j - L\frac{di_{low_j}}{dt} + \frac{V_{dc}}{2} \tag{4.7}$$

$$i_{up_j} = \frac{i_j}{2} + \frac{i_{dc}}{3} \tag{4.8}$$

$$i_{low_j} = -\frac{i_j}{2} + \frac{i_{dc}}{3} \tag{4.9}$$

Where,

V_{g_j} : AC-side voltage of phase j (j = a, b, c)

V_{dc} : DC-grid voltage

I_{dc} : DC-grid current

V_j : Converter output voltage of phase j

i_j : Output current of phase j

V_{up_j} : Total voltage of upper arm of phase j

V_{low_j} : Total voltage of lower arm of phase j

$V_{up_j}^{SM}$: Total voltage of upper SMs of phase j

$V_{low_j}^{SM}$: Total voltage of lower SMs of phase j

i_{up_j} : Upper arm current of phase j

i_{low_j} : Lower arm current of phase j

$V_{C_{k_{up_j}}}$: Instantaneous voltage of submodule k of the upper arm of phase j

$V_{C_{k_{low_j}}}$: Instantaneous voltage of submodule k of the lower arm of phase j

$V_{up_{j_k}}$: Switching functions of upper arm submodule of phase j

$V_{low_{j_k}}$: Switching functions of lower arm submodule of phase j

4.2.1 DC Side Fault

In this scenario, the fault takes place on the dc side of the interlinked converter. Consequently, the contribution from the dc layer is simple to calculate. However, the contribution from the ac side is challenging because of the status of the MMC. The MMC contributes to the ac side current through the charged SM capacitors according to the switching status of each SM.

For a DC side fault, the DC-current is calculated as follows:

$$i_{dc} = \frac{Vdc}{2 * R_{dc}} \tag{4.10}$$

However, the calculation of the AC-side contribution into the DC-side fault starts with the calculation of the output phase voltage vj. This output phase voltage is added to the submodules output voltages of the same phase to calculate the voltage that appears across the arm inductance of the same phase considering zero voltage during the dc fault as presented in (4.11) and (4.12).

$$V_j \ = V_g + L_g \frac{di_j}{dt} \tag{4.11}$$

$$V_j + V_{up_j}^{SM} + L \frac{di_{up_j}}{dt} = 0 \tag{4.12}$$

From (4.8), $i_{up_j} = \frac{i_j}{2}$ during dc fault since the dc side current will circulate through the fault and the dc layer only. Consequently, (4.12) can be rewritten as follows:

$$V_j + V_{up_j}^{SM} + \frac{L}{2} \frac{di_j}{dt} = 0 \tag{4.13}$$

Equating (4.11) and (4.13) results in the following equations:

$$V_g + L_g \frac{di_j}{dt} + V_{up_j}^{SM} + \frac{L}{2} \frac{di_j}{dt} = 0 \tag{4.14}$$

$$\frac{di_j}{dt} \ = \frac{-V_g - \ \sum_{k=1}^{n} S_{up_{j_k}} V_{c_{up_{j_k}}}}{L_g + \frac{L}{2}} \tag{4.15}$$

The AC- side current in each phase during the DC-side fault can be calculated using (4.15). The negative sign indicates the direction of the current contribution from the ac layer to the fault. The arm current of phase j equals half the phase current and thus the current can be calculated as presented in (4.16).

$$i_{up_j} \ = \int \frac{1}{2} * \frac{-V_g - \ \sum_{k=1}^{n} S_{up_{j_k}} V_{c_{up_{j_k}}}}{L_g + \frac{L}{2}} \tag{4.16}$$

Therefore, the fault current in case of DC-side faults considering the contribution of both DC and AC layer to the fault is calculated as follows:

$$i_f \ = i_{dc} + i_{ac} \tag{4.17}$$

$$i_f \ = i_{dc} - (i_{up_a} + i_{up_b} + i_{up_c}) \tag{4.18}$$

Thus, the total fault current in this case is calculated using (4.18) with the DC contribution calculated using (4.10) and AC contribution calculated through applying (4.16) for each phase.

4.2.2 AC Side Fault

In this scenario, the fault occurs on the ac side of the interlinking converter. In this case, the contribution from the ac side is simple to calculate while the contribution from the dc side is the challenging component. The MMC contributes to the ac side current through the charged capacitors according to the present switching scheme.

For the system layout shown in Fig. A.1, the AC current during a fault on the AC-side is calculated using the following equations:

$$V_g + L_g \frac{di_j}{dt} = 0 \tag{4.19}$$

$$i_j \ = -\frac{1}{L_g} \int V_g dt \tag{4.20}$$

However, the calculation of the DC-side contribution to the AC-side faults is formed by applying KVL in the DC layer as follows:

$$\frac{V_{dc}}{2} - R_{dc} * i_{dc} - V_{up_j}^{SM} - L \frac{di_{up_j}}{dt} = 0 \tag{4.21}$$

From this equation, the DC-side contribution is expressed as follows:

$$i_{up_j} \ = \frac{1}{L} \int \frac{V_{dc}}{2} - R_{dc} * i_{dc} - V_{up_j}^{SM} \tag{4.22}$$

Similarly, the current in the lower arm of phase j during AC-side fault can be calculated as presented in (4.23).

$$i_{low_j} = \frac{1}{L}\int \frac{V_{dc}}{2} - R_{dc} * i_{dc} - V_{low_j}^{SM} \tag{4.23}$$

Therefore, the contributions of the DC layer to the AC layer faults through the converter phase j equals i_{f_j} as expressed in (4.24).

$$i_{f_j} = i_{up_j} - i_{low_j} \tag{4.24}$$

4.3 Fault Confining Capability

Fault confining capability is crucial to prevent any contribution from the AC layer into the DC layer and vice versa. When a fault is detected, both layers should be isolated to avoid the contribution of the fault from one of the layers to the other. Unfortunately, the conventional voltage source converter is unable to provide fault confining capability (See Appendix) when the IGBTs signals are turned off (i.e. when a fault occurs) [97, 99, 100].

Thus, replacing the conventional IC by another converter topology that has fault confining capability is essential to decouple the two layers during faults, which would allow the two layers to work independently during faults. This objective is achieved through the utilization of the switched capacitor SM (SCSM) topology [101], shown in Fig. 4.3, or any other SM topology with fault confining capability [99,100]. The SCSM topology has seven IGBTs with their antiparallel diodes, in addition to free wheeling diode (Df), thus it is capable of generating three voltage states 0, E, or 2E as illustrated in Fig. 4.4, Fig. 4.5, and Fig. 4.6, respectively.

The SCSM topology depends on its internal power semiconductor devices to provide fast response when a fault is detected. Upon the occurrence of a fault, the IGBTs gating signals are disabled. However, the current is not cut off suddenly since a current path is provided through the SM diodes as illustrated in Fig. 4.7. For $I_{arm} > 0$, D1, D2, D3 and D4 provide a path for the current and the SM terminal voltage is 2E, as shown in Fig. 4.4-a. However, the current path is through diodes D2, D5, , D6 and Df for Iarm $<$ 0 with a terminal voltage -E, as shown in Fig. 4.4-b. It is clear that the SCSM has full

blocking capability since the SM has an opposing voltage in case of negative arm current, thus forcing the diodes to be reversed biased.

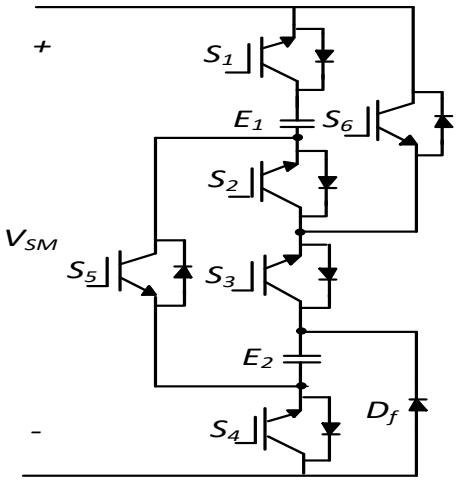

Figure 4.3: Switched Capacitor Submodule Configuration

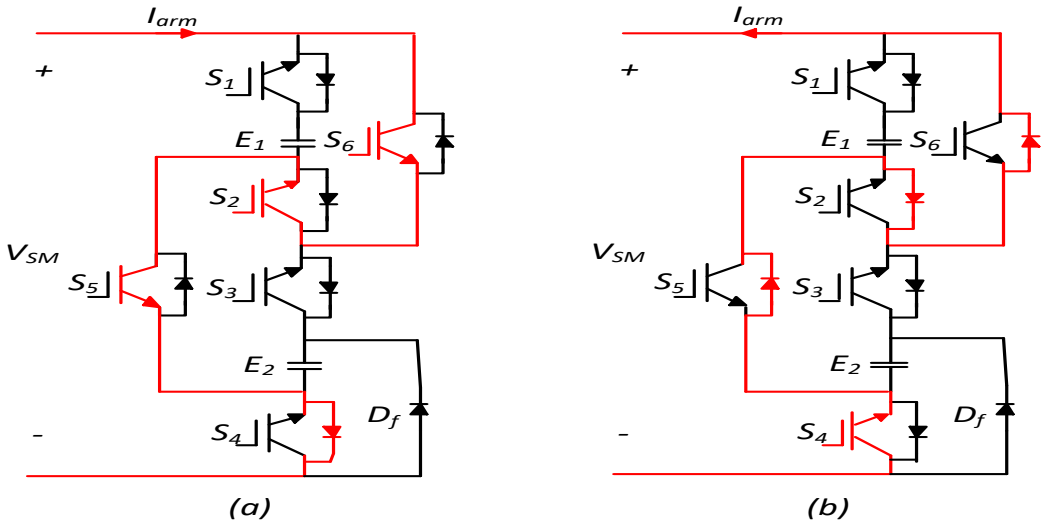

Figure 4.4: Switched Capacitor Submodule Operation: 0 State a): Positive Arm Current, b): Negative Arm Current

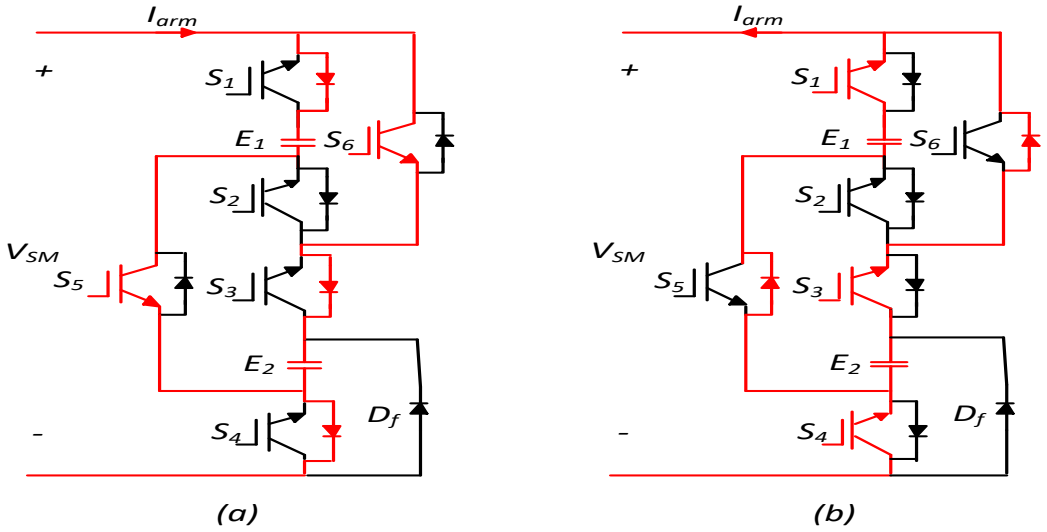

Figure 4.5: Switched Capacitor Submodule Operation: E State a): Positive Arm Current, b): Negative Arm Current

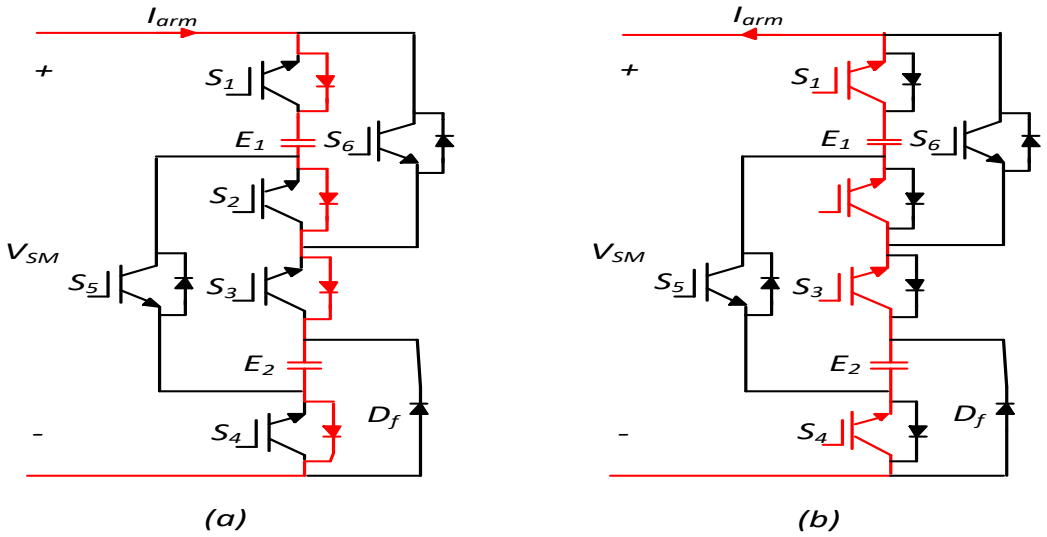

Figure 4.6: Switched Capacitor Submodule Operation: 2E State a): Positive Arm Current, b): Negative Arm Current

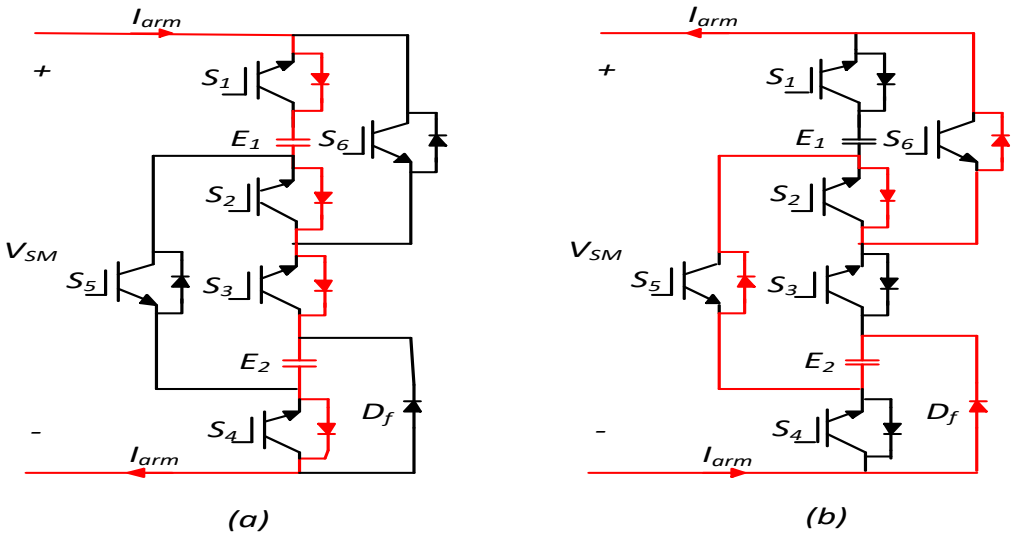

Figure 4.7: Switched Capacitor Submodule Operation During Fault Conditions (a): Positive Arm Current, (b): Negative Arm Current

The SCSM operation during normal and fault operating conditions are sumamrized in Table. 4.1.

Table 4.1: Operational Modes of Switched Capacitor Submodule

During Normal Operation	
$V_{SM} = 0$	S_2, S_5, S_4, S_6 ON
$V_{SM} = E$	S_1, S_6, S_3, S_5, S_4 ON
$V_{SM} = 2E$	S_1, S_2, S_3, S_4 ON
During Fault	
V_{SM} **for** $I_{SM} > \mathbf{0}$	2E D_1, D_2, D_3, D_4
V_{SM} **for** $I_{SM} < \mathbf{0}$	-E D_f, D_5, D_6, D_2

4.4 Simulation Results

A simulation model for microgrid layout presented in Fig. A.1 was implemented using MATLAB/SIMULINK. The system operation was tested for normal and fault operating conditions using the conventional half-bridge submodule topology. While, the system operation is evaluated during fault conditions using the SCSM topology to validate its effectiveness in confining the fault. The ac layer is modeled by a voltage source connected through impedance to the MMC terminals. On the other hand, the dc layer is represented by a dc voltage source and a resistance.

4.4.1 Fault Current Validations

In this subsection, a 9-level half-bridge SM MMC (i.e., 8 SMs) layout is used as the interlinking converter with a switching frequency of 3 kHz. The system is simulated during normal operating conditions followed by the two fault scenarios under study (i.e. DC-side and AC-side faults). For each fault scenario, the DC and AC current contributions are calculated using the mathematical equations presented in Section 4.2 and then compared with the faults currents obtained from the simulation model to verify the validity of the proposed calculation formulas.

A. DC Side Fault

A fault is initiated on the DC side at t=0.28 sec as shown in Fig. 4.8, and both the DC and AC side currents are calculated during the fault interval. Fig. 4.8.a shows the DC side current obtained from the simulation model. It is clear that the current reaches a value of 3000A after the fault initiation which is exactly equal to the theoretical dc grid current obtained from (4.10). However, the AC current contribution into the DC fault of phase A is calculated from (4.16) and plotted on Fig. 4.8.b with the AC current obtained from the simulation model. According to the figure, the calculated AC current coincide over the simulated current.

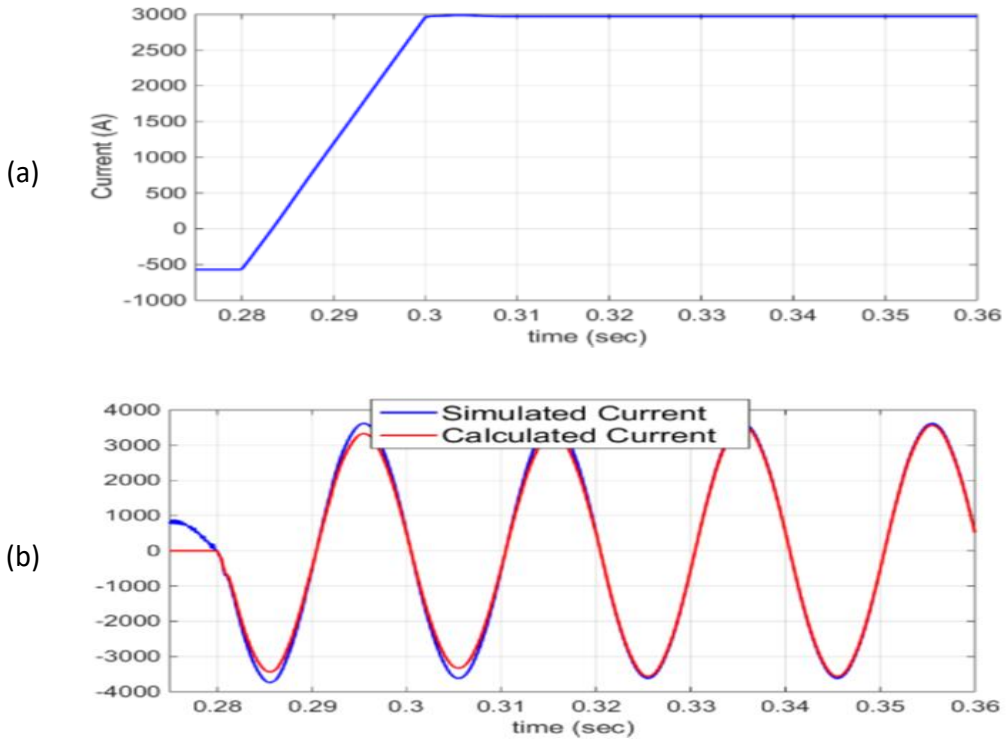

Figure 4.8: Simulations Results Under DC Fault Operating Conditions (a): DC Grid Current and (b): Simulated and Calculated AC Grid Gurrent

B. AC Side Fault

A solid three phase fault is initiated on the AC side at t=0.28 sec and both the DC and AC side currents are calculated during such a fault. Fig. 4.9.a shows the calculated AC side current of phase A from (4.20) with the AC current obtained from the simulation model. The contribution of the DC grid into the AC fault through the converter phase j (i.e. j=a) is calculated from (4.22) and (4.23). Fig. 4.9.b shows the current calculated from (4.22) and the current obtained from the simulation model.

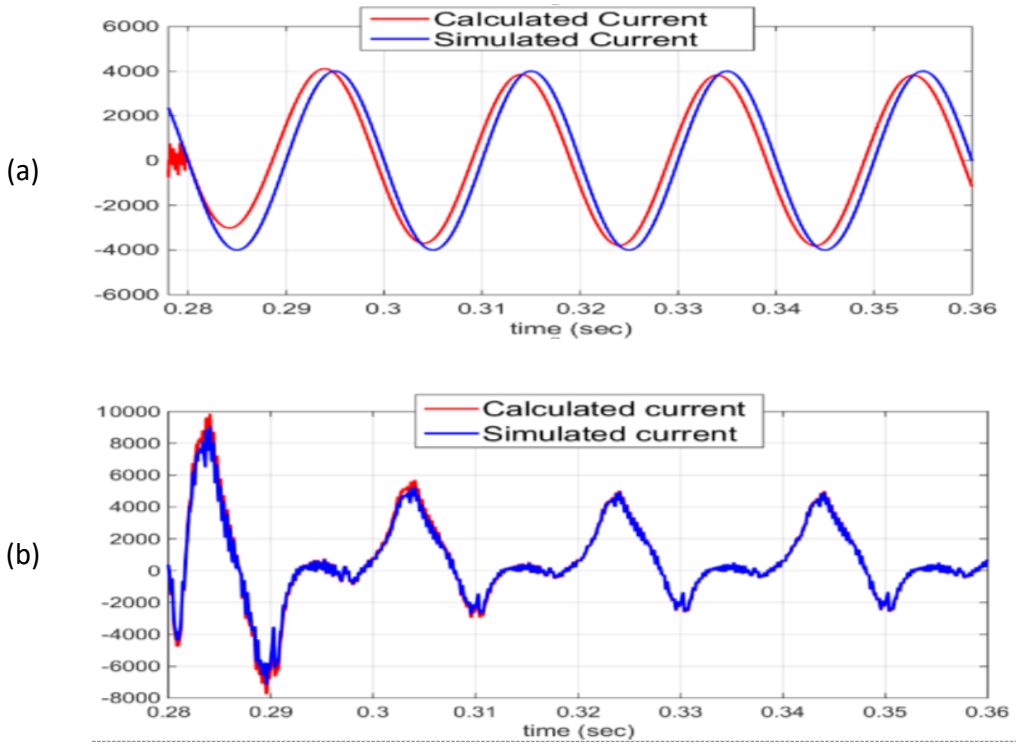

Figure 4.9: Simulations Results Under AC Fault Operating Conditions (a): Simulated and Calculated AC Grid Current and (b): Simulated and Calculated DC Grid Contribution

4.4.2 Fault Confining Validation

In this subsection, a 9-level MMC layout is used as the interlinking converter with the same switching frequency and voltages given in Subsection 4.4.1. However, each two half-bridge SMs are replaced with one SCSM to generate the same voltage level. The fault confining capability of the proposed MMC topology is illustrated by applying a pole to pole solid fault at t=0.4 to t=0.44. During this interval of time, the IGBTs signals are turned off to prevent the contribution of the AC side current into the DC fault. The simulation results for the fault condition are represented in Fig. 4.10. The MMC phase voltages are shown in Fig. 4.10.a. It is clear from Fig. 4.10.b that the ac grid currents are limited to zero during the fault making the ac layer contribution into the fault equals to zero and as a

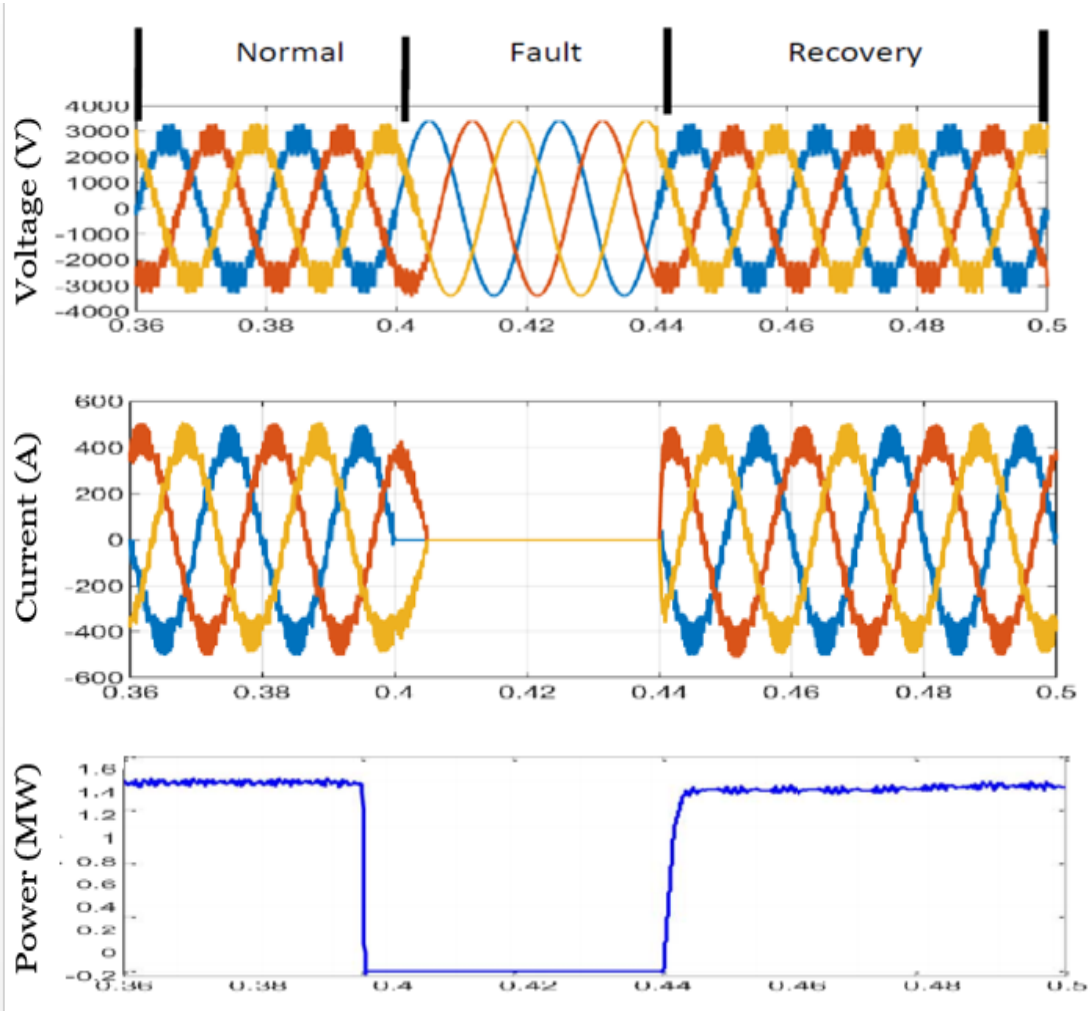

Figure 4.10: Simulations Results Under Fault Operating Conditions (a): MMC Phase Voltages, (b): AC grid currents, and (c): AC Grid ACtive Power

result the ac grid power is limited to zero as shown in Fig. 4.10.c. It is clear from the simulation results that the system returns to its normal operation when the fault is cleared by re-enabling the gating signals of the IGBTs.

4.5 Conclusions

The utilization of the modular multilevel converter in bilayer microgrids has been proposed in this Chapter. In the bilayer configuration, the two layers (i.e., AC and DC) are interconnected through the IC, and hence a fault in the AC layer would impact the DC layer resulting in service interruption for the whole network. This issue represented a main obstacle in the implementation of the bilayer configuration. Replacing the conventional IC with MMC has proven to be an effective solution in preventing the current contribution from the healthy layer to the faulty layer. This quarantine is achieved by turning off the gating signals from IGBTs upon fault occurrence. As a result the SM will generate an opposing voltage so that the diodes are reversed biased. The simulation results highlight the effectiveness of the SCSM in blocking the contributions of the fault current from one layer to the other. Additionally, reactivating the gating signals to the IGBTs helped to restore system's normal conditions when the fault is cleared. This fault confining prevents unnecessary disconnection of the two layers and hence enhances system reliability.

A mathematical formulation for the dynamic equations describing the fault current behavior in bilayer microgrids has also been presented in this Chapter. The MMC has been utilized as the IC between the DC and AC layers. The formulas were obtained for two possible fault scenarios including AC and DC layers faults to determine the dynamics and the contribution of both grids into each fault scenario. A simulation model with a nine-level MMC has been implemented using MATLAB/SIMULINK during these fault scenarios. The obtained results are compared with the mathematical model presented in the chapter to verify the validity of the mathematical models. The agreement between the simulation results and the mathematical model output shows the validity of the proposed mathematical formulas.

Chapter 5

A Planning Framework for the Interconnection of Smart Microgrids

5.1 Introduction

This chapter introduces a novel stochastic planning framework for the interconnection of different types (AC, DC, AC-DC hybrid, or bilayer) of μGs. The proposed planning framework determines the optimal connectivity of the IμGs that minimizes the installation and operation cost to provide the following planning decisions: the candidate buses of each μG, where the candidate bus is the bus that maximizes/minimizes the μG capability to export/import power to/from the neighboring μGs; the interconnection lines that will form the IμG network, the types of these lines (AC/DC); and the locations and sizes of the interlinking converters (ICs) used to interconnect two μGs of different types of power (AC/DC).

The proposed framework has been employed for finding the optimal configuration of the interconnection lines for a case study that included six μGs of different types. Additionally, in order to highlight benefits of μGs interconnection, the case-study system evaluated the role of microgrids interconnection in reducing the amount of curtailed power.

This chapter is organized as follows: Section 5.2 discusses the IμG configuration and the advantages of μG interconnection. Section 5.3 formulates the planning framework and

the associated optimization problems. The illustration of the planning framework, along with a flowchart describing the planning strategy is presented in Section 5.4. Section 5.5 describes the case studies that demonstrated the effectiveness of the proposed planning framework and μGs interconnection. Finally, the chapter is concluded in Section 5.6.

5.2 Interconnection of Multi-Micogrids

The uncertainties of the renewable-based DGs and the limited capacities of μGs have introduced several challenges to the planning and operation of μGs. As such, power system planners have always been concerned with the proper planning of μGs to 1) diminish the risk associating the uncertainties of load demands and renewable DGs, and 2) reduce the system investment cost by preventing the over-design of the μG DGs. As a result, the IμGs was promoted as one of the promising solutions to satisfy the previously mentioned objectives.

The interconnection of μGs provides numerous advantages and benefits that can be summarized as follows:

1. Increasing the system reliability and decreasing the probability of overloading.
2. Reducing the load shedding and the DGs curtailment.
3. Minimizing the dependency on the main grid, and hence facilitating the supply of power to remote areas effectively.

As shown in Fig. 5.1, the IμGs are formed when two or more μGs (AC, DC, or AC-DC hybrid) are connected through AC/DC lines and ICs. The types of lines (AC or DC) connecting the IμGs are dependent on the μGs types, while the sizes of the ICs connecting the IμGs are dependent on the power transfer between them. The amount of power transfer is dependent on the network configuration of the IμGs, the candidate bus in each μG, in addition to the load and generation nature of each μG. In this work, two planning stages are implemented in order to achieve the optimal connectivity of the IμGs at a minimum cost. The objectives of the two stages are as follows:

1. Stage 1: The objective is to determine the candidate bus for each μG. The candidate bus of each microgrid is used to interconnect this microgrid with other microgrids.

2. Stage 2: The objective is to determine the optimal connectivity of IμGs by providing the following decisions: 1) the locations of the lines connecting the μGs, 2) the types of the lines (AC or DC) connecting the μGs, and 3) the sizes of the ICs needed for connecting the μGs. It is worth noting that the μGs are properly planned and existing, while the planning framework aims to optimize the connectivity of the IμGs.

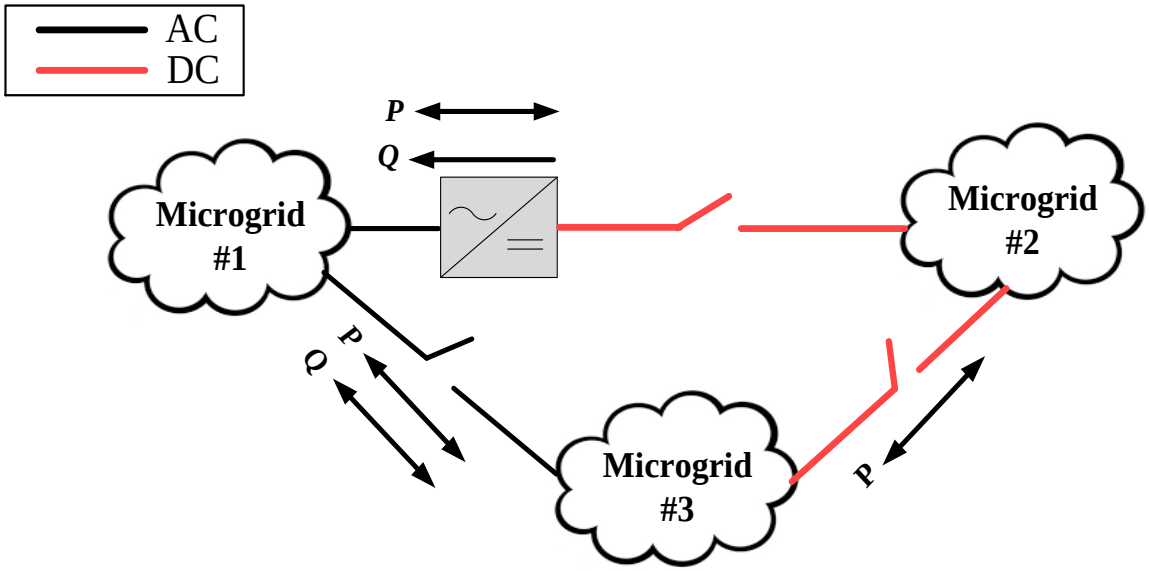

Figure 5.1: Interconnected Microgrids.

5.3 Planning Framework

Two stages are integrated in order to determine the optimal interconnection of μGs. The first stage involves the determination of the candidate bus in each μG. The candidate bus maximizes/minimizes the μG capability to export/import power to/from the neighboring μGs. After the determination of the candidate bus of each μG, the second-stage will be utilized to provide the interconnection decisions: 1) how the μGs are interconnected, 2) the types (AC/DC) of the lines connecting the μGs, and 3) the sizes of the ICs needed for connecting the μGs.

5.3.1 Stage-1 Formulation

This stage is formulated as an optimization problem in GAMS to determine the candidate bus of each μG. The objective function and constraints can be described as follows:

I. Objective Function

The objective of Stage-1 is to maximize the capability of the μG to export power. This objective is achieved through maximizing the apparent power of the virtual power variable (VPV) at every bus n in μG q, where VPV is a virtual load/DG that is used for determining the μG capability to export/import power.

$$\max \; S_n^{vpv} = \mathbb{E}(S_{n,s}^{vpv}) \quad , \quad \forall \; n \in N_{\mu G_q}^b \tag{5.1}$$

where $N_{\mu G_q}^b$ is the set of buses in μG_q; q is the index of μGs; S_n^{vpv} is the value of the apparent power of the VPV at bus n; $S_{n,s}^{vpv}$ is the VPV apparent power at bus n for an MCS scenario s; and $\mathbb{E}(S_{n,s}^{vpv})$ is the expected value of $S_{n,s}^{vpv}$.

II. Optimization Constraints

Four types of constraints are considered in this stage: 1) the active and reactive power balance equations (5.2)−(5.3), 2) the upper and lower limits of the voltage magnitude and angle at each bus (5.4)−(5.5), in addition to the power capacity of the network lines (5.6), 3) the active and reactive power limits for the energy resources (5.7)−(5.9), and 4) the capacity limits and the modulation-index limits of the AC-DC converters (5.10)−(5.11).

$$P_n^{inj} = P_n^{cal} \quad , \quad \forall \; n \in N_{\mu G_q}^b \tag{5.2}$$

$$Q_n^{inj} = Q_n^{cal} \quad , \quad \forall \; n \in N_{\mu G_q}^b \tag{5.3}$$

$$V_n^{min} \leq V_n \leq V_n^{max} \quad , \quad \forall \; n \in N_{\mu G_q}^b \tag{5.4}$$

$$\theta_n^{min} \leq \theta_n \leq \theta_n^{max} \quad , \quad \forall \; n \in N_{\mu G_q}^b \tag{5.5}$$

$$\sqrt{P_{nm}^2 + Q_{nm}^2} \; \leq \; S_{nm}^{max} \quad , \quad \forall \; n, m \in N_{\mu G_q}^b \tag{5.6}$$

$$P_{G_i}^{ac,min} \leq P_{G_i}^{ac} \leq P_{G_i}^{ac,max} \quad , \quad \forall\, i \in N_{\mu G_q}^{G,ac} \tag{5.7}$$

$$P_{G_j}^{dc,min} \leq P_{G_j}^{dc} \leq P_{G_j}^{dc,max} \quad , \quad \forall\, j \in N_{\mu G_q}^{G,dc} \tag{5.8}$$

$$Q_{G_i}^{ac,min} \leq Q_{G_i}^{ac} \leq Q_{G_i}^{ac,max} \quad , \quad \forall\, i \in N_{\mu G_q}^{G,ac} \tag{5.9}$$

$$\sqrt{(P_c^{ac})^2 + (Q_c^{ac})^2} \leq S_c^{max} \quad , \quad \forall\, c \in N_{\mu G_q}^{c} \tag{5.10}$$

$$M_c^{min} \leq M_c \leq M_c^{max} \quad , \quad \forall\, c \in N_{\mu G_q}^{c} \tag{5.11}$$

where P_n^{inj}, P_n^{cal}, Q_n^{inj}, and Q_n^{cal} are given in (5.12)-(5.15), these variables represent the injected/calculated active/reactive power at bus n; A_n is a binary element representing bus n type whose value is 0 if bus n is AC, and 1 if bus n is DC; $\overline{A_n}$ is the logical inverse of A_n, equal to $(1 - A_n)$; G_{nm} and B_{nm} are the respective conductance and susceptance of the AC line connecting buses n and m (in p.u.); G_{nm}^{dc} is the conductance of the DC line connecting buses n and m (in p.u); $\eta_{c\text{-}n\text{-}i}$ is the efficiency of an inverter at bus n (as a %); $\eta_{c\text{-}n\text{-}r}$ is the efficiency of a rectifier at bus n (as a %); K_{nm} is a binary element representing the connection between bus n and bus m (It is equal to 0 if no line connecting buses n and m, and equal to 1 if a line connecting buses n and m). V_n and θ_n are the voltage magnitude and angle at bus n, respectively; P_{nm}, Q_{nm}, and S_{nm} are the active, reactive, and apparent power transmitted through line nm, respectively; $N_{\mu G_q}^{G,ac}$ and $N_{\mu G_q}^{G,dc}$ are the sets of AC and DC energy resources in μG_q, respectively; $P_{G_i}^{ac}$ and $Q_{G_i}^{ac}$ are the respective active and reactive power of AC resource i; $P_{G_j}^{dc}$ is the output power of DC resource j; $N_{\mu G_q}^{c}$ is the set of AC-DC converters in μG_q; P_c^{ac}, Q_c^{ac}, and S_c are the active, reactive, and apparent power at the AC side of the AC-DC converter c, respectively; M_c is the modulation index of the converter c; and $\blacklozenge^{max/min}$ is the maximum/minimum limit of the variable $\blacklozenge$.

$$\begin{aligned} P_n^{inj} = \overline{A_n} \Big(P_{Gn}^{ac} - P_{Ln}^{ac} + \eta_{c\text{-}n\text{-}i}\, P_{Gn}^{dc} - \eta_{c\text{-}n\text{-}r}^{-1}\, P_{Ln}^{dc} \Big) \\ + A_n \Big(P_{Gn}^{dc} - P_{Ln}^{dc} + \eta_{c\text{-}n\text{-}r}\, P_{Gn}^{ac} - \eta_{c\text{-}n\text{-}i}^{-1}\, P_{Ln}^{ac} \Big) \ , \ \forall\, n \in N_{\mu G_q}^{b} \end{aligned} \tag{5.12}$$

$$P_n^{cal} = \sum_{\substack{m=1 \\ m \neq n}}^{N_b} K_{nm} \Bigg[\overline{A_n}\ \overline{A_m}\ \Big(V_n^2\, G_{nm} - V_n\, V_m\, (G_{nm}\, \cos\theta_{nm} + B_{nm}\, \sin\theta_{nm}) \Big) + A_n\ \overline{A_m}\ \Big(G_{nm}^{dc}\, (V_n^2 - V_n\, M_{c\text{-}mn}^{-1}\, V_m) \Big) + \overline{A_n}\ A_m\ \Big(G_{nm}^{dc}\, (M_{c\text{-}nm}^{-2}\, V_n^2 - M_{c\text{-}nm}^{-1}\, V_n\, V_m) + P_{c\text{-}nm}^{loss} \Big) + A_n\ A_m\ \Big(G_{nm}^{dc}\, (V_n^2 - V_n\, V_m) \Big) \Bigg]\ ,\ \forall\ n \in N_{\mu G_q}^b \quad (5.13)$$

$$Q_n^{inj} = \overline{A_n} \Big(Q_{Gn}^{ac} - Q_{Ln}^{ac} + Q_{Gn\text{-}c}^{dc} - Q_{Ln\text{-}c}^{dc} \Big)\ ,\ \forall\ n \in N_{\mu G_q}^b \quad (5.14)$$

$$Q_n^{cal} = \sum_{\substack{m=1 \\ m \neq n}}^{N_b} K_{nm} \Bigg[\overline{A_n}\ \overline{A_m}\ \Big(-V_n^2\, B_{nm} - V_n\, V_m\, (G_{nm}\, \sin\theta_{nm} - B_{nm}\, \cos\theta_{nm}) \Big) + \overline{A_n}\ A_m\, Q_{c\text{-}nm} \Bigg]\ ,\ \forall\ n \in N_{\mu G_q}^b \quad (5.15)$$

The value of the converter power losses is related the active power of the converter, as in (5.16). The modulation index of converter c is calculated as a function of the AC and DC voltages, as expressed in (5.17).

$$P_c^{loss} = \beta_c\ |P_c^{ac}| \quad (5.16)$$

$$V_c^{ac} = M_c\ V_c^{dc} \quad (5.17)$$

where P_c^{loss} is the power losses of converter c; β_c is the power-loss coefficient for converter c; and $V_c^{ac/dc}$ is the voltage magnitude at the AC/DC side of converter c.

III. Candidate-Bus Selection

For the μG_q, the candidate bus o is the bus at which the value of the VPV is maximum, as follows:

$$S_o^{vpv} = \max_n\ (S_n^{vpv}) \quad (5.18)$$

It is worthwhile to note that only one candidate bus is selected for each μG with one type of power (AC or DC). However, for each AC-DC hybrid μG, two candidate buses are

selected (one is AC and the other is DC). Therefore, the number of the candidate buses in the IμGs equals to (the number of AC μGs + the number of DC μGs + 2 × the number of AC-DC hybrid μGs).

5.3.2 Stage-2 Formulation

The second stage involves two optimization problems as will be illustrated in the following explanations.

5.3.2.1 Primary Optimization Problem

The primary optimization problem is solved using a GA to find the optimal connectivity of the IμGs that minimizes the net present value of the total system costs.

I. Objective Function

The objective function is to minimize the total present cost value (C_{NPV}), as follows:

$$\min\ C_{NPV} = \left(C_{INV} + \sum_{t=1}^{T_P} \frac{C_{AOM,t}}{(1+IR')^t} \right) \tag{5.19}$$

where C_{INV} is the total investment costs; T_P is the number of years in the planning study; $C_{AOM,t}$ is the annual operation and maintenance costs at year t; and IR' is the effective interest rate that can be calculated in terms of the interest rate (IR) and the inflation rate (FR) as follows:

$$IR' = \frac{IR - FR}{1 + FR} \tag{5.20}$$

The equation for C_{INV}, and $C_{AOM,t}$ are given by

$$C_{INV} = \sum_{x \in N_{buses}^{cand}} \sum_{\substack{y \in N_{buses}^{cand} \\ y > x}} K_{xy} \Bigg[\overline{A_x}\ \overline{A_y} \left(C_l^{ac}\, L_{xy}^{ac} + 2\ C_{xy}^{cb,ac} \right) + \left(\overline{A_x}\ A_y + A_x\ \overline{A_y} \right) \left(C_l^{dc}\, L_{xy}^{dc} + C_c\, S_{c\text{-}xy}^{max} + C_{c\text{-}xy}^{cb,ac} + 2\ C_{c\text{-}xy}^{cb,dc} \right) + A_x\ A_y \left(C_l^{dc}\, L_{xy}^{dc} + 2\ C_{xy}^{cb,dc} \right) \Bigg] \tag{5.21}$$

$$C_{AOM,t}\ =\ 8760\ \ \mathbb{E}(C_{OPF,s,t})\ +\ \lambda_{AM}\ \ C_{INV} \tag{5.22}$$

where N_{buses}^{cand} is the set of candidate buses; x and y are the indices of candidate buses; K_{xy} is a binary element representing the connection between the candidate buses x and y (i.e., K_{xy} is equal to 0 if no line connecting buses x and y, and equal to 1 if a line connecting buses x and y); A_x and A_y are binary elements representing the types of the candidate buses x and y; $C_l^{ac/dc}$ is the cost (in \$/mile) of the AC/DC lines; $L_{xy}^{ac/dc}$ is the distance (in miles) of an AC/DC line connecting two candidate buses x and y; $C_{xy}^{cb,ac/dc}$ is the cost of an AC/DC breaker installed in the line connecting candidate buses x and y; C_c is the IC cost (in \$/kVA); $S_{c-xy}^{c\text{-}max}$ is the rated apparent power of the IC required for connecting two different types (AC and DC) of candidate buses x and y; $C_{c\text{-}xy}^{cb,ac/dc}$ is the cost of the breaker at the AC/DC side of the IC connecting two candidate buses x and y; $C_{OPF,s,t}$ is the optimal operation cost (in \$/h) for an MCS scenario s at year t; $\mathbb{E}(C_{OPF,s,t})$ is the expected value of the operation cost at year t; and λ_{AM} is the annual maintenance cost as a % of the investment cost.

It should be noted that the apparent power of the IC connecting two candidate buses x and y for different MCS scenarios is represented by a stochastic variable $S_{c\text{-}xy,s}$. The IC rated-power ($S_{c\text{-}xy}^{c\text{-}max}$) is calculated as $max\,(S_{c\text{-}xy,s})$, while the system operation cost is represented by the expected value $\mathbb{E}(C_{OPF,s})$. For each MCS scenario for each GA chromosome, the values of the stochastic variables $\left(S_{c\text{-}xy,s}\right.$ and $\left.C_{OPF,s}\right)$ are obtained from the solution of the secondary optimization problem.

II. Optimization Constraints

Two constraints are considered in the primary optimization problem: a) the integer constraint (5.23) that is associated with the binary variables of the connection matrix K_{xy}, and b) the bus-connectivity constraint (5.24).

$$K_{xy} \in \{0,1\} \quad , \quad \forall\ x,y \in N_{buses}^{cand} \tag{5.23}$$

$$N_{L,x}^{min} \ \leq \sum_{\substack{y \in N_{buses}^{cand} \\ y \neq x}} K_{xy} \ \leq \ N_{L,x}^{max} \quad , \quad \forall\ x \in N_{buses}^{cand} \tag{5.24}$$

where $N_{L,x}^{max/min}$ is the maximum/minimum permissible number of interconnection lines that can be connected to candidate bus x.

5.3.2.2 Secondary Optimization Problem

The secondary optimization problem is implemented in GAMS to solve the OPF problem for each MCS scenario for each GA chromosome.

I. Objective Function

The objective is to minimize the total operation cost (C_{OPF}), as described in (5.25).

$$\min\ C_{OPF} = \sum_{q \in N_{\mu G}} C_{\mu G_q}^{OPF} \tag{5.25}$$

where

$$C_{\mu G_q}^{OPF} = \sum_{i \in N_{\mu G_q}^{G,ac}} C_{G_i}^{ac}\ P_{G_i}^{ac} + \sum_{j \in N_{\mu G_q}^{G,dc}} C_{G_j}^{dc}\ P_{G_j}^{dc} + \sum_{r \in N_{\mu G}} C_{imp}\ P_{rq} - \sum_{r \in N_{\mu G}} C_{exp}\ P_{qr} \tag{5.26}$$

where q and r are the indices of μGs; $C_{\mu G_q}^{OPF}$ is the operation cost of μG_q; $N_{\mu G}$ is the set of μGs; $N_{\mu G_q}^{G,ac}$ and $N_{\mu G_q}^{G,dc}$ are the sets of AC and DC energy resources in μG_q, respectively; $C_{G_i}^{ac}$ and $C_{G_j}^{dc}$ are the generation costs (in \$/MWh) of the AC and DC energy resources,

respectively; C_{imp} and C_{exp} are the cost of importing and exporting power (in \$/MWh), respectively; and P_{rq} is the active power transmitted from μG_r to μG_q.

II. Optimization Constraints

For the secondary optimization problem, the OPF constraints given in (5.2)−(5.15) are applied to all buses and DGs in the IμG system.

5.4 Strategy of the IμGs Planning

As previously mentioned in Section 5.3, the proposed planning framework aims to achieve the optimal connectivity for the IμGs that 1) minimizes the total system costs and 2) maximizes the amount of available power that can be exchanged between the μGs. In order to achieve these objectives, the planning framework determines the optimal candidate buses and the optimal connectivity of the IμGs network through the integration of two stages. Stage 1 is concerned with the determination of the candidate buses that will be used in the interconnection of the μGs, while Stage 2 is concerned with the determination of the optimal connectivity of the IμGs. It should be noted that the planning framework takes into consideration the uncertainties of the renewable DGs and the variations in the load demands for achieving a reliable and realistic solution. Stage 2 involves two optimization problems: 1) the primary problem is formulated using GA, and 2) the secondary problem is formulated in GAMS and solved for every GA chromosome for every MCS scenario.

5.4.1 Planning Framework Illustration

The flowchart of the proposed interconnection planning framework is presented in Fig. 5.2, and the procedures comprising it can be described as follows:

1. For a given μG_q, set the VPV at all buses to zero except for a selected bus n.
2. Select an MCS scenario that represents the variations in load demands and renewable energy resources.

3. For the selected MCS scenario, solve the OPF problem in GAMS in order to determine the maximum value of the VPV at bus n. This problem aims to maximize (5.1), subjected to the OPF constraints given in (5.2)−(5.11).

4. Repeat Steps 2 and 3 until the MCS stopping criterion is satisfied.

5. Calculate the expected value of the VPV for bus n.

6. Repeat Steps 1 to 5 for each bus in μG_q.

7. Rank the buses according to the calculated VPV values. The bus with the greatest VPV is then selected as the candidate bus for μG_q, as described in (5.14).

8. Repeat Steps 1 to 7 for each μG.

9. Initialize a GA population that consists of number of chromosomes, where each chromosome represents a possible configuration of the IμGs, based on the matrix K_{xy}.

10. For each chromosome in the current GA generation, an MCS scenario is selected.

11. GAMS is called to solve the secondary optimization problem to minimize (5.25) and to calculate the corresponding operation cost.

12. The solution of the secondary optimization problem is examined; if a feasible solution is obtained, the optimal operation cost ($C_{OPF,s}$) is calculated; otherwise, a very large value is assigned to the system cost.

13. If the MCS stopping criteria is satisfied (i.e., the maximum number of iterations is reached), go to Step 14; otherwise, another MCS scenario is selected and Steps 11 to 12 are repeated.

14. The operation cost of the current chromosome represented by the expected value $\mathbb{E}(C_{OPF,s})$ is calculated if the desired confidence level is achieved (i.e., 95 % solutions are feasible) ; otherwise, the corresponding chromosome is rejected.

15. For the current chromosome, the total present cost value is calculated using (5.15).

16. Repeat Steps 10 to 15 for each chromosome in the current GA generation, and then evaluate the GA objective function and constraints.

17. After solving all the current generation chromosomes, check the GA stopping criteria. If the GA stopping criteria is not satisfied, then the GA generation is updated by applying the GA operations (reproduction, crossover, and mutation) and the Steps 10 to 16 are repeated.

18. After the GA process is terminated, the optimal configuration connecting the IμGs is obtained with the corresponding costs.

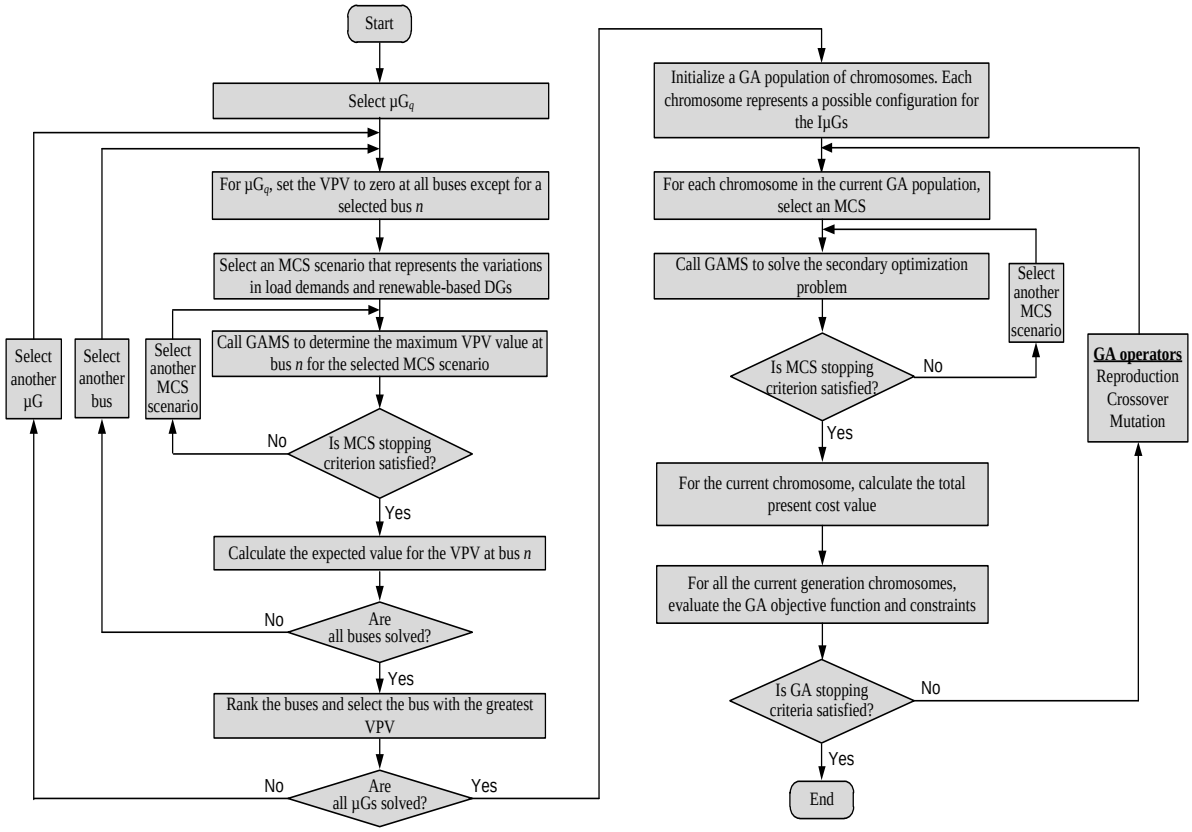

Figure 5.2: Flowchart for the Proposed Interconnection Planning Model

5.5 Case Studies

Six different types (AC, DC, AC-DC hybrid, and Bilayer) of microgrids are considered in the case under study, where each μG can have various types (AC/DC) of loads and DGs, as shown in Fig. 5.3. This case study elaborates and validates the planning framework capability in determining the optimal connectivity of the IμGs. Additionally, the case study validates the benefits achieved from the interconnection of μGs in terms of load curtailment by evaluating the amount of curtailed power (from the loads of the faulty μG for a single DG failure) for two cases: 1) Case 1 at which the μGs are islanded, and 2) Case 2 at which the μGs are interconnected. The proposed framework utilizes the MCS method and the stochastic models presented in [102], in which the seasonal stochastic variations associated with renewable-based DGs, load demands, and EVS demands were modeled based on the data given in [103–105].

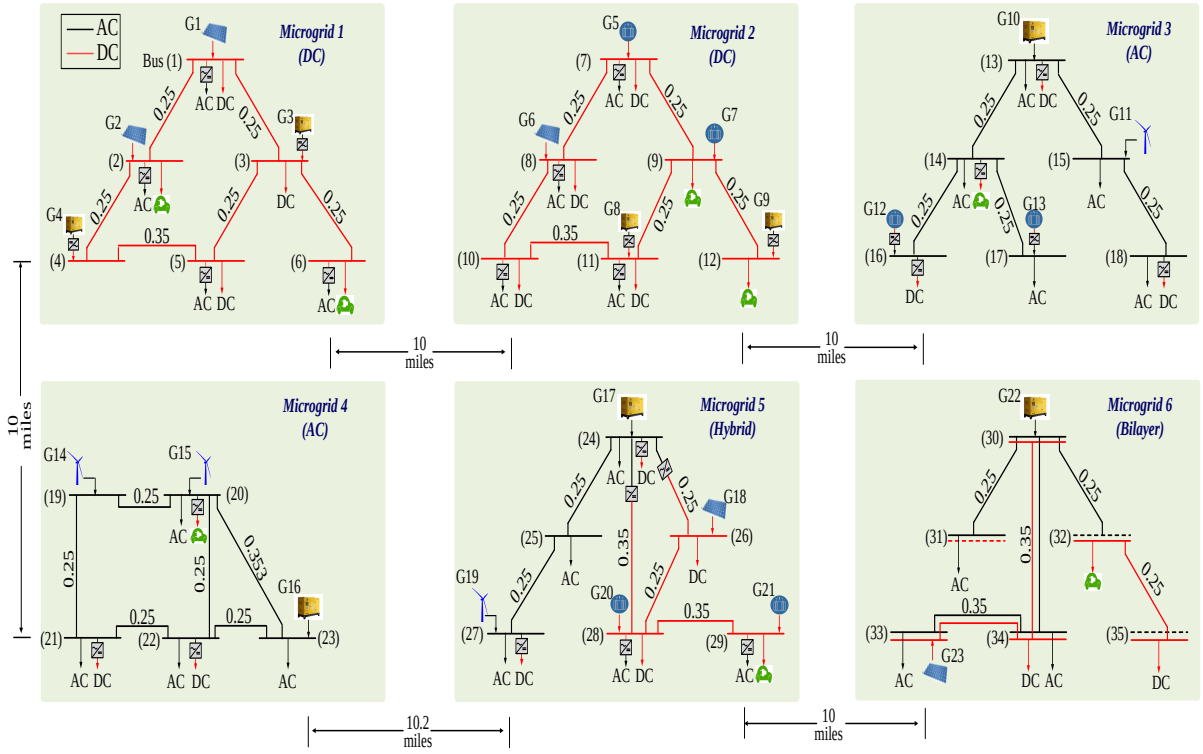

Figure 5.3: Interconnected Microgrids

As discussed in Sections 5.3 and 5.4, the planning framework aims to find the optimal connectivity of the IμGs by determining the following decisions:

1. The candidate bus of each μG.
2. The interconnection lines forming the IμGs network.
3. The types of the lines (AC or DC) connecting the μGs.
4. The sizes of the ICs connecting different types of μGs (AC and DC).

The distances (in miles) between the μGs under study, in addition to the distances (in miles) between the buses of each μG are given in Fig. 5.3. Table 5.1 summarizes the values and limits of the system and economic parameters. AWG #2 aluminum conductor steel-reinforced (ACSR) cables were used for the μGs lines (AC/DC) whose impedances are summarized in Table 5.2. AWG #3/0 ACSR cables were used for the interconnection lines (AC/DC). The DC resistance of this type of cable is (0.5295 Ω/mile), while the AC impedance is ($0.5459 + \text{j}0.5781$ Ω/mile).

Table 5.1: Input Parameters for the Planning Model

System Parameters	
Base values (S_{base}, V^{ac}_{base}, V^{dc}_{base})	10 MVA, 4.16 kV, 6.8 kV
Voltage magnitude permissible limits	0.95 to 1.05 pu
Voltage angle permissible limits	$-\pi/4$ to $\pi/4$ rad
Modulation index permissible limits	0.77 to 1.0
AC-DC converters efficiency	95 %
Number of MCS	10,000
Economic Parameters	
Interest rate-bilayer	7.5 % [45]
Inflation rate	1.0 % [95]
AC-DC converters cost	170.0 $/kVA [92]
Lines cost	28.0 k$/mile/conductor [93]
Circuit breakers cost	26.0 k$/unit [94]

Table 5.2: Impedances of the Microgrids Lines

From Bus	To Bus	Resistance (Ω)	Reactance (Ω)	From Bus	To Bus	Resistance (Ω)	Reactance (Ω)
1	2	0.3353	–	21	22	0.3419	0.1680
1	3	0.3353	–	22	23	0.3419	0.1680
2	4	0.3353	–	24	25	0.3419	0.1680
3	5	0.3353	–	24	26	0.3353	–
3	6	0.3353	–	24	28	0.4694	–
4	5	0.4694	–	25	27	0.3419	0.1680
7	8	0.3353	–	26	28	0.3353	–
7	9	0.3353	–	28	29	0.4694	–
8	10	0.3353	–	30	31	0.3419	0.1680
9	11	0.3353	–	30	32	0.3419	0.1680
9	12	0.3353	–	31	33	0.3419	0.1680
10	11	0.4694	–	32	35	0.3419	0.1680
13	14	0.3419	0.1680	33	36	0.3419	0.1680
13	15	0.3419	0.1680	30’	31’	0.3353	–
14	16	0.3419	0.1680	30’	32’	0.3353	–
14	17	0.3419	0.1680	31’	33’	0.3353	–
15	18	0.3419	0.1680	32’	34’	0.3353	–
19	20	0.3419	0.1680	32’	35’	0.3353	–
19	21	0.3419	0.1680	33’	34’	0.4694	–
20	22	0.3419	0.1680	–	–	–	–
20	23	0.4820	0.2369	–	–	–	–

Table 5.3 shows the operational costs of the AC and DC energy resources [106], [107], while Table 5.4 shows the active and reactive power limits of the system energy resources, in addition to the peak load demands.

Table 5.3: GA Parameters

DG Type	Operational Cost ($/ MWh)
Solar PV	8.0
Wind DG	10.0
Diesel DG	30.40
Fuel cells	26.70

Table 5.4: Loads and Energy Resources of the System Under Study

	Load Demands			**Energy Resources**				
Zone No.	P_L^{ac} (MW)	Q_L^{ac} (MVAR)	P_L^{dc} (MW)	Type	P_G^{max} (MW)	P_G^{min} (MW)	Q_G^{max} (MVAr)	Q_G^{min} (MVAr)
1	0.25	0.125	0.25	PV DG	1.00	–	–	–
2	0.25	0.125	0.50	PV DG	1.00	–	–	–
3	–	–	0.25	Diesel	1.00	0.10	0.50	0.05
4	–	–	–	Diesel	1.00	0.10	0.50	0.05
5	0.25	0.125	0.50	–	–	–	–	–
6	0.25	0.125	0.50	–	–	–	–	–
7	0.50	0.25	0.25	Fuel cell	1.50	0.20	–	–
8	0.50	0.25	0.50	PV DG	0.75	–	–	–
9	0.75	0.35	0.80	Fuel cell	0.75	0.10	–	–
10	0.25	0.125	0.75	–	–	–	–	–
11	0.25	0.125	0.25	Diesel	0.50	0.05	0.25	0.025
12	–	–	0.25	Diesel	1.25	0.125	0.60	0.06
13	0.50	0.25	0.25	Diesel	2.00	0.20	1.00	0.10
14	0.50	0.25	0.25	–	–	–	–	–
15	0.50	0.25	–	Wind DG	1.00	–	–	–
16	–	–	0.25	Fuel cell	0.50	0.075	–	–
17	0.50	0.25	–	Fuel cell	1.00	0.15	–	–
18	0.25	0.125	0.25	–	–	–	–	–
19	–	–	–	Wind DG	1.00	–	–	–
20	0.50	0.25	0.25	Wind DG	1.00	–	–	–
21	0.50	0.25	0.25	–	–	–	–	–
22	0.25	0.125	0.25	–	–	–	–	–
23	0.25	0.125	–	Diesel	1.00	0.10	0.50	0.05
24	1.00	0.50	0.50	Diesel	0.50	0.05	0.25	0.025
25	0.50	0.25	–	–	–	–	–	–
26	–	–	0.25	PV DG	0.80	–	–	–
27	0.50	0.25	0.25	Wind DG	1.00	–	–	–
28	0.40	0.20	0.25	Fuel cell	0.80	0.12	–	–
29	0.25	0.125	0.20	Fuel cell	1.00	0.15	–	–
30	–	–	–	Diesel	2.00	0.20	1.00	0.10
31	0.50	0.25	–	–	–	–	–	–
32	–	–	0.25	–	–	–	–	–
33	0.50	0.25	–	PV DG	0.50	–	–	–
34	0.40	0.20	0.25	–	–	–	–	–
35	–	–	0.20	–	–	–	–	–

5.5.1 Simulations Results

The possible network lines for interconnecting the μGs under study are represented in Fig. 5.4 by dotted lines, where each line can be AC or DC. It is worth noting that only the possible economic connections were considered, where each μG can be connected to the neighboring μG in order to reduce the overall project cost. For instance, μG_3 can only be connected to μG_2 or/and μG_5. The bus connectivity constraints for all μGs were selected to be $N_L^{max} = 3$ and $N_L^{min} = 0$.

For the μGs under study, the candidate buses obtained from Stage 1 are bus 3 for μG_1, bus 12 for μG_2, bus 13 for μG_3, bus 23 for μG_4, buses 24 and 29 for μG_5, and bus 30 for μG_6. The optimal configuration representing the connectivity of the IμGs obtained from Stage 2 is shown in Fig. 5.5. The obtained configuration from the planning framework includes six interconnection lines and three ICs connecting the μGs as follows: a DC line connecting μG_1 to μG_2, a DC line with an IC for connecting μG_1 to μG_4, a DC line with an IC connecting μG_3 to μG_6, a DC line with an IC for connecting μG_4 to μG_5, and a DC line connecting μG_5 to μG_6.

Despite the existence of AC buses in μG_3, μG_4, μG_5, and μG_6, the planning framework suggested the connection of μG_3 to μG_6 and μG_4 to μG_5 through DC lines and ICs. One might think that the connection of these μGs by AC lines, as shown in Fig. 5.6 would be more beneficial to reduce the number of ICs. For that reason, the configuration obtained from the planning framework (Configuration 1 shown in Fig. 5.5), will be compared with this configuration at which μG_3, μG_4, and μG_5 are interconnected by AC lines (Configuration 2 shown in Fig. 5.6). Additionally, the loop Configuration (Configuration 3) is considered in this comparison as the benchmark configuration that was reported several times in the literature.

The system cost is crucial in the choice of the optimal configuration interconnecting the μGs. For that reason, a detailed analysis is carried out to investigate the cost of the obtained configuration. The present value is determined for a 15 years study period with an annual load growth rate of 0.7 %. The costs associated with Configuration 1, Configuration 2, and Configuration 3 are listed in Table 5.5. As can be seen from Table 5.5, Configuration 1 has three ICs with total size of 4 MVA, while Configuration 2 has only one IC with a size of 1 MVA, and finally Configuration 3 has Four ICs with total size of

4.2 MVA. Accordingly, the converters cost associated with Configuration 2 (0.170 M$) is lower than the converters cost of Configuration 1 (0.680 M$) and Configuration 3 (0.714 M$). However, the operation and interconnection lines costs of Configuration 1 were found to be lower than those of Configuration 2 and Configuration 3, which resulted in lower investment costs and net present cost of Configuration 1 compared to Configuration 2 and Configuration 3. The obtained results therefore show the effectiveness and the capability of the proposed planning framework in determining the optimal configuration interconnecting the IμGs that will result in minimum costs.

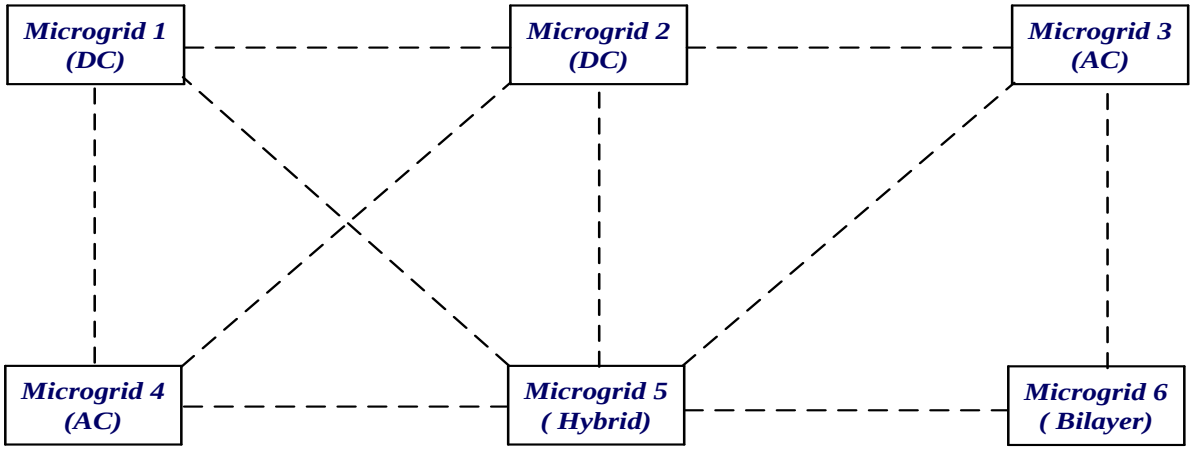

Figure 5.4: Possible Interconnections of Microgrids

Table 5.5: Comparison of Interconnected Microgrids Configurations

Cost (M$)	Configuration 1	Configuration 2	Configuration 3
Operation cost at year #15	2.263	2.299	2.308
Cost of Interconnection lines	2.800	4.200	3.360
Cost of converters	0.680	0.170	0.714
Cost of breakers	0.338	0.286	0.364
Total investment cost	3.818	4.656	4.438
Total operation cost for 15 years	20.911	21.287	21.328
Total net present cost	24.729	25.943	25.766

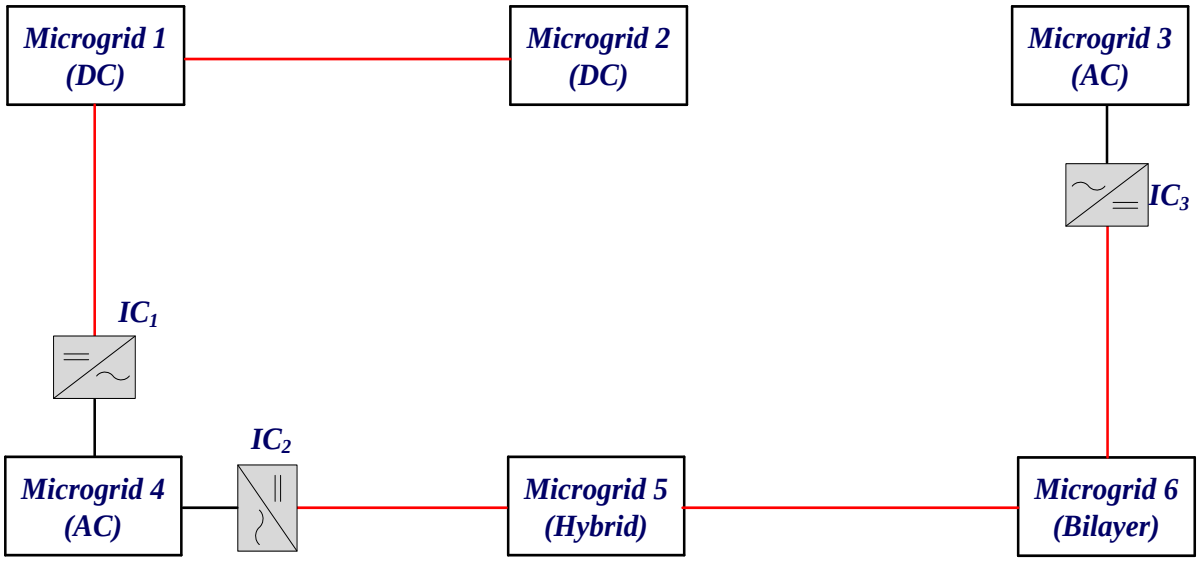

Figure 5.5: Proposed Interconnection of Microgrids (Configuration 1)

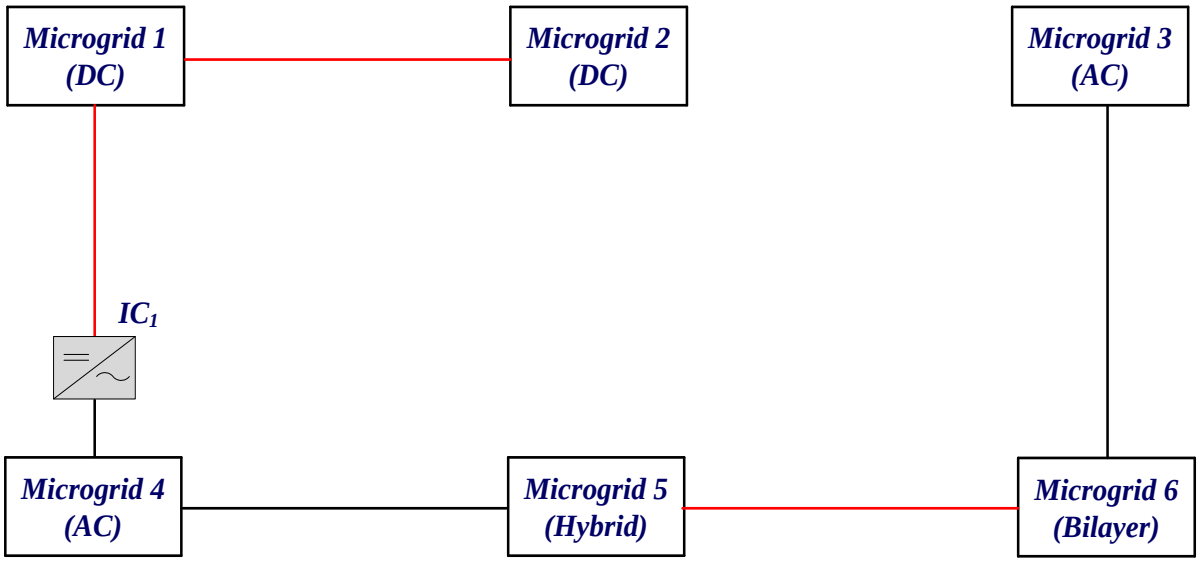

Figure 5.6: Possible Interconnection of Microgrids (Configuration 2)

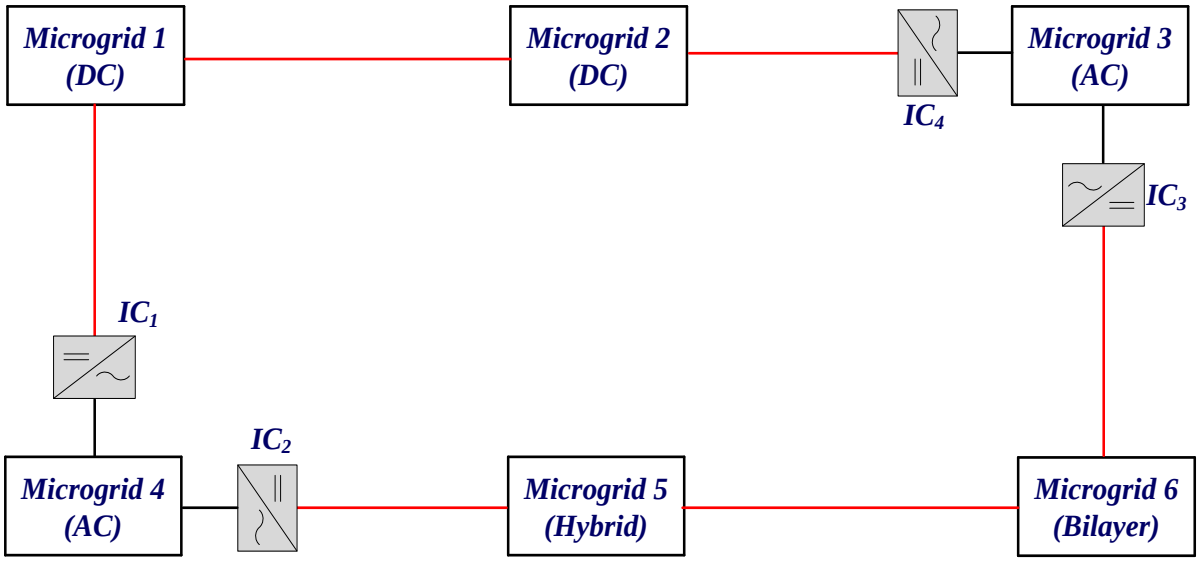

Figure 5.7: Possible Interconnection of Microgrids (Configuration 3)

5.5.2 Evaluation of the System Performance Under DG Failure

As mentioned earlier in this Chapter, reducing the load curtailment is considered among the main benefits of the μGs interconnection. In order to ensure that the obtained IμGs configuration achieves this benefit, the operation of the system under study is evaluated by determining the amount of curtailed power for a single DG failure (i.e., N-1 contingency criteria) for two cases. In the first case (Case 1), all the μGs are assumed to be islanded (no interconnection), while the second case (Case 2) involves the interconnection of the μGs shown in Fig.5.5 (Configuration 1). For the two cases, the operation of μGs is investigated assuming a single DG failure as follows:

1. Select μG_q.
2. DG $\#i$ is assumed to be unavailable ($P_{G_i} = 0$).
3. Calculate the required amount of power that should be curtailed from μG_q loads, if any, due to the unavailability of $DG\ \#i$ for two cases a) the μGs are islanded and b) the μGs are interconnected.

4. Repeat Steps 2-3 for each DG in μG_q.

5. Repeat Steps 1-4 for each μG.

The formulation of the problem is changed to account for the load curtailment. As a result, the objective function for the islanded μGs case (Case 1) becomes as follows:

$$\min \; C^{OPF}_{\mu G_q} \tag{5.27}$$

where

$$C^{OPF}_{\mu G_q} = \sum_{i \in N^{G,ac}_{\mu G_q}} C^{ac}_{G_i} \; P^{ac}_{G_i} + \sum_{j \in N^{G,dc}_{\mu G_q}} C^{dc}_{G_j} \; P^{dc}_{G_j} + \sum_{n \in N^{b}_{\mu G_q}} C_{cur} \; (P^{ac}_{Lcur,n} + P^{dc}_{Lcur,n}) \tag{5.28}$$

The IμGs objective function (Case 2) is defined as follows:

$$\min \sum_{q \in N_{\mu G}} C^{OPF}_{\mu G_q} \tag{5.29}$$

where

$$C^{OPF}_{\mu G_q} = \sum_{i \in N^{G,ac}_{\mu G_q}} C^{ac}_{G_i} \; P^{ac}_{G_i} + \sum_{j \in N^{G,dc}_{\mu G_q}} C^{dc}_{G_j} \; P^{dc}_{G_j} + \sum_{r \in N_{\mu G}} C_{imp} \; P_{rq} - \sum_{r \in N_{\mu G}} C_{exp} \; P_{qr} + \sum_{n \in N^{b}_{\mu G_q}} C_{cur} \; (P^{ac}_{Lcur,n} + P^{dc}_{Lcur,n}) \tag{5.30}$$

In addition, the active load power in equation (5.31) is modified to $(P^{ac/dc}_{Ln} - P^{ac/dc}_{Lcur,n})$, while the reactive load power in equation (5.14) is modified to $(Q^{ac}_{Ln} - Q^{ac}_{Lcur,n})$, where $P^{ac/dc}_{Lcur,n}$ and $Q^{ac}_{Lcur,n}$ are the curtailed active power from AC/DC loads and the curtailed reactive power from AC loads at bus n in the faulty μG. It is assumed that the power factor of each AC load is kept constant, so that the reactive power curtailed $Q^{ac}_{Lcur,n}$ is

proportional to the active power curtailed $P^{ac}_{Lcur,n}$, as described in (5.31).

$$Q^{ac}_{Lcur,n} = P^{ac}_{Lcur,n} * \tan\Big(\cos^{-1}(P.F_{Ln})\Big) \tag{5.31}$$

Where $P.F_{Ln}$ is the power factor of an Ac load at bus n.

The curtailed power results are summarized in Fig. 5.8. The results revealed that the interconnection of μGs reduced the amount of curtailed power significantly compared to the islanded μGs case as the μGs with excessive power are contributing to the μGs with power shortage.

For instance, the total curtailed power for all DG failures for the islanded μGs was 6094.604 kW, while it was only 1037.27 kW for the interconnected μGs which is 82.98 % less than the islanded μGs case.

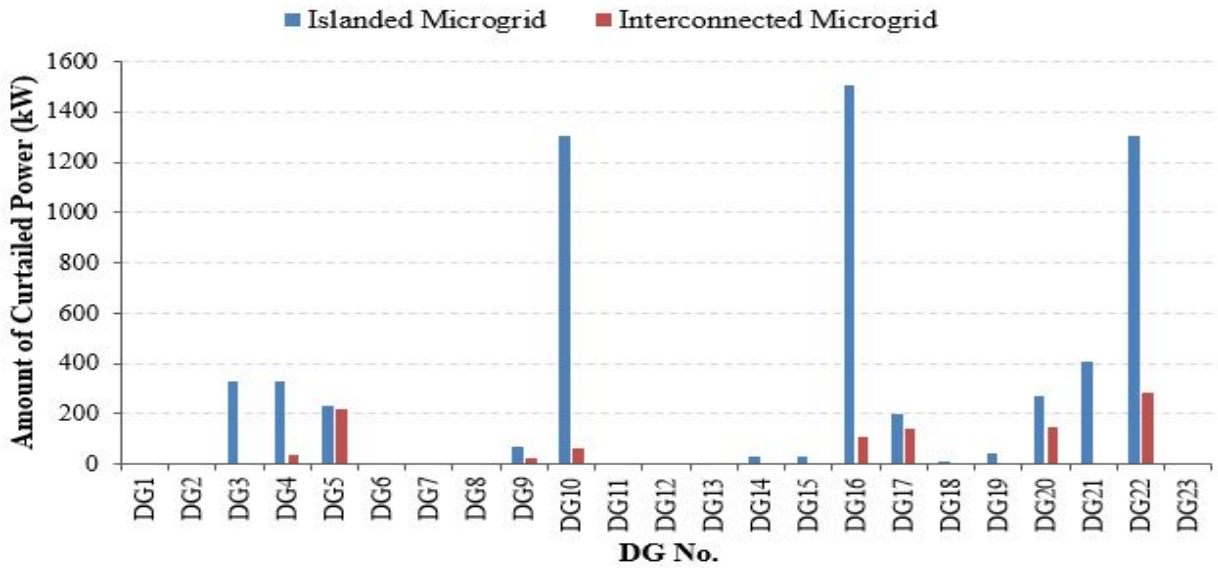

Figure 5.8: Curtailed Load Power: Islanded Microgrids vs Interconnected Microrgrids for the System given in

Fig. 5.3 Assuming Single DG Failure at a Time

5.6 Conclusion

A novel stochastic interconnection planning framework for μGs is proposed in this thesis. The planning framework determines the optimal connectivity of the IμGs that minimizes the investment and operation costs through the integration of two stages. The first stage determines the candidate buses of each μG, where the candidate bus is the bus that maximizes/minimizes the μG capability to export/import power to/from the neighboring μGs. The second stage involves two optimization problems, which aims to determine the optimal connectivity of the IμGs that minimizes the net present value of the system costs through the determination of: 1) the interconnection lines that will form the IμGs network, 2) the types of these lines (AC/DC), and 3) the locations and sizes of the interlinking converters used to interconnect two μGs with different types of power. The stochastic variations of the loads, EVs, and renewable-based DGs are taken into consideration by the proposed framework.

The proposed framework was applied to a system of six different types of μGs and the objective was to determine the optimal connectivity of the IμGs that minimizes the total system costs. The obtained results verified the capability of the framework in achieving the optimal configuration interconnecting the μGs for the system under study. The case-study system was solved assuming a single DG failure for two cases: obtained IμGs configuration and islanded μGs. The results revealed that the μGs interconnection significantly reduced the load curtailment significantly.

Chapter 6

Energy Trading Mechanism for Interconnected Microgrids

6.1 Introduction

This chapter proposes a dual action trading mechanism (DATM) that facilitates and arranges the energy trading between the IμGs. This mechanism aims to minimize the operation cost of the μGs and provide full utilization of renewable energy resources, and hence maximize the social welfare, while considering the self interest of each μG. These objectives are achieved through the implementation of two trading stages. Stage 1 is the conventional trading at which the μGs submit their bids/offers to the interconnected system operator to determine the trading price and the amount of energy exchange. Afterwards, the μGs are given the chance to participate in Stage 2 by submitting new offers/bids, however, they also have the option to not participate (i.e. Do nothing). Stage 2 results in a decrease in the μGs operation cost and reduces the renewable power curtailment by 1) providing the μG that have excess renewable power, which were not purchased in Stage 1 to submit new reduced offers to avoid the curtailment of the renewable energy resources unitized power and 2) providing the μGs with expensive energy resources to reduce their operation cost by purchasing cheap energy in Stage 2. The security and transparency of the transactions should be investigated to ensure the reliability and efficiency of the DATM. The coverage of this topic is beyond the scope of this thesis, nevertheless, this issue is considered as an

item for future work.

The proposed energy trading mechanism has been employed for a case study that included eight μGs, where each μG can have various types of loads and DGs (i.e. renewables and dispatchables). The energy exchange, operation cost, and amount of energy curtailed from renewable energy resources, for each μG, were calculated for two cases:

1. Case a: The μGs are interconnected, however conventional trading (CT) is considered (i.e., Stage 1 only)
2. Case b: The μGs are interconnected, and the proposed trading mechanism is implemented (i.e. Stage 1 and Stage 2)

This chapter is organized as follows: Section 6.2 introduces the trading mechanism principles, participants, and assumptions. Section 6.3 formulates the trading mechanism and the associated optimization problems. Section 6.4 describes the case studies that were employed for evaluating the effectiveness of the proposed trading mechanism. Finally, the chapter is concluded in Section 6.5.

6.2 Introduction to the Trading Mechanism

The advancement and developments of renewable-based DGs and the growing interest in environmental concerns have promoted the implementation of μGs. However, the interconnection of μGs has proven to have numerous benefits including enhanced system reliability and reduction in the renewable energy uncertainty through facilitating the energy exchange between the IμG.

The conventional markets (e.g. Ontario, California, New England, etc.) will not ensure reliability and full utilization of renewable power if applied to a system of isolated IμGs. In the conventional market, the offers are placed by bulk generators (e.g. Ontario Power Generation) and bids are placed by large loads or retailers that distribute the purchased energy to loads. In other words, the generators will always place offers and loads will always bid which is not the case in μGs. It is worth noting that the government policies

to promote the implementation of renewable energy at the distribution level such as net-metering program is capped to 100 kw, and hence does not have significant penetration to the power grid. In other words, most of the generators and loads are dispatchable and can receive instructions from the system operator to adjust their generation/demand.

In contrast, renewable-based DGs represent a huge portion of the μGs. As a result, although μGs are planned such that the generation capacity is greater than the load demand, overload problems may occur in the μGs due to their limited capacity and the uncertainty associated with the renewable-based DGs. Therefore μGs may act as generators at a certain instant (e.g. during the availability of renewable energy) while acting as a load at other instant (e.g. unavailability of renewable and high load demands) depending on the renewable-based DGs output power and load demands. This unique nature of μGs makes the implementation of the conventional market to a system of IμGs inappropriate. As such, an energy trading model is needed to facilitate and coordinate the energy exchange between the μGs.

The direct trading of the IμGs provides significant benefits to the sellers and buyers (i.e. μGs) compared to their trading with the utility [73] that can be summarized as follows:

1. Regulating and balance energy generation/consumption in microgrids
2. Reducing transmission losses compared to trading with the utility
3. Reducing electricity cost by enhancing the electricity price competitiveness
4. Promoting the utilization of renewable-based DGs
5. Providing an involvement to communities by creating new jobs and promote electricity trading within the μGs rather than with the utility

Based on the previous discussion, this thesis proposes a DATM that facilitates the energy trading between the IμGs in order to achieve the following objectives:

1. Utilizing the renewable-based DGs output power
2. Minimizing operational costs of the interconnected system while considering the self-interest of each microgrid

3. Minimizing loads curtailment
4. Maximizing social welfare.

6.2.1 Trading Mechanism Participants

An overview of the trading mechanism proposed in this thesis is presented in Fig. 6.1, which consists of two levels: upper level and lower level. The upper level participants includes interconnected system operator and μGs operators. While the lower level participants includes μG operator, in addition to loads and DGs within the μG. The role of each participant can be described as follows:

1. Interconnected System Operator
    - Accepts bids and offers from μGs
    - Analyze the offers and bids to determine the trading price and shares the results with the microgrids
    - Ensures the satisfaction of energy trading agreements
2. Microgrid Operators
    - Forecast load demands and renewable-based DGs output power
    - Maintain microgrid adequacy
    - Analyze microgrid data and estimates imported power required or available power that can be exported to maximize profit
    - Sends bids/offers to the interconnected system operator
3. Loads
    - Loads can sign an agreement allowing μG operator to curtail portion of their load demand in return for compensation
    - Loads purchase energy from its μG owner (operator) based on trading agreement

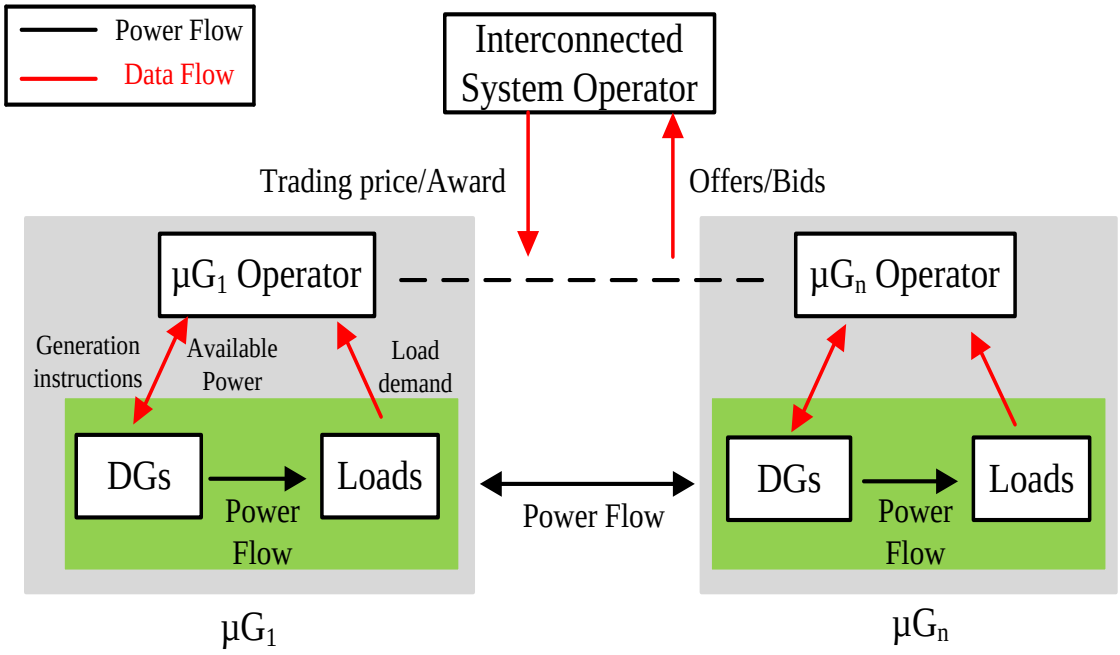

Figure 6.1: Overview of the Energy Trading mechanism.

6.2.2 Assumptions

The following assumptions and rules are considered in the DATM:

1. The IμGs network is isolated with no connection to the main grid
2. Each μG has one owner that owns all the μGs assets
3. The loads inside each μG purchase energy from their μG owner
4. Microgrid operator ensures the satisfaction of its local demand first before trading in the external market

6.3 Dual Action Trading Mechanism (DATM) Formulation

This section proposes a DATM that arranges the energy trading between the IμGs, while capturing the stochastic variations of the renewable-based DGs and load demands.

6.3.1 Stage 1

In this stage, each μG is scheduling its energy resources and forecasts its load demands in order to determine the surplus/deficit amount of power. Afterwards, μGs develop their bidding or offer in order to maximize their profit (i.e. selling energy to other μGs, if available) and decrease their costs (i.e. operational cost of DGs and cost of importing power). Based on the submitted bids and offer by each μG, the interconnected system operator determines the trading price and the award of each μG.

I. Lower Level

The lower level of the proposed model takes place within the μG boundaries in order to determine the optimal operation cost, as well as the available power that can be exported or the power that should be imported for each μG. It should be noted that the μGs will utilize their renewable and the minimum power limit output of the dispatchable DGs first before exporting any power to other μGs.

The objective of each μG is to dispatch its DGs and to meet its load demands while minimizing the total cost (i.e., operation cost of renewable-based DGs, operation cost of dispatchable DGs, and cost of curtailing power on particpants of load management program) as described in equation (6.1), subjected to the following constraints: 1) power balance constraint (6.2), 2) maximum power limit of renewable energy resources (6.3), 3) maximum and minimum power limit of dispatchable energy resources (6.4), and 4) the maximum permissible power that can be curtailed from those participating in load management program (6.5).

$$\min C_{op.cost} = \sum_{a=1}^{N_{G.R}} (C_{G.R})_a \, (P_{G.R})_a + \sum_{b=1}^{N_{G.D}} (C_{G.D})_b \, (P_{G.D})_b + \sum_{c=1}^{N_{L.M}} (C_{L.M})_c \, (P_{L.M})_c + C_{imp} \, P_{imp} \quad (6.1)$$

Subject to,

$$\sum_{a=1}^{N_{G.R}} (P_{G.R})_a + \sum_{b=1}^{N_{G.D}} (P_{G.D})_b + P_{imp} = - \sum_{c=1}^{N_{L.M}} (P_{L.M})_c + \sum_{d=1}^{N_{Loads}} (P_L)_d + P_{Loss} \quad (6.2)$$

$$(P_{G.R})_a \leq (P_{G.R})_a^{max} \quad (6.3)$$

$$(P_{G.D})_b^{min} \leq (P_{G.D})_b \leq (P_{G.D})_b^{max} \quad (6.4)$$

$$(P_{L.M}) \leq (P_{L.M})_c^{max} \quad (6.5)$$

Where a is the index of renewable energy resources; b is the index of dispatchable energy resources; c is the index of participants in load management program; d is the index of load demands; $(P_{G.R})_a$ is the power generated by renewable energy resource a, $(P_{G.D})_b$ is the power generated by dispatchable energy resource b; $(P_{L.M})_c$ is the power curtailed from load management program participant c; P_{imp} is the power that shuold be imported by the μG to maintain its adequacy; $C_{G.Ra}$ is the generation cost (in \$/MWh) of the renewable energy resource a; $C_{G.Db}$ is the generation cost (in \$/MWh) of the dispatchable energy resource b; $C_{L.Mc}$ is the cost of curtailing power (in \$/MWh) for participant c enrolling in the load management program; C_{imp} is the cost of imported power (i.e. large value is assigned so that the μG maintains its adequacy without importing power); $N_{G.R}$ is the set of renewable energy resources; $N_{G.D}$ is the set of dispatchable energy resources; $N_{L.M}$ is the set of participants in load management program; N_{Loads} is the set of loads; P_{loss} is the power losses.

The power that can be exported by the μG from renewable energy resources and dispatchable DGs is given in (6.6) and (6.7), respectively.

$$(P_{exp.R}) = \begin{cases} (P_{G.R})^{max} - P_{G.R}, & \text{if } (P_{G.D})^{min} + (P_{G.R})^{max} \geq P_L \\ 0, & \text{otherwise} \end{cases} \tag{6.6}$$

$$(P_{exp.D}) = \begin{cases} (P_{G.D})^{max} - (P_{G.D}), \\ \qquad \text{if } (P_{G.D})^{max} + (P_{G.R})_{max} \geq P_L \text{ and } (P_{G.R})_{max} = (P_{G.R}) \\ 0, \qquad \text{otherwise} \end{cases} \tag{6.7}$$

$$(P_{exp.total}) = (P_{exp.R}) + (P_{exp.D}) \tag{6.8}$$

Where, P_{imp} is the power that should be imported by the μG to fulfill load demands; $P_{exp.R}$ and $P_{exp.D}$ are the renewable and dispatchable power can be exported by the μG.

Based on $(P_{exp.R})$, $(P_{exp.D})$, and (P_{imp}) the μG will determine its offer/bidding curve that will be submitted to the interconnected system operator.

II. Upper Level

The upper level real-time trading commences at the beginning of each sub-hourly time interval, where μG operator submits its offer/bidding curve to the interconnected system operator. The interconnected system operator will determine the trading price and shares it, in addition to the requested power/power awarded by/to each μG operator in order to maximize the social welfare as described in (6.9). The social welfare is maximized subject to: 1) demand-supply equilibrium: ensures that market is cleared such that the total accepted demand is equal to the total accepted generation (6.11), 2) limits on bids/ offers accepted in auction, and 3) PD^{max} / PG^{max}: demand/generation bid/offer blocks offered by participants (6.12) and (6.13).

$$J = \sum_{j=1}^{N_D} \sum_{k=1}^{N_{D_j}} (\rho_{D_{jk}}) (PD_{j.k}) (W_j) - \sum_{i=1}^{N_G} \sum_{b=1}^{N_{G_i}} (\rho_{G_{ib}}) (PG_{i.b}) (\overline{W_j}) \tag{6.9}$$

Where,

$$W_j = 1 - \overline{W_j} = \begin{cases} 1, & \text{B}id \\ 0, & \text{O}ffer \end{cases} \tag{6.10}$$

Subjected to,

$$\sum_{j=1}^{N_D} \sum_{k=1}^{N_{D_j}} PD_{j.k} = \sum_{i=1}^{N_G} \sum_{b=1}^{N_{G_i}} PG_{i.b} \tag{6.11}$$

$$0 \leq (PD_{j.k}) \leq (PD_{j.k})^{max} \tag{6.12}$$

$$0 \leq (PG_{i.b}) \leq (PG_{i.b})^{max} \tag{6.13}$$

Where, J is the social welfare to be maximized; $PD_{j.k}$ is the power block k bid by demand j; $PG_{i.b}$ is the power block b offered by generator i; ND_j, NG_i are the number of blocks bid/offered by demand j / generator i; ND, NG are the number of demand / generator participants; price of block k bid by demand j; $\rho_{D_{jk}}$ is the price of block k bid by demand j; $\rho_{G_{ib}}$ is the price of block b offered by generator i; PD^{Max} / PG^{Max} are the max size of demand or supply bid/offer block offered.

It is worth noting that the trading price is the dual variable (Lagrange multiplier) associated with this equality constraint:

It coincides either with price of the most expensive generation block that has been accepted or price of cheapest demand block that has been accepted

- Demand is cleared up to the point that marginal benefit they derive is equal to the price they pay
- Generation is cleared up to the point that their marginal cost is equal to the price they receive

6.3.2 Stage 2

In the second stage, the μGs are given the chance to adjust their biddings/offers based on the trading price achieved in Stage 1 and the amount of purchased energy. This arrangement is beneficial as it allows the μGs to minimize their operational costs and ensure full utilization of renewable-based DGs. For instance, a μG that placed an offer at high price in stage 1, higher than the trading price and hence did not sell any power, might place a bid at stage 2 to purchase the excessive renewable energy that was not purchased in stage 1. In that case, the buyer μG hence minimizes its operational cost, while the seller μG makes extra profit through the utilization of its renewable-based DGs.

It is worth while to note that the amount of power that should be imported/ can be exported by each μG, in Stage 2, are adjusted to account for the energy purchased/sold in Stage 1, as given in (6.14)-(6.16).

$$(P_{exp.R})_{stage2} = (P_{exp.R})_o - (P_{exp.R})_{stage1} \tag{6.14}$$

$$(P_{exp.D})_{stage2} = (P_{exp.D})_o - (P_{exp.D})_{stage1} \tag{6.15}$$

$$(P_{imp})_{stage2} = (P_{imp}) - (P_{imp})_{stage1} \tag{6.16}$$

where, $(P_{exp.R})_{stage2}$ is available power of the renewable energy resources that can be exported in Stage 2; $(P_{exp.D})_{stage2}$ is available power of the dispatchable energy resources that can be exported in Stage 2; $(P_{imp})_{stage2}$ is the amount of power that should be imported in Stage 2; $(P_{exp.R})$ is available power of the renewable energy resources that can be exported in Stage 1; $(P_{exp.D})$ is available power of the dispatchable energy resources that can be exported in Stage 1; (P_{imp}) is the amount of power that should be imported in Stage 1; $(P_{exp.R})_{stage1}$ is the power that was exported by the renewable energy resources in Stage 1; $(P_{exp.D})_{stage1}$ is the power that was exported by the dispatchable energy resources in Stage 1; $(P_{imp})_{stage1}$ is the power that was imported by the renewable energy resources in Stage 1.

6.4 Case Study

In this section, the case study used to evaluate and validate the effectiveness of the proposed DATM is presented. The case study is used to evaluate the conventional energy trading (i.e. Stage 1 only) and the proposed DATM performance over a 24-hour profile, and compare the results in terms of operation cost, importing cost, exporting revenue, and net trading value; a positive net trading value means revenue, while a negative net trading value means cost. The two mechanism were implemented in GAMS. The following subsections provide the description of the system under study and the simulation results.

6.4.1 System Description

Eight microgrids are considered in this case study, where each microgrid can have various types (AC/DC) of loads and DGs. The active power limits of the system energy resources, in addition to the peak load demands are given in Table 6.1. The operational costs of the PV panels, wind DGs, and dispatchable DGs are given as 8.0 \$/MWh, 10.0 \$/MWh, and 30.40 \$/MWh, respectively [108], [109].

Table 6.1: Data for the System Loads and Energy Resources (MW)

	Load Demands		**Energy Resources**			
Microgrid	Loads	EVs	Dispatchable		PV	Wind
No.	P_L	P_{EV}	P_G^{max}	P_G^{min}	P_G	P_G
1	1.00	0.10	0.50	0.10	–	0.85
2	1.00	0.10	0.90	0.36	1.00	–
3	1.00	0.15	0.70	0.14	0.50	0.50
4	1.00	0.10	0.50	0.10	–	0.70
5	0.50	–	0.50	0.10	0.50	–
6	1.00	0.10	0.60	0.12	1.00	–
7	0.00	–	–	–	–	0.80
8	1.00	–	–	–	–	–

6.4.2 Input Profiles

Fig. 6.2 shows the forecasted load demand of various μGs. The IEEE-RTS system [110] and the load data provided in [87] were used to calculate the load profile. The forecased load demands given in Fig. 6.2-(a) - Fig. 6.2-(d) are applied to μG.1 - μG.4, respectively. It is worth noting that μG.7 and μG.8 have the same load demands as of μG.1, while μG.5 and μG.6 have the same load demands as of μG.4 and μG.3, respectively.

The PV and wind DGs output power, given in Fig. 6.3, were obtained from [87, 111], respectively. The demand of the EVSs, , given in Fig. 6.3, were modeled based on 15-pole charging station profile given in [89] .

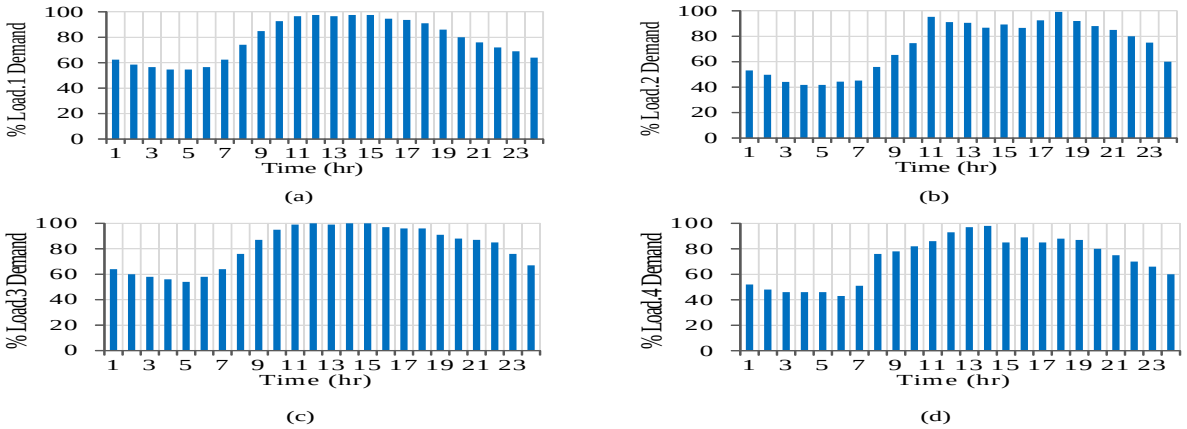

Figure 6.2: Load Demands.

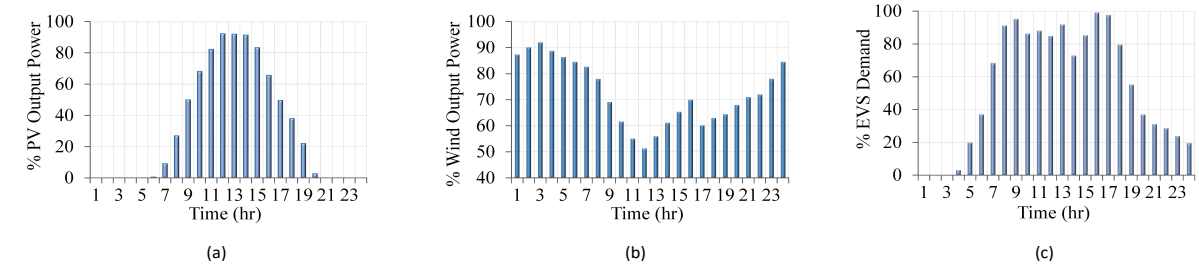

Figure 6.3: Input profiles: (a) forecasted PV power; (b) forecasted wind power; (c) forecasted EVs load demand.

6.4.3 Analysis

The output of the energy resources and the load demands define the μGs status (i.e. surplus or deficit), and hence the decision to bid/offer. It should be noted that the μGs must fulfill the minimum generation limit of the dispatchable DGs, as was given in Table 6.1. As such, the μG status can be defined as follows:

1. The μG will have surplus of power from renewable and dispatchable energy resources that can be exported if the following condition $P_{G.R} + P_{G.D}^{min}$ - $P_L > 0$ is true (i.e. minimum disptachable power in addition to renewable power is greater than the load demand).

2. The μG will have surplus of power from dispatchable energy resources that can be exported if the following condition $P_{G.R} + P_{G.D}^{min}$ - $P_L > 0$ is false (i.e. minimum disptachable power in addition to renewable power is less than the load demand, which means all renewable power is utilized and further disptachble power is needed), while the following condition $P_{G.R} + P_{G.D}$ - $P_L > 0$ is true (i.e. available disptachable power in addition to renewable power is greater than the load demand).

3. The μG will have a deficit status and requires importing power if the following condition $P_{G.R} + P_{G.D}$ - $P_L > 0$ is true.

The μGs' status are summarized in Table 6.2. It is worth noting that condition 2 is true if condition 1 is true, while condition 1 is false if condition 2 is false.

Table 6.2: Microgrids' Status

Status	$P_{G.R} + P_{G.D}^{min}$ - $P_L > 0$ (Condition 1)	$P_{G.R} + P_{G.D}$ - $P_L > 0$ (Condition 2)
Surplus: renewables and dispatchables	True	True
Surplus: dispatchables	False	True
Deficit	False	False

The 24 hour profile mimics the two aforementioned conditions are shown in Fig. 6.4. As per Fig. 6.4, the condition is true if the curve lies above the x-axis, while the condition is false if the curve lies below the x-axis. It is worth noting that the two curves are coinciding for μG_7 and μG_8 since μG_7 does not have any dispatchable energy resources or loads, while μG_8 does not have any energy resources.

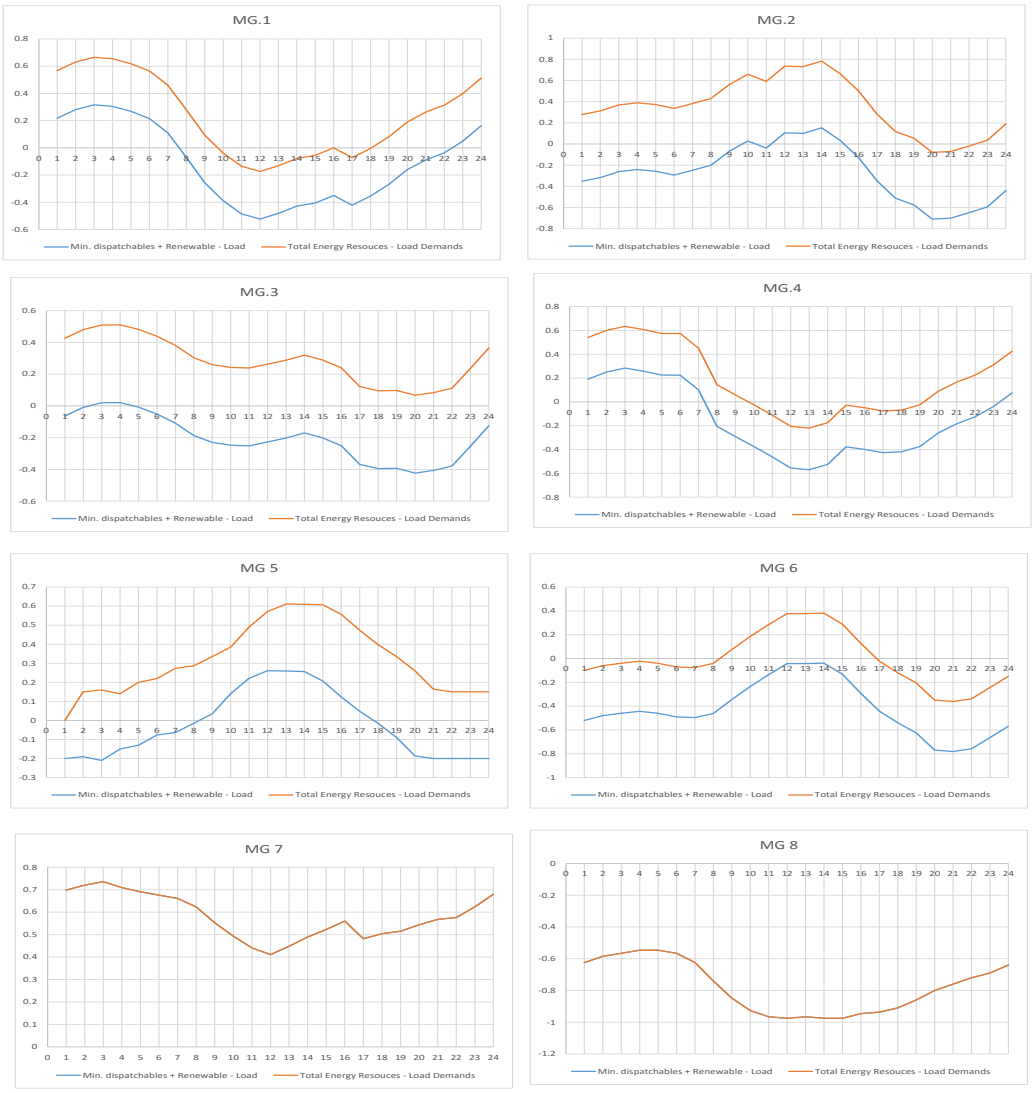

Figure 6.4: Microgrids' Status.

6.4.4 Results

This subsection presents the results of the conventional energy trading and the DATM. Based on the analysis illustrated in the previous subsection (i.e., Fig. 6.4 and Table 6.2), the status of each microgrid is determined, and hence the bidding/offer curves are developed, as summarized in Table 6.3). These curves are analyzed by the interconnected system operator to determine the energy trading price and the amount of power exchange between

Table 6.3: Microgrids' Offers (O), Bids (B), Do nothing (DN) for (Stage 1, Stage 2)

Hour	μG_1	μG_2	μG_3	μG_4	μG_5	μG_6	μG_7	μG_8
1	(O,O)	(O,B)	(O,B)	(O,O)	(O,B)	(B,DN)	(O,O)	(B,DN)
2	(O,O)	(O,B)	(O,B)	(O,O)	(O,B)	(B,DN)	(O,O)	(B,DN)
3	(O,O)	(O,B)	(O,O)	(O,O)	(O,B)	(B,DN)	(O,O)	(B,DN)
4	(O,O)	(O,B)	(O,O)	(O,O)	(O,B)	(B,DN)	(O,O)	(B,DN)
5	(O,O)	(O,B)	(O,B)	(O,O)	(O,B)	(B,DN)	(O,O)	(B,DN)
6	(O,O)	(O,B)	(O,B)	(O,O)	(O,B)	(B,DN)	(O,O)	(B,DN)
7	(O,O)	(O,B)	(O,B)	(O,O)	(O,B)	(B,DN)	(O,O)	(B,DN)
8	(O,O)	(O,B)	(O,B)	(O,B)	(O,B)	(B,DN)	(O,O)	(B,DN)
9	(O,O)	(O,O)	(O,O)	(O,B)	(O,O)	(O,DN)	(O,O)	(B,DN)
10	(B,DN)	(O,O)	(O,B)	(B,DN)	(O,DN)	(O,O)	(O,O)	(B,DN)
11	(B,DN)	(O,O)	(O,DN)	(B,DN)	(O,DN)	(O,O)	(O,O)	(B,DN)
12	(B,DN)	(O,O)	(O,O)	(B,DN)	(O,O)	(O,O)	(O,O)	(B,DN)
13	(B,DN)	(O,O)	(O,O)	(B,DN)	(O,DN)	(O,O)	(O,O)	(B,DN)
14	(B,DN)	(O,O)	(O,B)	(B,DN)	(O,O)	(O,B)	(O,O)	(B,DN)
15	(B,DN)	(O,O)	(O,O)	(B,DN)	(O,O)	(O,O)	(O,O)	(B,DN)
16	(B,DN)	(O,O)	(O,O)	(B,DN)	(O,O)	(O,O)	(O,O)	(B,DN)
17	(B,DN)	(O,DN)	(O,O)	(B,DN)	(O,O)	(B,DN)	(O,O)	(B,DN)
18	(B,DN)	(O,DN)	(O,DN)	(B,DN)	(O,DN)	(B,DN)	(O,O)	(B,DN)
19	(O,O)	(O,O)	(O,O)	(B,DN)	(O,O)	(B,DN)	(O,O)	(B,DN)
20	(O,O)	(B,DN)	(O,DN)	(O,DN)	(O,DN)	(B,DN)	(O,O)	(B,DN)
21	(O,O)	(B,DN)	(O,O)	(O,O)	(O,O)	(B,DN)	(O,O)	(B,DN)
22	(O,DN)	(B,DN)	(O,O)	(O,O)	(O,B)	(B,DN)	(O,O)	(B,DN)
23	(O,O)	(O,O)	(O,O)	(O,O)	(O,O)	(B,DN)	(O,O)	(B,DN)
24	(O,O)	(O,B)	(O,B)	(O,O)	(O,B)	(B,DN)	(O,O)	(B,DN)

the μGs. Afterwards, the μGs are given the chance to participate in Stage 2 by submitting new offers/bids, however, they also have the option to not participate (i.e. Do nothing). Stage 2 results in a decrease in the μGs operation cost and reduces the renewable power curtailment by 1) providing the μG that have excess renewable energy, which were not purchased in Stage 1 to submit new reduced offers to avoid the curtailment of the renewable energy resources unitized power and 2) providing the μGs with expensive energy resources to reduce their operation cost by purchasing cheap power in Stage 2.

The results are summarized in Table 6.4. It is worth noting that the μGs profit from selling energy to its loads is not shown in the results since it has the same value for both mechanisms. The results revealed that the implementation of DATM results in:

1. μG_1, μG_4, μG_5, and μG_7 achieved cost savings of 5.12 %, 2.43 %, 1.60 %, and 1.84 % despite the increase in the operation cost, since the increase in the operation cost is compensated by the extra profit from selling excess power.
2. μG_2 and μG_3 achieved cost savings of 4.67 % and 3.16 % due to the purchasing of cheap power in Stage 2, and hence reducing their operation cost.
3. μG_6 and μG_8 are not improved as they submit high bids in Stage 1 to secure their power requirements and avoid compensating their loads.

Table 6.4: Annual Cost and Revenue for Each μG ($)

	Operation Cost		**Import Cost**		**Export Revenue**		**Net Trading Value**	
μG	CT	DATM	CT	DATM	CT	DATM	CT	DATM
1	134,141	137,901	36,590	36,590	63,108	72,108	-107,623	-102,383
2	166,663	148,446	7,606	21,611	80,008	80,008	-94,262	-90,049
3	154,281	141,947	0.0	9,519	62,384	62,384	- 91,896	-89,082
4	125,710	127,681	29,194	29,194	38,482	43,210	-116,423	-113,666
5	86,383	80,499	0.0	4,528	170,046	170,046	83,663	85,018
6	161,050	161,050	86,484	86,484	44,872	44,872	-202,662	-202,662
7	45,322	51,344	0.0	0.0	487,450	501,744	442,128	450,429
8	0.0	0.0	786,477	786,477	0.0	0.0	-786,477	-786,477

Fig. 6.5 - Fig. 6.9 show the annual operation cost, annual import cost, annual export revenue, and net trading value, and curtailed renewable energy of IμGs, respectively. The

results revealed that the implementation of DATM resulted in cost savings of 2.9 % for the IμGs, and reduction in the amount of curtailed renewable energy from 1,424.87 MWh to 314.56 MWh, which validates the effectiveness of the proposed mechanism and its capability in reducing the operation cost and amount of curtailed renewable energy.

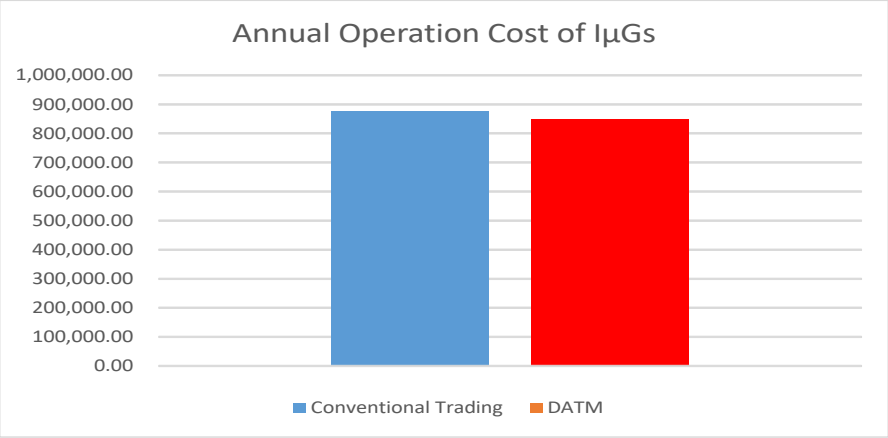

Figure 6.5: Annual Operation Cost of IμGs ($).

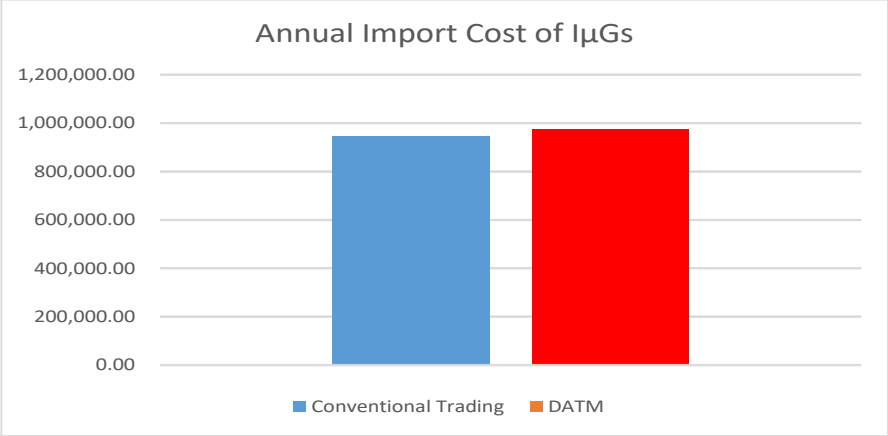

Figure 6.6: Annual Import Cost of IμGs ($).

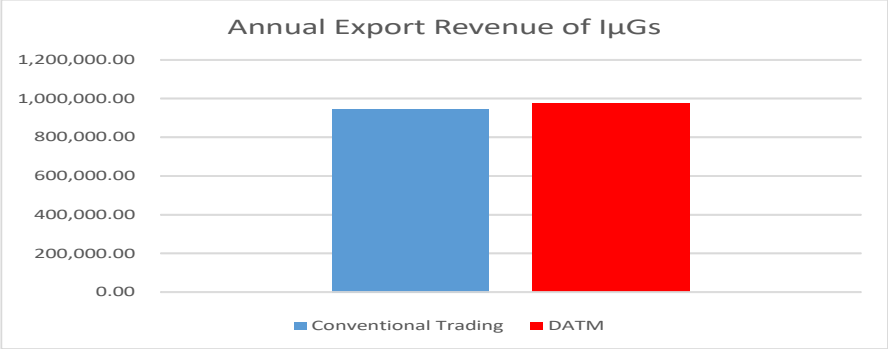

Figure 6.7: Annual Export Revenue of IμGs ($).

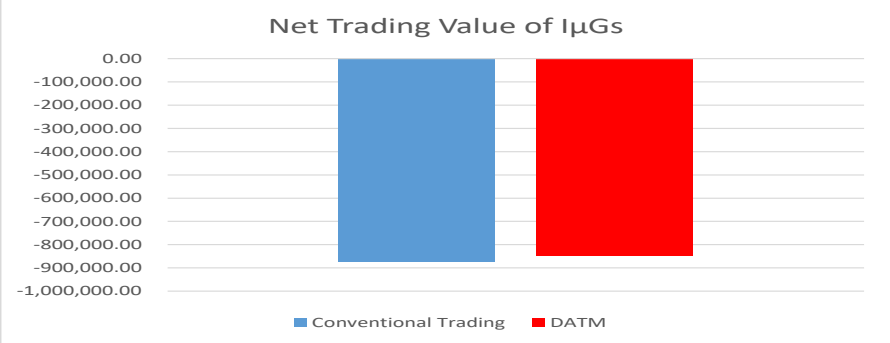

Figure 6.8: Annual Trading Value of IμGs ($).

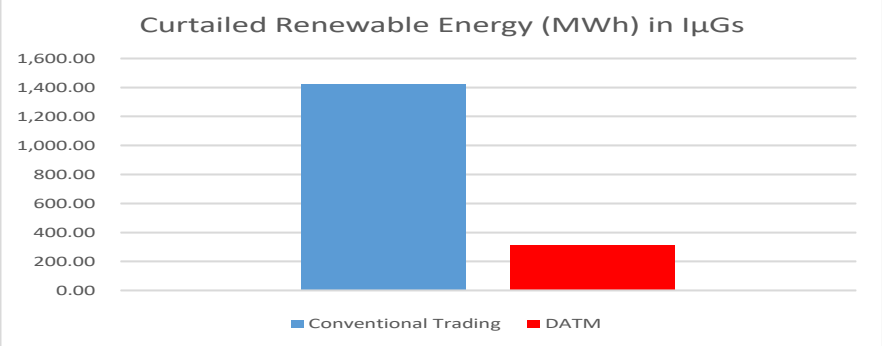

Figure 6.9: Annual Curtailed Energy from Renewable Energy Resources (MWh) of IμGs.

6.5 Conclusions

A novel dual action energy trading mechanism for interconnected microgrids has been proposed in this Chapter. The DATM facilitates the energy trading through the integration of two trading stages. Stage 1 is the conventional trading at which the μGs submit their bids/offers to the interconnected system operator to determine the trading price and the amount of power exchange. Afterwards, the μGs are given the chance to participate in Stage 2 by submitting new offers/bids, however, they also have the option to not participate (i.e. Do nothing). Stage 2 results in a decrease in the μGs operation cost and reduces the renewable power curtailment by 1) providing the μG that have excess renewable energy, which were not purchased in Stage 1 to submit new reduced offers to avoid the curtailment of the renewable energy resources unitized power and 2) providing the μGs with expensive energy resources to reduce their operation cost by purchasing cheap power in Stage 2. A case study with eight μGs has been implemented to validate the effectiveness of the proposed trading mechanism by conducting detailed comparison with the conventional trading in terms of operation cost, import cost, export cost, and amount of curtailed power from renewable energy resources. The obtained results demonstrated the benefits and the cost savings offered by the DATM and showed the capability of the DATM in achieving the optimal operation for the case under study.

Chapter 7

Summary, Contributions, and Directions for Future Work

7.1 Summary and Conclusions

The main objective of the research presented in this thesis was to facilitate the utilization of μGs by addressing and providing solutions to the challenges associated with their implementation. . In order to achieve this objective, this thesis addressed the challenges associated with the promotion and realization of μGs, and presented novel solutions to tackle these challenges. The research presented in this thesis included four consecutive parts: 1) developing a stochastic planning framework for the network configuration of AC-DC Bilayer microgrid, 2) achieving optimal and reliable operation of AC-DC bilayer microgrid under AC/DC layer fault, 3) developing a stochastic planning framework for interconnected microgrids, and 4) developing an energy trading mechanism for interconnected microgrids. A detailed summary of the four parts performed in this work is presented below.

The first part of this research introduces the AC-DC bilayer μG configuration and a novel stochastic planning framework. Detailed analysis of this configuration was presented in Chapter 3. This BμG configuration consists of 1) an AC layer, in which AC loads and DGs are connected to AC buses, 2) a DC layer, in which DC loads and DGs are connected to DC buses, and 3) interlinking converters (ICs) that facilitate the con-

nection between the AC and DC layers. This novel configuration reduces the number of interfacing converters and accommodates the increased penetration of DC DGs and DC loads. However, achieving the proper and optimal operation of this bilayer configuration requires an efficient planning framework, which was also introduced in Chapter 3. The objective of the planning framework is to determine the optimal bilayer configuration that minimizes the system total costs. In order to achieve the aforementioned objective, the planning framework solves the planning problem by providing the following decisions: 1) the optimal connection of the AC layer, 2) the optimal connection of the DC layer, and 3) the optimal number, sizes, and locations of the ICs. The proposed framework takes into account the stochastic variations in load demands and renewable-based DGs through the use of an Monte-Carlo simulation technique, in order to achieve reliable and realistic planning solution. Two case studies were implemented to validate the effectiveness of the proposed planning framework.

In the second part, a mathematical formulation for the fault current calculation in the interlinked BμGs was presented. The detailed analysis and formulas was presented in Chapter 4. The fault current calculations considered the layout of the converter and the switching schemes for two fault scenarios, AC-side and DC-side faults. The two fault scenarios were studied to present a formula for the calculation of the fault current contribution from both the faulty and the healthy layers during each fault scenario. The bilayer configuration was modeled and simulated using MATLAB/SIMULINK during these fault scenarios. The results obtained from the simulation study were compared with the presented mathematical model to validate the effectiveness of the derived formulations. The agreement between the simulation results and mathematical model output proves the correctness of the proposed formulas to calculate the fault current and the contribution of each layer in both fault scenarios.

Furthermore, a solution for the fault current elevation in BμGs was also presented in Chapter 4. This solution depends on confining the fault within its original zone thus preventing the current contribution from the healthy layer to the faulty layer, through the utilization of a novel modular multilevel converter topology, switched capacitor submodule (SCSM), instead of the conventional VSC. This quarantine is achieved by turning off the gating signals from IGBTs upon fault occurrence. As a result, the SM will generate an opposing voltage causing the diodes to be reversed biased, and hence blocking any

continuous current paths. A case study was implemented to prove the effectiveness of the proposed methodology in confining the fault within its zone and preventing any inter-layers contribution. The results show the successful converter operation regards blocking any current contribution from the the faulty layer to the healthy layer, and hence quarantining the fault in the faulty layer. Additionally, reactivating the gating signals to the IGBTs helped to restore system's normal conditions when the fault is cleared. This fault confining improves system operation and thus prevents unnecessary disconnection of the two layers.

In the third part, a novel stochastic interconnection planning framework for μGs was proposed. The planning framework determines the optimal IμGs configuration that minimizes the investment and operation costs through the integration of two stages. The first stage determines the candidate buses of each μG, where the candidate bus is the bus that maximizes/minimizes the μG capability to export/import power to/from the neighboring μGs. The second stage aims to determine the optimal IμGs configuration that minimizes the net present value of the system costs through the determination of: 1) the interconnection lines that will form the IμGs network, 2) the types of these lines (AC/DC), and 3) the locations and sizes of the interlinking converters used to interconnect two μGs with different types of power. The proposed interconnection planning framework was successfully tested on a case study of a system of five different types of μGs. The case-study system was solved assuming a single DG failure for two cases: obtained IμGs configuration and islanded μGs. The obtained results verified the capability of the framework in achieving the optimal configuration for the system under study. The results revealed that the μGs interconnection significantly reduced the load curtailment and enhanced the system operation.

In the fourth part, a DATM was proposed. This mechanism arranges and facilitates the power trading between the interconnected microgrids. This mechanism aims to minimize the operation cost of the μGs and provide full utilization of renewable energy resources, and hence maximize the social welfare. In order to achieve these objectives, the mechanism includes two trading stages. Stage 1 is the conventional trading at which the μGs submit their bids/offers to the interconnected system operator to determine the trading price and the amount of power exchange. Afterwards, the μGs are given the chance to participate in Stage 2 by submitting new offers/bids, however, they also have the option to not participate (i.e. Do nothing). Afterwards, the μGs are given the chance to participate in Stage 2 by

submitting new offers/bids, however, they also have the option to not participate (i.e. Do nothing). As a result, the RERs power that were not traded in Stage 1 can be utilized and exchanged in Stage 2, which increases profit of the seller (i.e. instead of curtailing this power) and minimizes the operation cost of the buyer (i.e. purchasing clean power for low price instead of utilizing its own dispatchables). The proposed DATM has been evaluated on a case study with eight μGs to validate its effectiveness. The evaluation included detailed comparison for the DATM with the conventional trading mechanism in terms of operation cost, import cost, export cost, and amount of curtailed power from renewable energy resources. The obtained results demonstrated the benefits and the cost savings offered by the DATM and showed the capability of the DATM in achieving the optimal operation for the case under study.

7.2 Contributions

The major contributions of the work presented in this thesis can be highlighted as follows:

1. Promoting and enhancing the AC-DC bilayer μG configuration that facilitates the integration of different types (AC and DC) of loads and DGs by connecting all the AC/DC loads and DGs directly to the corresponding AC/DC layer due to the existence of both layers (AC/DC).

2. Developing a novel stochastic planning framework for the network configuration of bilayer microgrids. The framework searches for the optimal BμG configuration that minimizes the total system costs. The model incorporates consideration of the stochastic behavior of load demands and renewable DGs.

3. Proposing MMC as interlinking converter for AC/DC microgrids and utilizing its fault confining capability to eliminate the fault current contribution between the AC and DC layer of the bilayer μG. This unique feature of the MMC would quarantine the fault inside each layer and thus prevents the faulty layer from contributing to the fault current through blocking any continuous current paths.

4. Developing a stochastic planning framework for interconnected microgrids. The planning framework minimizes the total system costs and minimizes the loads curtailment

under DG failure, through the determination of interconnection buses and optimal interconnection configuration. The developed model is generic, versatile, and can be readily used for all types of μGs.

5. Introducing a two stage trading mechanism that facilitates the power exchange between the interconnected microgrids. In the first stage, the μGs submit their bids and offers to fulfill their power requirements or export their excess power. In the second stage, the μGs are given the chance to participate in another trading round and submit new bids/offers, which results in full utilization of energy resources and minimum operation cost.

7.3 Directions for Future Work

Based on the work presented in this thesis, the following topics are suggested for future exploration:

1. Investigating and assessing the techno-economic impacts of battery storage systems on the planning and operation of bilayer μGs. In this case, the planning and operation models should be developed to enable consideration of the charging and discharging cycles of battery storage systems.

2. The application of the reliability-based planning model for the design of isolated interconnected microgrids.

3. Conducting a small signal stability analysis for the interconnected microgrids to ensure the seamless transitions between different operating modes.

4. The development of DATM to include network connections of each microgrid in the interconnected system to account for the power losses in each microgrid and operation constraint.

5. Investigating the security and transparency of the transactions to ensure that the reliability and efficiency of the DATM.

References

[1] Ontario Power Authority. (Feb. 2016). Fit Program. [Online]. Available: http://fit.powerauthority.on.ca/fit-program.

[2] Nova Scotia Power Inc. COMFIT program. [Online]. Available: https://energy.novascotia.ca/renewables/programs-and-projects/comfit.

[3] Tax Incentives for Clean Energy Equipment, Government of Canada. [Online]. Available: https://www.canada.ca/en/revenue-agency/services/tax/technical-information/income-tax/income-tax-folios-index/series-3-property-investments-savings-plans/series-3-property-investments-savings-plan-folio-8-resource-properties/income-tax-folio-s3-f8-c2-tax-incentives-clean-energy-equipment.html.

[4] Natural Resources Canada. Gams. [Online]. Available: https://www.nrcan.gc.ca/energy/energy-sources-distribution/renewables/about-renewable-energy/7295

[5] Renewable energy facts, natural resources canada. [Online]. Available: https://www.nrcan.gc.ca/science-data/data-analysis/energy-data-analysis/renewable-energy-facts/20069

[6] T. Wu, C. Chang, L. Lin, G. Yu, and Y. Chang, "Dc-bus voltage control with a three-phase bidirectional inverter for dc distribution systems," *IEEE Transactions on Power Electronics*, vol. 28, no. 4, pp. 1890–1899, 2013.

[7] X. She, A. Q. Huang, S. Lukic, and M. E. Baran, "On integration of solid-state transformer with zonal dc microgrid," *IEEE Transactions on Smart Grid*, vol. 3, no. 2, pp. 975–985, 2012.

[8] K. Kurohane, T. Senjyu, A. Yona, N. Urasaki, T. Goya, and T. Funabashi, "A hybrid smart ac/dc power system," *IEEE Transactions on Smart Grid*, vol. 1, no. 2, pp. 199–204, 2010.

[9] S. K. Chaudhary, J. M. Guerrero, and R. Teodorescu, "Enhancing the capacity of the ac distribution system using dc interlinks—a step toward future dc grid," *IEEE Transactions on Smart Grid*, vol. 6, no. 4, pp. 1722–1729, 2015.

[10] A. A. Hamad, M. E. Nassar, E. F. El Saadany, and M. M. A. Salama, "Optimal configuration of isolated hybrid ac/dc microgrids," *IEEE Transactions on Smart Grid*, pp. 1–1, 2018.

[11] F. Nejabatkhah, Y. W. Li, A. B. Nassif, and T. Kang, "Optimal design and operation of a remote hybrid microgrid," *CPSS Transactions on Power Electronics and Applications*, vol. 3, no. 1, pp. 3–13, 2018.

[12] G. F. Reed, B. M. Grainger, A. R. Sparacino, and Z. Mao, "Ship to grid: Medium-voltage dc concepts in theory and practice," *IEEE Power and Energy Magazine*, vol. 10, no. 6, pp. 70–79, 2012.

[13] L. A. de Souza Ribeiro, O. R. Saavedra, S. L. de Lima, and J. de Matos, "Isolated micro-grids with renewable hybrid generation: The case of lençóis island," *IEEE Transactions on Sustainable Energy*, vol. 2, no. 1, pp. 1–11, 2011.

[14] International Renewable Energy Agency (IRENA) (2017, Oct.). Battery storage for renewables: market status and technology outlook. [Online]. Available: https://www.irena.org/-/media/Files/IRENA/Agency/Publication/2017/Oct/IRENA_Electricity_Storage_Costs_2017.pdf.

[15] International Energy Agency. Global EV Outlook, 2020. [Online]. Available: https://www.iea.org/reports/global-ev-outlook-2020.

[16] A. A. Hamad, H. E. Farag, and E. F. El-Saadany, "A novel multiagent control scheme for voltage regulation in dc distribution systems," *IEEE Transactions on Sustainable Energy*, vol. 6, no. 2, pp. 534–545, 2015.

[17] A. A. Hamad, M. A. Azzouz, and E. F. El-Saadany, "Multiagent supervisory control for power management in dc microgrids," *IEEE Transactions on Smart Grid*, vol. 7, no. 2, pp. 1057–1068, 2016.

[18] L. A. de Souza Ribeiro, O. R. Saavedra, S. L. de Lima, and J. de Matos, "Isolated micro-grids with renewable hybrid generation: The case of lençóis island," *IEEE Transactions on Sustainable Energy*, vol. 2, no. 1, pp. 1–11, 2011.

[19] A. Mohamed, V. Salehi, and O. Mohammed, "Real-time energy management algorithm for mitigation of pulse loads in hybrid microgrids," *IEEE Transactions on Smart Grid*, vol. 3, no. 4, pp. 1911–1922, 2012.

[20] V. K. Sood, *"HVDC and FACTS Conrollers: Applications of Static Converters in Power Systems"*. Kluwer Academic Publishers Academic Press, 2004.

[21] C. Du, *"The control of VSC-HVDC and its use for large industrial power systems", Ph.D. thesis, Department of Electric Power Engineering, Chalmers University of Technology, Goteborg, Sweden, 2003.*

[22] T. W. May, Y. M. Yeap, and A. Ukil, "Comparative evaluation of power loss in hvac and hvdc transmission systems," in *2016 IEEE Region 10 Conference (TENCON)*, 2016, pp. 637–641.

[23] A. Lesnicar and R. Marquardt, "An innovative modular multilevel converter topology suitable for a wide power range," in *2003 IEEE Bologna Power Tech Conference Proceedings,*, vol. 3, 2003.

[24] B. R. B. J. J. S. R. Hauth, P. Tatro and J. Fink, *"HVDC Power Transmission Technology Assess", Oak Ridge Nat.Lab. Rep, May 2007.*

[25] A. Lotfjou, Y. Fu, and M. Shahidehpour, "Hybrid ac/dc transmission expansion planning," *IEEE Transactions on Power Delivery*, vol. 27, no. 3, pp. 1620–1628, 2012.

[26] W. Feng, L. A. Tuan, L. B. Tjernberg, A. Mannikoff, and A. Bergman, "A new approach for benefit evaluation of multiterminal vsc–hvdc using a proposed mixed

ac/dc optimal power flow," *IEEE Transactions on Power Delivery*, vol. 29, no. 1, pp. 432–443, 2014.

[27] P. C. Loh, D. Li, Y. K. Chai, and F. Blaabjerg, "Autonomous operation of hybrid microgrid with ac and dc subgrids," *IEEE Transactions on Power Electronics*, vol. 28, no. 5, pp. 2214–2223, May 2013.

[28] X. Liu, P. Wang, and P. C. Loh, "A hybrid ac/dc microgrid and its coordination control," *IEEE Transactions on Smart Grid*, vol. 2, no. 2, pp. 278–286, June 2011.

[29] J. M. Guerrero, P. C. Loh, T. Lee, and M. Chandorkar, "Advanced control architectures for intelligent microgridspart ii: Power quality, energy storage, and ac/dc microgrids," *IEEE Transactions on Industrial Electronics*, vol. 60, no. 4, pp. 1263–1270, April 2013.

[30] X. Liu, P. Wang, and P. C. Loh, "A hybrid ac/dc microgrid and its coordination control," *IEEE Transactions on Smart Grid*, vol. 2, no. 2, pp. 278–286, June 2011.

[31] J. M. Guerrero, P. C. Loh, T. Lee, and M. Chandorkar, "Advanced control architectures for intelligent microgridspart ii: Power quality, energy storage, and ac/dc microgrids," *IEEE Transactions on Industrial Electronics*, vol. 60, no. 4, pp. 1263–1270, April 2013.

[32] J. L. T. Kaipia, P. Salonen and J. Partanen, "Possibilities of the low voltage dc distribution systems," *Nordac, Nordic Distribution and Asset Management Conference*, pp. 1–10, 2006.

[33] P. N. P. P. P. Salonen, T. Kaipia and J. Partanen, "An lvdc distribution system concept," *NORPIE, Nordic Workshop on Power and Industrial Electroncis*, 2008.

[34] P. Borazjani, N. I. A. Wahab, H. B. Hizam, and A. B. C. Soh, "A review on microgrid control techniques," in *2014 IEEE Innovative Smart Grid Technologies - Asia (ISGT ASIA)*, 2014, pp. 749–753.

[35] A. A. Hamad, M. A. Azzouz, and E. F. El Saadany, "A sequential power flow algorithm for islanded hybrid ac/dc microgrids," *IEEE Transactions on Power Systems*, vol. 31, no. 5, pp. 3961–3970, 2016.

[36] K. Tanaka, "Decentralized voltage control in distribution systems by distributed generators," in *2009 IEEE International Symposium on Industrial Electronics*, 2009, pp. 554–559.

[37] X. Lu, J. M. Guerrero, K. Sun, J. C. Vasquez, R. Teodorescu, and L. Huang, "Hierarchical control of parallel ac-dc converter interfaces for hybrid microgrids," *IEEE Transactions on Smart Grid*, vol. 5, no. 2, pp. 683–692, 2014.

[38] P. C. Loh, D. Li, Y. K. Chai, and F. Blaabjerg, "Autonomous operation of hybrid microgrid with ac and dc subgrids," *IEEE Transactions on Power Electronics*, vol. 28, no. 5, pp. 2214–2223, 2013.

[39] A. Khodaei, "Provisional microgrids," *IEEE Transactions on Smart Grid*, vol. 6, no. 3, pp. 1107–1115, May 2015.

[40] C. Battistelli, Y. P. Agalgaonkar, and B. C. Pal, "Probabilistic dispatch of remote hybrid microgrids including battery storage and load management," *IEEE Transactions on Smart Grid*, vol. 8, no. 3, pp. 1305–1317, May 2017.

[41] A. Khodaei, "Microgrid optimal scheduling with multi-period islanding constraints," *IEEE Transactions on Power Systems*, vol. 29, no. 3, pp. 1383–1392, May 2014.

[42] H. Lotfi and A. Khodaei, "Static hybrid ac/dc microgrid planning," in *2016 IEEE Power Energy Society Innovative Smart Grid Technologies Conference (ISGT)*, Sep. 2016, pp. 1–5.

[43] H. Lotfi and A. Khodaei, "AC versus DC microgrid planning," *IEEE Transactions on Smart Grid*, vol. 8, no. 1, pp. 296–304, Jan 2017.

[44] S. Mohamed, M. F. Shaaban, M. Ismail, E. Serpedin, and K. A. Qaraqe, "An efficient planning algorithm for hybrid remote microgrids," *IEEE Transactions on Sustainable Energy*, vol. 10, no. 1, pp. 257–267, Jan 2019.

[45] H. M. A. Ahmed, A. B. Eltantawy, and M. M. A. Salama, "A planning approach for the network configuration of ac-dc hybrid distribution systems," *IEEE Transactions on Smart Grid*, vol. 9, no. 3, pp. 2203–2213, May 2018.

[46] M. A. Zamani, T. S. Sidhu, and A. Yazdani, "A protection strategy and microprocessor-based relay for low-voltage microgrids," *IEEE Transactions on Power Delivery*, vol. 26, no. 3, pp. 1873–1883, 2011.

[47] J. Shiles, E. Wong, S. Rao, C. Sanden, M. A. Zamani, M. Davari, and F. Katiraei, "Microgrid protection: An overview of protection strategies in north american microgrid projects," in *2017 IEEE Power Energy Society General Meeting*, 2017, pp. 1–5.

[48] M. Baran and I. EI-Markaby, "Fault analysis on distribution feeders with distributed generators," in *2006 IEEE Power Engineering Society General Meeting*, 2006, pp. 1 pp.–.

[49] M. Brucoli, T. C. Green, and J. D. F. McDonald, "Modelling and analysis of fault behaviour of inverter microgrids to aid future fault detection," in *2007 IEEE International Conference on System of Systems Engineering*, 2007, pp. 1–6.

[50] C. A. Plet, M. Graovac, T. C. Green, and R. Iravani, "Fault response of grid-connected inverter dominated networks," in *IEEE PES General Meeting*, 2010, pp. 1–8.

[51] M. Kamh and R. Iravani, "A unified three-phase power-flow analysis model for electronically-coupled distributed energy resources," in *2011 IEEE Power and Energy Society General Meeting*, 2011, pp. 1–1.

[52] M. Z. Kamh and R. Iravani, "A unified three-phase power-flow analysis model for electronically coupled distributed energy resources," *IEEE Transactions on Power Delivery*, vol. 26, no. 2, pp. 899–909, 2011.

[53] J. Yang, J. E. Fletcher, and J. O'Reilly, "Short-circuit and ground fault analyses and location in vsc-based dc network cables," *IEEE Transactions on Industrial Electronics*, vol. 59, no. 10, pp. 3827–3837, 2012.

[54] C. M. Franck, "Hvdc circuit breakers: A review identifying future research needs," *IEEE Transactions on Power Delivery*, vol. 26, no. 2, pp. 998–1007, 2011.

[55] J. Candelaria and J. Park, "Vsc-hvdc system protection: A review of current methods," in *2011 IEEE/PES Power Systems Conference and Exposition*, 2011, pp. 1–7.

[56] R. Minciardi and R. Sacile, "Optimal control in a cooperative network of smart power grids," *IEEE Systems Journal*, vol. 6, no. 1, pp. 126–133, March 2012.

[57] L. Che, X. Zhang, M. Shahidehpour, A. Alabdulwahab, and A. Abusorrah, "Optimal interconnection planning of community microgrids with renewable energy sources," *IEEE Transactions on Smart Grid*, vol. 8, no. 3, pp. 1054–1063, May 2017.

[58] Z. Wang and J. Wang, "Self-healing resilient distribution systems based on sectionalization into microgrids," *IEEE Transactions on Power Systems*, vol. 30, no. 6, pp. 3139–3149, Nov 2015.

[59] Z. Wang, B. Chen, J. Wang, M. M. Begovic, and C. Chen, "Coordinated energy management of networked microgrids in distribution systems," *IEEE Transactions on Smart Grid*, vol. 6, no. 1, pp. 45–53, Jan 2015.

[60] H. Dagdougui, A. Ouammi, and R. Sacile, "Optimal control of a network of power microgrids using the pontryagin's minimum principle," *IEEE Transactions on Control Systems Technology*, vol. 22, no. 5, pp. 1942–1948, Sep 2014.

[61] F. Shahnia, R. P. S. Chandrasena, S. Rajakaruna, and A. Ghosh, "Primary control level of parallel distributed energy resources converters in system of multiple interconnected autonomous microgrids within self-healing networks," *IET Generation, Transmission Distribution*, vol. 8, no. 2, pp. 203–222, February 2014.

[62] E. Pashajavid, F. Shahnia, and A. Ghosh, "Overload management of autonomous microgrids," in *2015 IEEE 11th International Conference on Power Electronics and Drive Systems*, June 2015, pp. 73–78.

[63] ——, "Interconnection of two neighboring autonomous microgrids based on small signal analysis," in *2015 9th International Conference on Power Electronics and ECCE Asia (ICPE-ECCE Asia)*, June 2015, pp. 213–220.

[64] F. Shahnia, S. Bourbour, and A. Ghosh, "Coupling neighboring microgrids for overload management based on dynamic multicriteria decision-making," *IEEE Transactions on Smart Grid*, vol. 8, no. 2, pp. 969–983, March 2017.

[65] M. Hemmati, S. Ghasemzadeh, and B. Mohammadi-Ivatloo, "Optimal scheduling of smart reconfigurable neighbour micro-grids," *IET Generation, Transmission Distribution*, vol. 13, no. 3, pp. 380–389, 2019.

[66] M. Fathi and H. Bevrani, "Statistical cooperative power dispatching in interconnected microgrids," *IEEE Transactions on Sustainable Energy*, vol. 4, no. 3, pp. 586–593, July 2013.

[67] J. Matamoros, D. Gregoratti, and M. Dohler, "Microgrids energy trading in islanding mode," in *2012 IEEE Third International Conference on Smart Grid Communications (SmartGridComm)*, Nov 2012, pp. 49–54.

[68] D. Gregoratti and J. Matamoros, "Distributed energy trading: the multiple-microgrid case," *IEEE Transactions on Industrial Electronics*, vol. 62, no. 4, pp. 2551–2559, April 2015.

[69] H. Wang and J. Huang, "Cooperative planning of renewable generations for interconnected microgrids," *IEEE Transactions on Smart Grid*, vol. 7, no. 5, pp. 2486–2496, Sep 2016.

[70] F. Samadi Gazijahani and J. Salehi, "Stochastic multi-objective framework for optimal dynamic planning of interconnected microgrids," *IET Renewable Power Generation*, vol. 11, no. 14, pp. 1749–1759, 2017.

[71] H. S. V. S. Kumar Nunna and S. Doolla, "Multiagent-based distributed-energy-resource management for intelligent microgrids," *IEEE Transactions on Industrial Electronics*, vol. 60, no. 4, pp. 1678–1687, 2013.

[72] Reforming the Energy Vision. [Online]. Available: https://rev.ny.gov/

[73] H. Wang and J. Huang, "Incentivizing energy trading for interconnected microgrids," *IEEE Transactions on Smart Grid*, vol. 9, no. 4, pp. 2647–2657, 2018.

[74] Y. Wang, W. Saad, Z. Han, H. V. Poor, and T. Başar, "A game-theoretic approach to energy trading in the smart grid," *IEEE Transactions on Smart Grid*, vol. 5, no. 3, pp. 1439–1450, 2014.

[75] D. An, Q. Yang, W. Yu, X. Yang, X. Fu, and W. Zhao, "Soda: Strategy-proof online double auction scheme for multimicrogrids bidding," *IEEE Transactions on Systems, Man, and Cybernetics: Systems*, vol. 48, no. 7, pp. 1177–1190, 2018.

[76] H. S. V. S. Kumar Nunna and S. Doolla, "Multiagent-based distributed-energy-resource management for intelligent microgrids," *IEEE Transactions on Industrial Electronics*, vol. 60, no. 4, pp. 1678–1687, 2013.

[77] W. Lee, L. Xiang, R. Schober, and V. W. S. Wong, "Direct electricity trading in smart grid: A coalitional game analysis," *IEEE Journal on Selected Areas in Communications*, vol. 32, no. 7, pp. 1398–1411, 2014.

[78] L. Xiang, W. Lee, R. Schober, and V. W. S. Wong, "Direct electricity trading in smart grid: A coalitional game analysis," *IEEE Journal on Selected Areas in Communications*, vol. 32, no. 7, pp. 1398–1411, 2014.

[79] W. Tushar, T. K. Saha, C. Yuen, P. Liddell, R. Bean, and H. V. Poor, "Peer-to-peer energy trading with sustainable user participation: A game theoretic approach," *IEEE Access*, vol. 6, pp. 62 932–62 943, 2018.

[80] M. Fathi and H. Bevrani, "Statistical cooperative power dispatching in interconnected microgrids," *IEEE Transactions on Sustainable Energy*, vol. 4, no. 3, pp. 586–593, 2013.

[81] J. Matamoros, D. Gregoratti, and M. Dohler, "Microgrids energy trading in islanding mode," in *2012 IEEE Third International Conference on Smart Grid Communications (SmartGridComm)*, 2012, pp. 49–54.

[82] D. Gregoratti and J. Matamoros, "Distributed energy trading: The multiple-microgrid case," *IEEE Transactions on Industrial Electronics*, vol. 62, no. 4, pp. 2551–2559, 2015.

[83] A. S. Kelso and V. P. Crawford, "Job matching, coalition formation, and gross substitutes," *Econometrica*, vol. 50, no. 6, pp. 1483–1504, 1982.

[84] J. W. Hatfield, S. D. Kominers, A. Tamura, and A. Teytelboym, "Stability and competitive equilibrium in trading networks," *J. Polit. Econ.*, vol. 121, no. 5, pp. 966–1005, 2013.

[85] T. Fleiner, J. Janko, A. Tamura, and A. Teytelboym, "Trading networks with bilateral contracts," *in Proc. 3rd Conf. Auctions Market Mech. Appl.*, no. 5, pp. 1–39, 2015.

[86] GDXMRW. General algebraic modeling system. [Online]. Available: https://www.gams.com/latest/docs/T_GDXMRW.html

[87] Y. M. Atwa and E. F. El-Saadany, "Optimal allocation of ess in distribution systems with a high penetration of wind energy," *IEEE Transactions on Power Systems*, vol. 25, no. 4, pp. 1815–1822, Nov 2010.

[88] Solar Powered in Toronto. (2015, Nov.). [Online]. Available: http://www.yourturn.ca/solar/our-system/graphs-and-logs/.

[89] Y. Liao and C. Lu, "Dispatch of ev charging station energy resources for sustainable mobility," *IEEE Transactions on Transportation Electrification*, vol. 1, no. 1, pp. 86–93, June 2015.

[90] MathWave Technologies. (2015, Nov.). Data analysis and simulation. [Online]. Available: http://www.mathwave.com/.

[91] A. A. Eajal, M. F. Shaaban, K. Ponnambalam, and E. F. El-Saadany, "Stochastic centralized dispatch scheme for AC/DC hybrid smart distribution systems," *IEEE Transactions on Sustainable Energy*, vol. 7, no. 3, pp. 1046–1059, July 2016.

[92] B. W. McConnell, "Applications of high temperature superconductors to direct current electric power transmission and distribution," *IEEE Transactions on Applied Superconductivity*, vol. 15, no. 2, pp. 2142–2145, June 2005.

[93] One Stop Buy. (2015, April). Prices for power cables. [Online]. Available: http://www.onestopbuy.co/wire-cable/PENGUIN-41245.asp.

[94] ABB Sales. (2016, Nov.). Budgetary quote for medium voltage circuit breakers. [Online]. Available: http://new.abb.com/medium-voltage/apparatus/circuit-breakers.

[95] A. S. A. Awad, T. H. M. EL-Fouly, and M. M. A. Salama, "Optimal ESS allocation for benefit maximization in distribution networks," *IEEE Trans. Smart Grid*, vol. 8, no. 4, pp. 1668–1678, July 2017.

[96] National Renewable Energy Laboratory. (2016, May). On the path to sunshot: The role of advancements in solar photovoltaic efficiency, reliability, and costs. [Online]. Available: https://www.nrel.gov/docs/fy16osti/65872.pdf.

[97] A. Sallam, A. Hossam, R. Refaat, and M. Zakaria. Master of engineering science:study of modular multilevel converter for high voltage direct current systems. [Online]. Available: https://eng.alexu.edu.eg/index.php/en/news/823-elec1-master-degree-en-5-2017

[98] M. Saeedifard and R. Iravani, "Dynamic performance of a modular multilevel back-to-back hvdc system," in *2011 IEEE Power and Energy Society General Meeting*, 2011, pp. 1–1.

[99] L. Zhang, Y. Zou, J. Yu, J. Qin, V. Vittal, G. G. Karady, D. Shi, and Z. Wang, "Modeling, control, and protection of modular multilevel converter-based multi-terminal hvdc systems: A review," *CSEE Journal of Power and Energy Systems*, vol. 3, no. 4, pp. 340–352, 2017.

[100] J. Zhang, C. Jiang, and Y. Han, "Modular multilevel converter composite submodule topology and control," *The Journal of Engineering*, vol. 2019, no. 16, pp. 2643–2648, 2019.

[101] A. A. Elserougi, A. M. Massoud, and S. Ahmed, "A switched-capacitor submodule for modular multilevel hvdc converters with dc-fault blocking capability and a reduced number of sensors," *IEEE Transactions on Power Delivery*, vol. 31, no. 1, pp. 313–322, 2016.

[102] H. M. A. Ahmed, A. B. Eltantawy, and M. M. A. Salama, "A planning approach for the network configuration of ac-dc hybrid distribution systems," *IEEE Transactions on Smart Grid*, vol. 9, no. 3, pp. 2203–2213, May 2018.

[103] Y. M. Atwa and E. F. El-Saadany, "Optimal allocation of ess in distribution systems with a high penetration of wind energy," *IEEE Transactions on Power Systems*, vol. 25, no. 4, pp. 1815–1822, Nov 2010.

[104] Solar Powered in Toronto. (2015, Nov.). [Online]. Available: http://www.yourturn.ca/solar/our-system/graphs-and-logs/.

[105] Y. Liao and C. Lu, "Dispatch of ev charging station energy resources for sustainable mobility," *IEEE Transactions on Transportation Electrification*, vol. 1, no. 1, pp. 86–93, June 2015.

[106] C. Zhang, Y. Xu, Z. Y. Dong, and K. P. Wong, "Robust Coordination of Distributed Generation and Price-Based Demand Response in Microgrids," *IEEE Transactions on Smart Grid*, vol. 9, no. 5, pp. 4236–4247, Sep. 2018.

[107] G. Liu, Y. Xu, and K. Tomsovic, "Bidding Strategy for Microgrid in Day-Ahead Market Based on Hybrid Stochastic/Robust Optimization," *IEEE Transactions on Smart Grid*, Jan. 2016.

[108] C. Zhang, Y. Xu, Z. Y. Dong, and K. P. Wong, "Robust Coordination of Distributed Generation and Price-Based Demand Response in Microgrids," *IEEE Transactions on Smart Grid*, vol. 9, no. 5, pp. 4236–4247, Sep. 2018.

[109] G. Liu, Y. Xu, and K. Tomsovic, "Bidding Strategy for Microgrid in Day-Ahead Market Based on Hybrid Stochastic/Robust Optimization," *IEEE Transactions on Smart Grid*, Jan. 2016.

[110] C. Grigg, P. Wong, P. Albrecht, R. Allan, M. Bhavaraju, R. Billinton, Q. Chen, C. Fong, S. Haddad, S. Kuruganty, W. Li, R. Mukerji, D. Patton, N. Rau, D. Reppen, A. Schneider, M. Shahidehpour, and C. Singh, "The ieee reliability test system-1996. a report prepared by the reliability test system task force of the application of probability methods subcommittee," *IEEE Transactions on Power Systems*, vol. 14, no. 3, pp. 1010–1020, 1999.

[111] Solar Powered in Toronto. (2015, Nov.). Data analysis and simulation. [Online]. Available: http://www.yourturn.ca/solar/our-system/graphs-and-logs/

[112] A. Lesnicar and R. Marquardt, "An innovative modular multilevel converter topology suitable for a wide power range," in *2003 IEEE Bologna Power Tech Conference Proceedings,*, vol. 3, 2003, pp. 6 pp. Vol.3–.

APPENDICES

Appendix A

Modular Multilevel Converter Operation and Control

A.1 MMC Structure and Operation

The MMC topology general layout, shown in Fig. A.1, has two arms with number of series submodules (SMs). The different SMs configurations were extensively discussed in literature [97, 112]. Among the different configurations, the half-bridge topology is considered the simplest and most common SM topology. This half-bridge topology is structured with two IGBTs and their antiparallel diodes in addition to a capacitor as shown in Fig. A.2. The IGBTs belong to the same SM are operated in a complementary way to avoid shorting the SM. Based on the switching operation, this SM has two voltage states at its terminal (i.e. E and 0). Switching on the upper or lower IGBT will result in a terminal voltage state equals E or 0, respectively. Therefore, each SM represents a voltage step in the total MMC voltage. It is worth noting that increasing the number of SM, increases the voltage levels and hence enhances the output voltage (i.e. staircase waveform approach sinusoidal).

The level shifted pulse width modulation is used to obtain the required gating signals to generate the desired voltage. This technique starts with comparing a sinusoidal reference waveform and a triangular carrier waveform [98]. The resultant waveform from this

comparison represents the voltage levels required to realize the desired voltage as shown in Fig. A.3. Thereafter, for each voltage level, the corresponding number of SMs to be inserted in the arm current path is determined to balance the capacitors voltages (i.e. within +/- 5 % margin). The conventional voltage balancing technique depends on sorting the capacitors voltages as follows [98]:

1. For $I_{arm} > 0$, select the SMs with lowest capacitor voltages to avoid capacitors' overcharging.

2. For $I_{arm} < 0$, select the SMs with highest capacitor voltages to avoid capacitors' over discharging.

Fig. A.4 summarizes the capacitor voltage balancing algorithm.

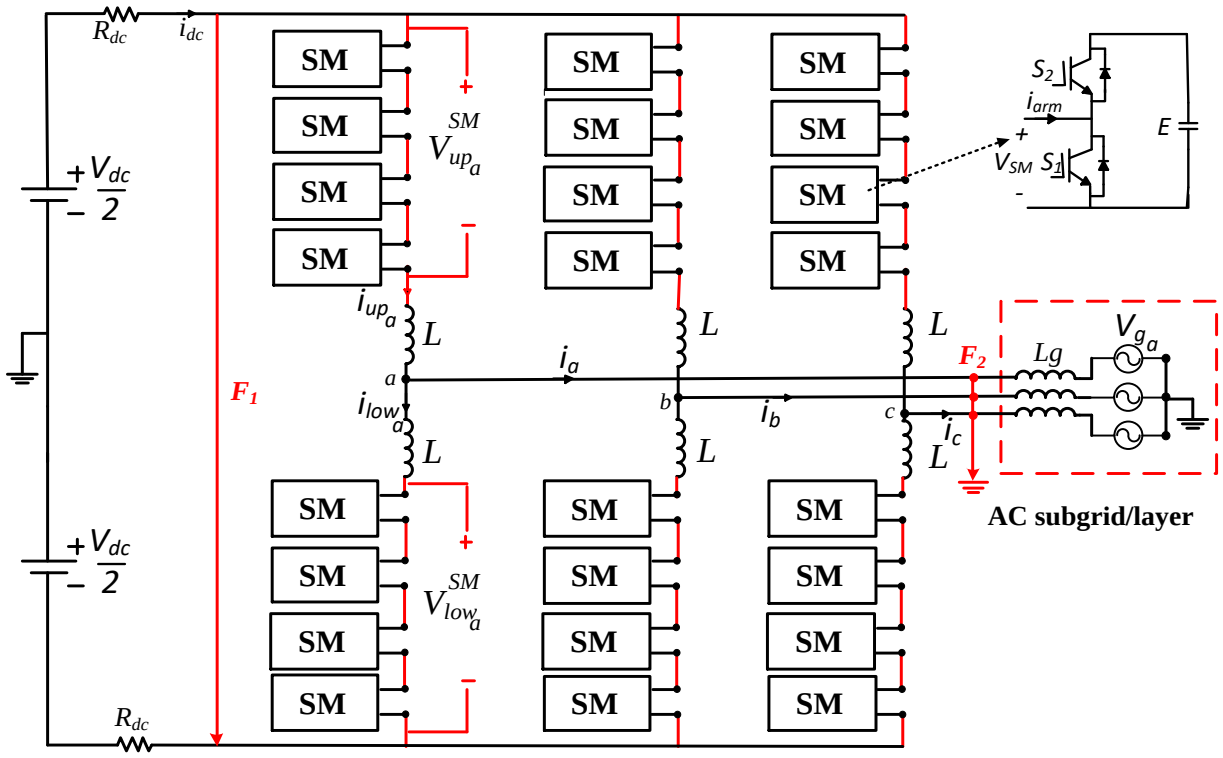

Figure A.1: Modular Multilevel Converter Layout.

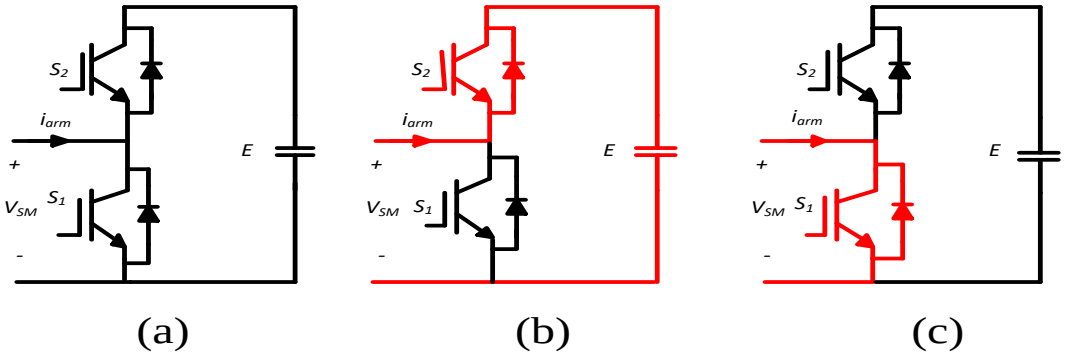

Figure A.2: (a) Half-bridge Submodule Configuration, (b) On State, (c) Off State

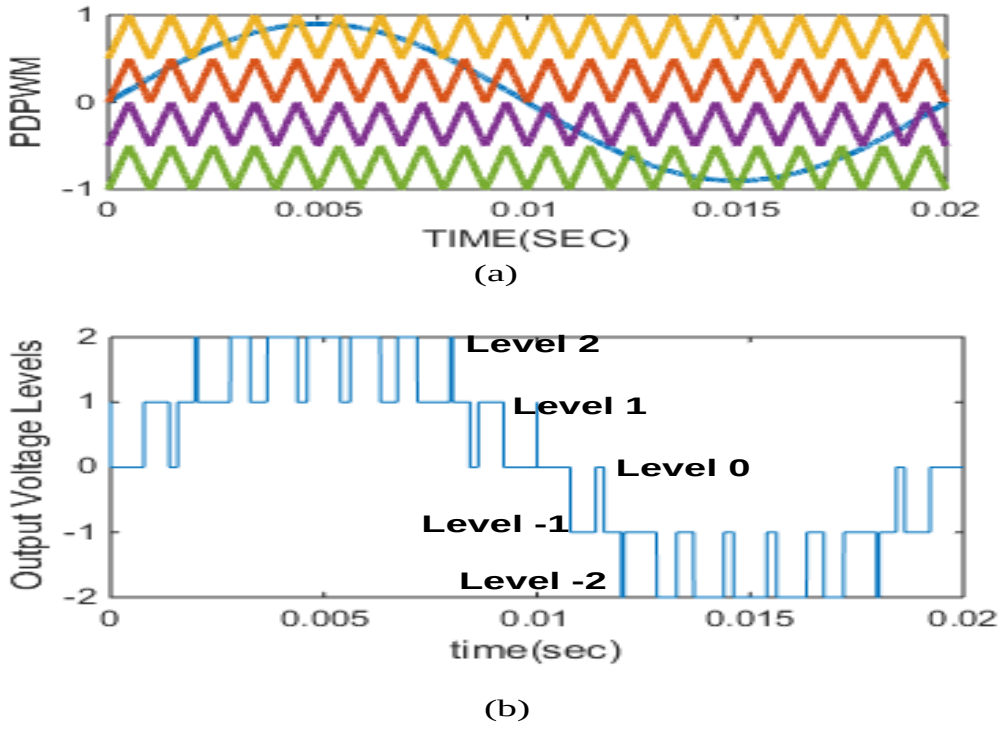

Figure A.3: Level Shifted Pulse Width Modulation

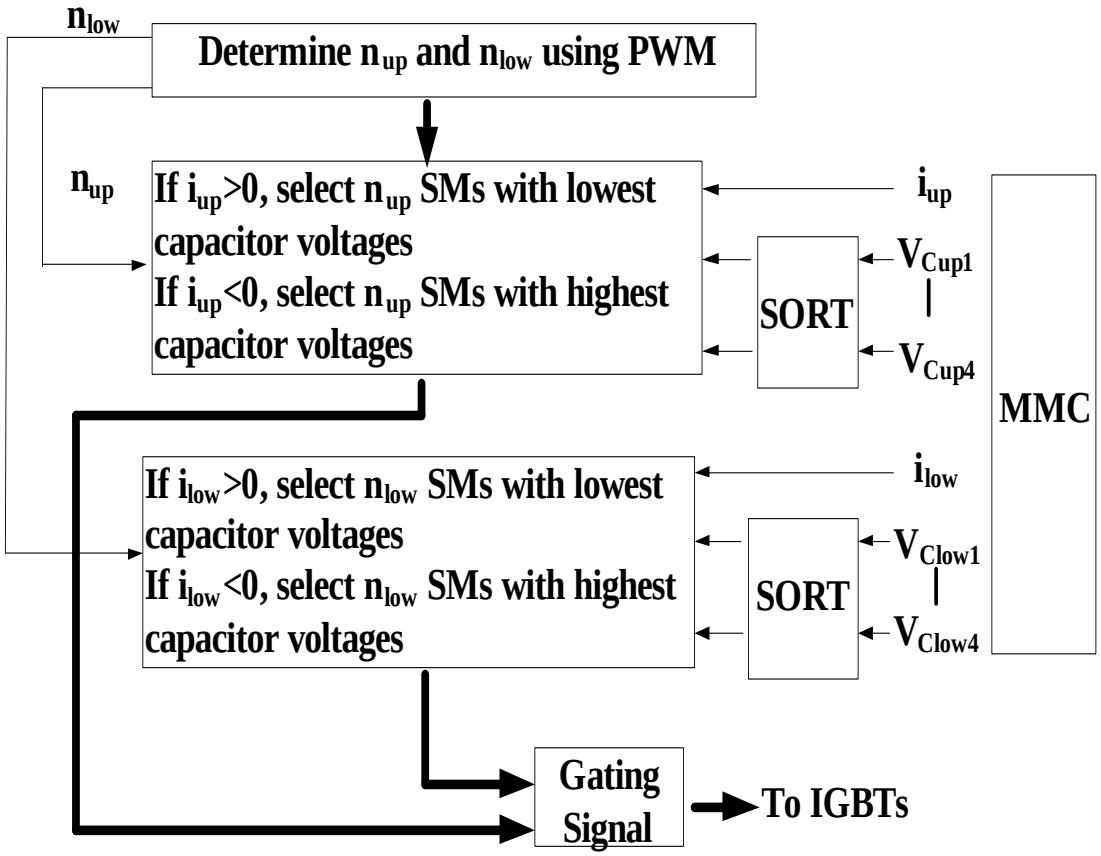

Figure A.4: Capacitor Voltage Balancing Algorithm

The main advantages of the MMC can be summarized as follows [2, 29, 36, 37, 40]:

1. Modularity
2. Sinusoidal waveform can be obtained by connecting large number of SM in series which reduces the need for large AC filters
3. Reliability as redundant sub-modules is placed in series with the existing SMs in order to be inserted in case of SM failure

4. Increased efficiency due to low switching frequency of each sub-module
5. Reduced footprint due to the elimination of the bulky DC-link capacitors

However, despite the great advantages of the modular multilevel converter, it has the following disadvantages [36,37]:

1. High number of switching devices are used which makes the control system more complex and more costly
2. Difficulties in keeping the capacitor voltages balanced especially with large numbers of capacitors at higher number of levels. As a result, extra control for the voltage balancing of the modules' capacitors is needed
3. Circulating current flows between the phase legs which increases the losses inside the converter

A.2 Fault Confining Capability of Half-Bridge Sub-module

Fault confining capability is crucial to prevent any contribution from the AC layer into the DC layer and vice versa. When a fault is detected, both layers should be isolated to avoid the contribution of the fault from one of the layers to the other. Unfortunately, the conventional half-bridge SM topology is unable to provide fault confining capability since it acts as uncontrolled rectifier when the IGBTs signals are turned off (i.e. when a fault occurs), as illustrated in Fig. A.5. The half-bridge SM topology provides a path for the current through its free wheeling diodes depending on the arm current direction. When the arm current is positive (i.e. See Fig. A.5-a), the current passes through D2 resulting a voltage E across the SM terminals, and hence the capacitors are in charging state. However, when the arm current is negative (i.e. See Fig. A.5-b), the current passes through D1 resulting in a zero voltage across the SM terminals, and hence the capacitor voltage remains constant. The absence of capacitors's discharging state results in over charging of the capacitors and dramatic increase in their voltages which would damage the semiconductor devices.

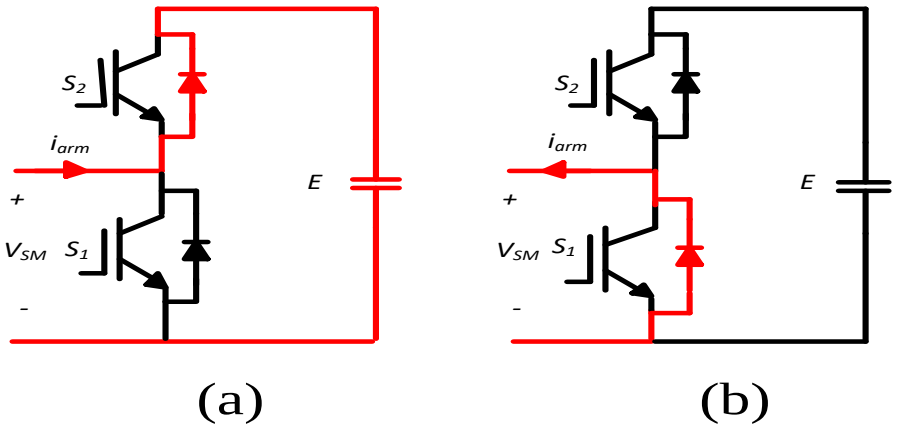

Figure A.5: Half-bridge SM Configuration Operation During Fault Conditions

A.3 Simulation Results

A simulation model for microgrid layout presented in Fig. A.1 was implemented using MATLAB/SIMULINK. In this model, a 9-level half-bridge SM MMC layout is used as the interlinking converter with a switching frequency of 3 kHz. The system operation was tested for normal operating conditions using the conventional half-bridge submodule topology. The ac layer is modeled by a voltage source connected through impedance to the MMC terminals. On the other hand, the dc layer is represented by a dc voltage source and a resistance.

A. Normal Operating Conditions

For an AC grid voltage of 4.16 KV and 1.65 MVA, the simulation results are shown in Fig. A.6. Fig. A.6.a - Fig. A.6.d show the AC grid voltages, the converter phase voltages, the ac grid currents, and the average dc grid current, respectively. The figures show that balance of the system voltages and currents within their nominal values. Moreover the current negative sign, shown in Fig. A.6.d, indicates that the power flow is from the AC grid to the DC grid.

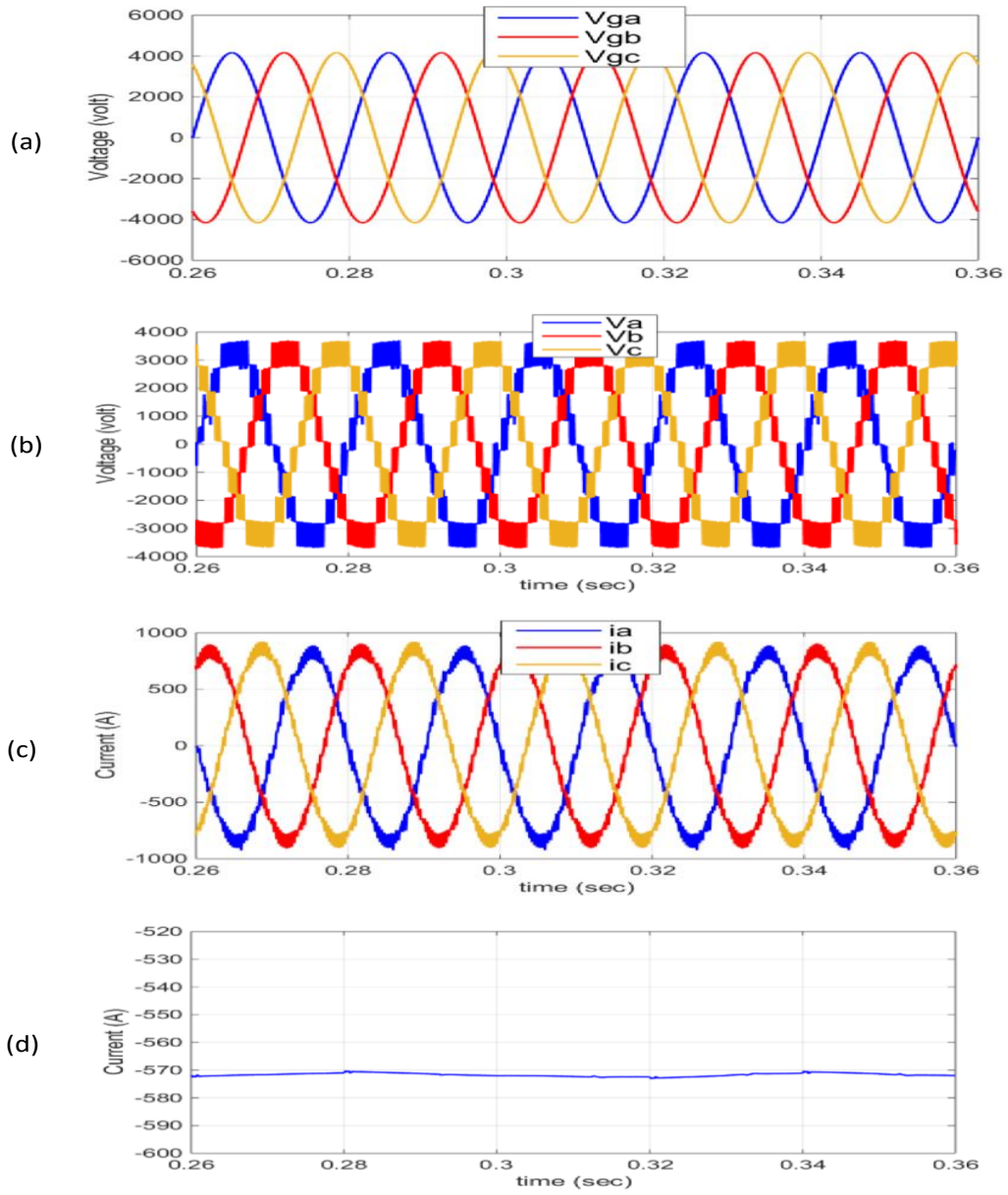

Figure A.6: Simulation Results Under Normal Operating Conditions (a): AC Grid Voltages, (b): Converter Phase Voltages, (c): AC Grid Currents, and (d): DC Grid Current